ABSTRACT

BURRIS, KEVIN DALE. Examining Winter Storm Structures with High-resolution Atmospheric Soundings. (Under the direction of Dr. Sandra Yuter).

Frozen winter precipitation has major impacts on society, including freshwater resources and transportation. Quantitative precipitation estimates for winter storms often have large errors which reduce the utility of forecasts. Current research shows that mesoscale and convective scale processes are important to the distribution of winter precipitation. Motivated by in-situ observations of ice particles by aircraft, this study focuses on two small scale processes affecting surface precipitation: ice mass loss from sublimation and ice mass growth from local instability.

Observations of 701 winter storms (November 2005 - January 2023) which include surface air temperatures less than 0°C in the Northeast United States are examined. Each storm has an associated low pressure track at least 250 km in length and with a duration $\geq$ 6 hours. The primary data set is 1,590 high resolution (1 second, 5 mb) National Weather Service upper air soundings. Complementary measurements from surface stations, radar, and sea level pressure reanalysis are combined with the radiosondes into a powerful dataset to yield insights on the vertical structures within storms. Radar reflectivity measurements concurrent with the rawinsonde's in-flight 4D position are analysed alongside the thermodynamic data. A relational database allows subsets of observations to be conditionally selected to focus on specific environments and physical processes. To simplify analysis of storms in different geographic locations, observations are placed in a low pressure centric framework. Compared to a classic skew-T, a new visualization for sounding data tailored for winter storm processes facilitates comparisons among profiles of temperature, thermodynamic stability, and wind stability.

Weather radar echoes greater than 0 dBZ, indicative of precipitation-sized ice, occurred primarily below 4 km and rarely exceeded 6 km AGL, even though cloud often extended to 8-10 km. On average, about 11% of the storm's cloud depth consisted of layers subsaturated with respect to ice ($<$ 85% RH_{ice}). Most of these dry layers sandwiched between moister layers are in the upper portion of the cloud, above where falling precipitation-size ice was present. Signatures of sublimating ice precipitation (radar echoes in layers that are subsaturated with respect to ice) within the storms are very uncommon, occurring in less than 2% of the precipitation echoes.

Most of the storm extent is neutral or stable for conditional and potential local stability. As expected, conditional and potential instability conditions are more common 1 km below cloud top than 1 km above cloud top. Moist Richardson number values indicating possible presence of Kelvin-Helmholtz waves occur about 15% of the time throughout the vertical extent of the

cloud. Commonly, there is a layer of enhanced wind shear near the cloud top boundary which implies that cloud top entrainment of dry air is nearly always occurring. In the lowest 2 km of the profiles, there is both more frequently occurring wind shear than higher altitudes and more frequently occurring local conditional and potential stable layers compared to higher altitudes. These competing factors imply the boundary layer wind shear instabilities will often be damped.

Examining Winter Storm Structures with High-resolution Atmospheric Soundings

by
Kevin Dale Burris

A dissertation submitted to the Graduate Faculty of
North Carolina State University
in partial fulfillment of the
requirements for the Degree of
Doctor of Philosophy

Marine, Earth, and Atmospheric Science

Raleigh, North Carolina
2023

APPROVED BY:

Dr. Matthew Parker	Dr. Camilo Rey-Sanchez
Dr. Jeffrey Cunningham	Dr. Jereome Lavelle

Dr. Sandra Yuter
Chair of Advisory Committee

ACKNOWLEDGEMENTS

The views expressed in this dissertation are those of the author and do not necessarily reflect the official policy or position of the Air Force, the Department of Defense or the U.S. Government.

I cannot express enough gratitude for the guidance and professional mentorship of Dr. Sandra Yuter, without which this would not be possible. Thank you to Dr. Matthew Miller for your technical advice, reviews, and comments. A special thank you to fellow students Laura Tomkins and Luke Allen for your help in sharing data, methods, and interpretations, and to Rachel Kennedy for your weekly discussions on the process.

Thank you to the United States Air Force Academy for selecting me for this program.

TABLE OF CONTENTS

LIST OF TABLES

LIST OF FIGURES

CHAPTER

1

INTRODUCTION

Winter storms and the precipitation they produce have critical impacts on society, affecting transportation, natural resources, and the economy. Each year in the United States, over 1,300 traffic fatalities occur during wintery weather, and transportation departments spend $2.3 billion attempting to control snow and ice on the road network (Federal Highway Administration 2022). Considering snow as a resource, around one sixth of the global population lives in regions where snowmelt contributes over 50% of the water available in local streamflows (Barnett et al. 2005).

Many of the key impacts of winter storms depend on how much precipitating ice mass reaches the surface. Ice precipitation can sublimate below the cloud base of winter storms where the relative humidity with respect to ice (RH_{ice}) is less than 100%. Recent aircraft observations during the NASA IMPACTS field campaign (McMurdie et al. 2022) found many precipitation particles in conditions with $RH_{ice} < 100\%$ above the lowest cloud base (Allen et al. 2021; Peele et al. 2021). Ice crystals in these layers will sublimate, reducing precipitation mass and cooling the nearby environment. If layers with $RH_{ice} < 100\%$ occupy a significant portion of the vertical profile between cloud base and cloud top, they will affect the stability profile and possibly yield enough sublimation to materially impact the surface precipitation.

Weather radar can detect precipitation-sized particles (> 0.2 mm diameter) but cannot observe cloud particles or measure relative humidity. Upper air soundings observe the detailed

vertical profile of temperature, dewpoint, pressure, wind direction, and speed. From these quantities we can derive several stability metrics (potential instability, conditional instability, and shear instability), as well as the locations of cloud using the relative humidity with respect to ice and water. We use these complementary data sets to address questions about where and how frequently sublimation (ice shrinkage) is occurring in winter cyclones. Additionally, we infer potential regions of ice growth by examining the altitudes and frequencies of different sources of instability and their occurrence within clouds.

We have developed a new way of displaying upper air sounding data in conjunction with nearby scanning radar data tailored to focus on variables of interest within winter storms. This new visualization improves comprehension of key relationships within the vertical profile of the atmosphere relevant for winter storms as compared to the traditional skew-T with its focus on CAPE, CIN, and RH with respect to water (RH_{water}) which are more relevant for warm season convection than winter snow storms.

1.1 Background and Motivation

1.1.1 Overview of cloud structures of midlatitude cyclones

The structure of midlatitude cyclones arranges the cloud and precipitation features of winter storms. Broad areas of ascending air define the extent of the cloud shield, and precipitation is typically associated with the vertical motions in regions of surface frontogenesis (though other lifting mechanisms can exists). Localized areas of increased instability yield enhanced areas of precipitation down to the ∼1 km scale of generating cells (e.g. Keeler et al. 2016a). The basic synopotic scale horizontal cloud extent, frontal positions, and air flows for a mature midlatitude cyclone are shown in Figures 1.1 and 1.2. An example satellite observation of a midlatitude cyclone is shown in Figure 1.3. The surface low and frontal positions are included. Higher cloud tops (indicated by colder brightness temperatures) are clearly favored north of the low pressure center's location associated with the "comma head".

Vertical cross-sections of clouds and precipitation associated with air flows over frontal surfaces (Figures 1.4, 1.5, 1.6, and 1.7) traditionally depict saturated conditions for the full extent of the storm between cloud base and cloud top (Hobbs 1978; Houze 1989, 2014; Matejka et al. 1980; Wallace and Hobbs 2006; Ward 2023). Sublimation of ice precipitation particles is typically only considered important between the lowest cloud base and the surface (Forbes and Hogan 2006; Roebber et al. 2003).

Recent airborne radar observations from NASA IMPACTS reveal fine details of storm structures in vertical cross-sections of winter storms (Fig. 1.8). Radar reflectivity and horizontal

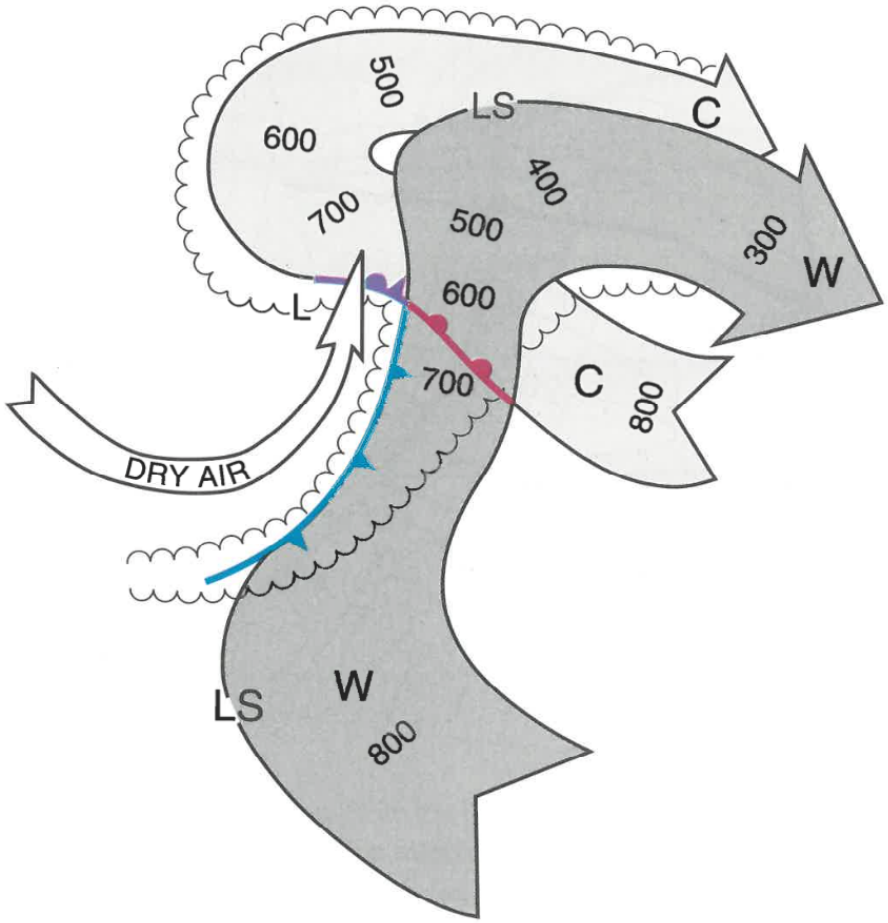

Figure 1.1: A schematic of warm (W) and cold (C) airflows in a mature midlatitude cyclone. Surface low pressure center and fronts are annotated. Numbers inside the arrows indicate the top of the ascending airflow in mb. Figure 3.1.24 from Bader et al. (1995), adapted from Carlson (1980).

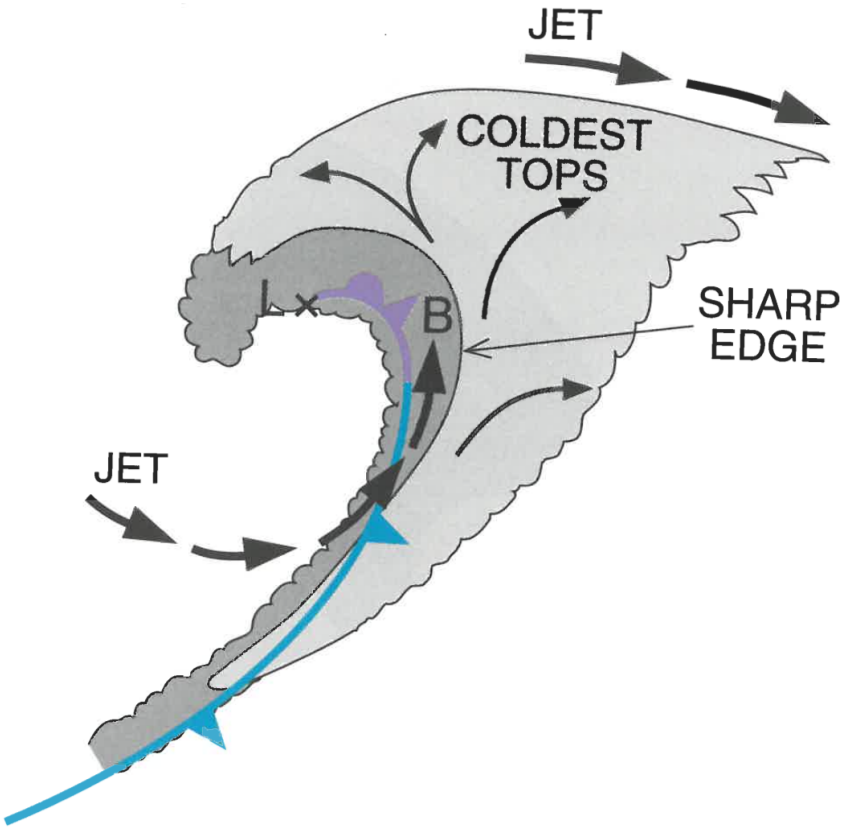

Figure 1.2: A diagram of a comma cloud in a mature midlatitude cyclone. Arrows indicate system-relative synoptic flow. Surface low pressure center and fronts are annotated. Figure 3.4.11 from Bader et al. (1995).

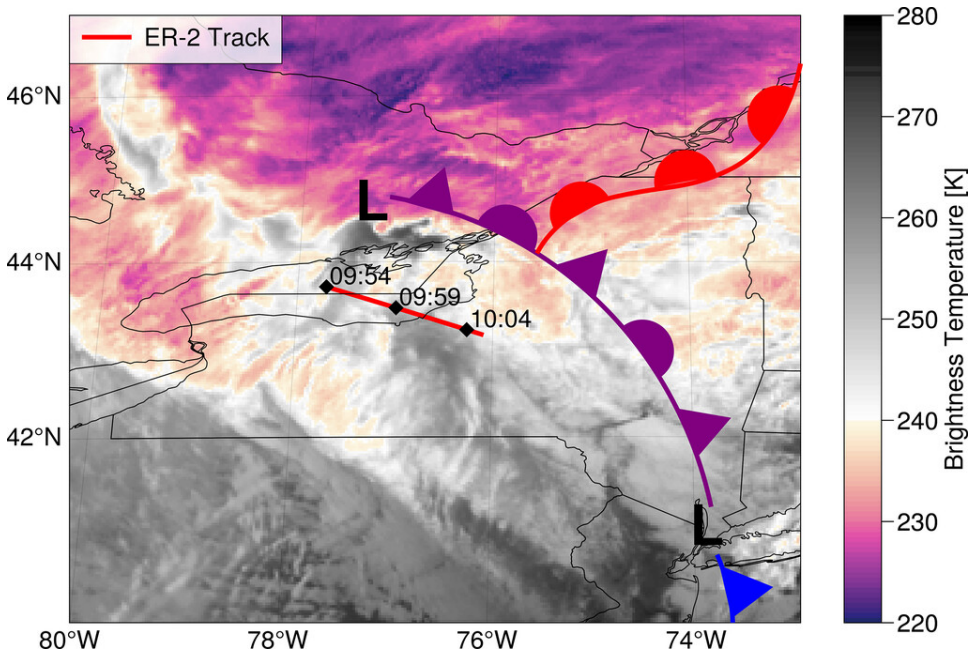

Figure 1.3: Infrared brightness temperatures of a mature, deep occluded cyclone at 1000 UTC 27 Feb 2020. Data is from the Advanced Baseline Imager channel 13 of GOES-16; frontal analysis derived from National Weather Service Weather Prediction Center surface analysis. ER-2 track is high-altitude aircraft associated with NASA IMPACTS. Figure 9 from McMurdie et al. (2022)

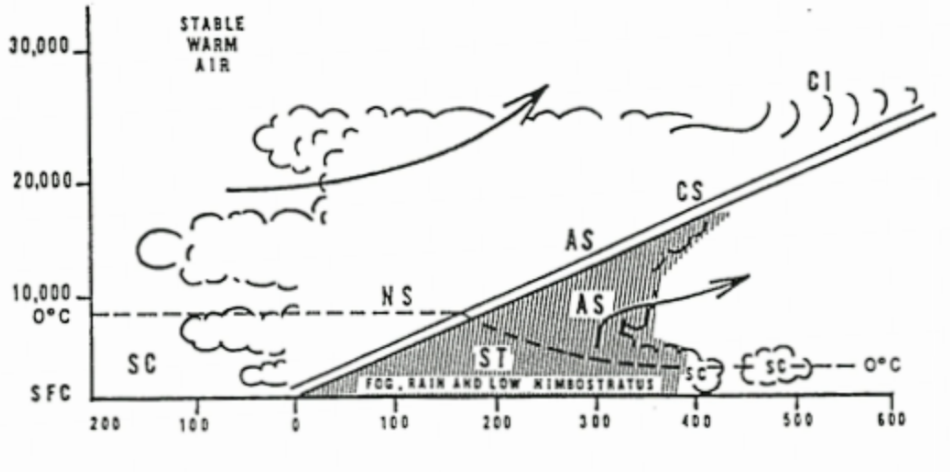

Figure 1.4: Schematic cross section of clouds, vertical motions, and precipitation associated with a stable warm front. Figure from Ward (2023).

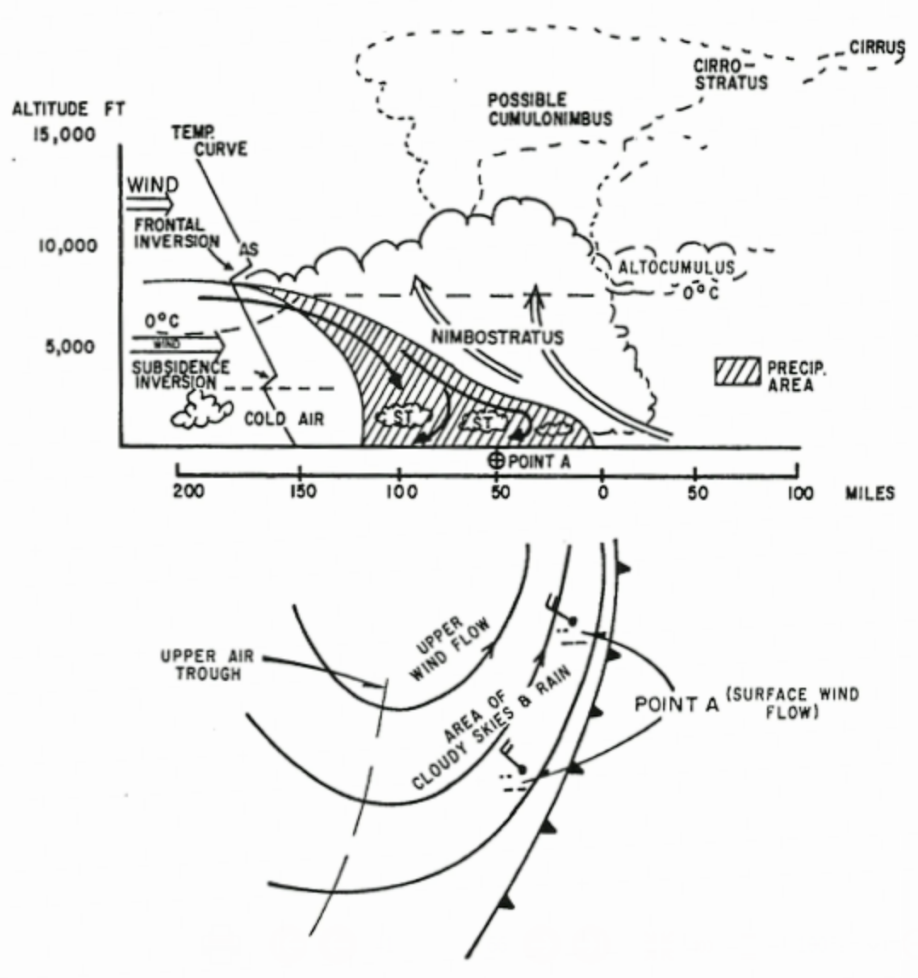

Slow Moving Active Cold Front

Figure 1.5: Schematic cross section of clouds, vertical motions, and precipitation associated with a slow moving cold front. Figure from Ward (2023).

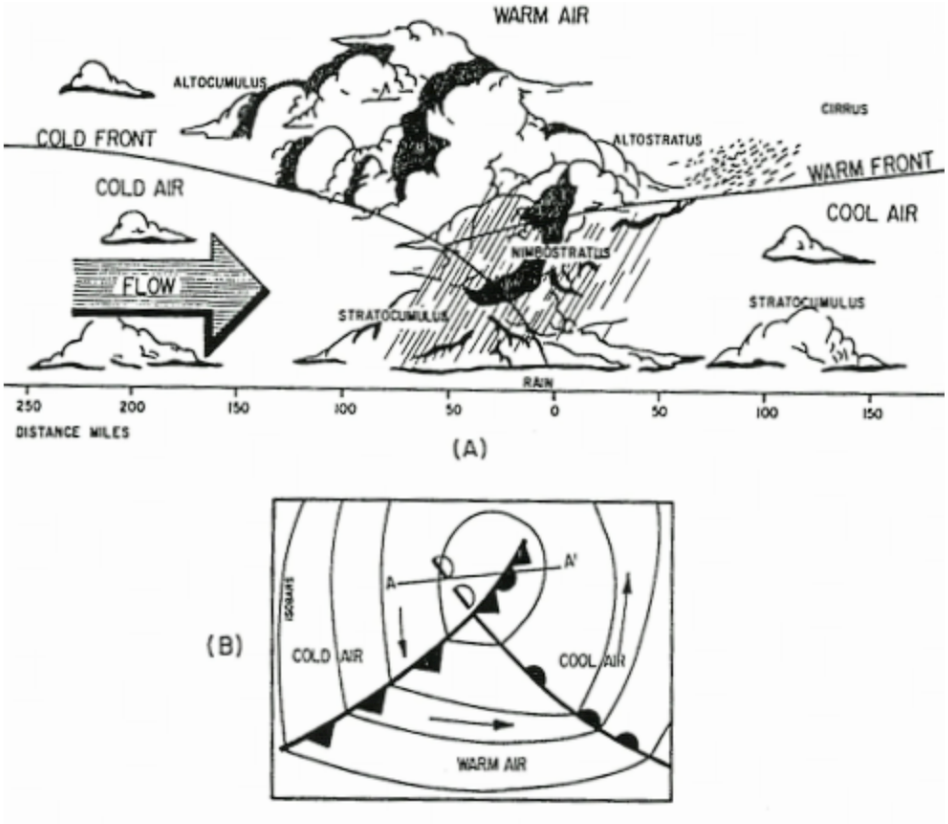

Vertical Structure Of A Cold Occlusion

Figure 1.6: Schematic cross section of clouds, vertical motions, and precipitation associated with a cold occlusion. Figure from Ward (2023)

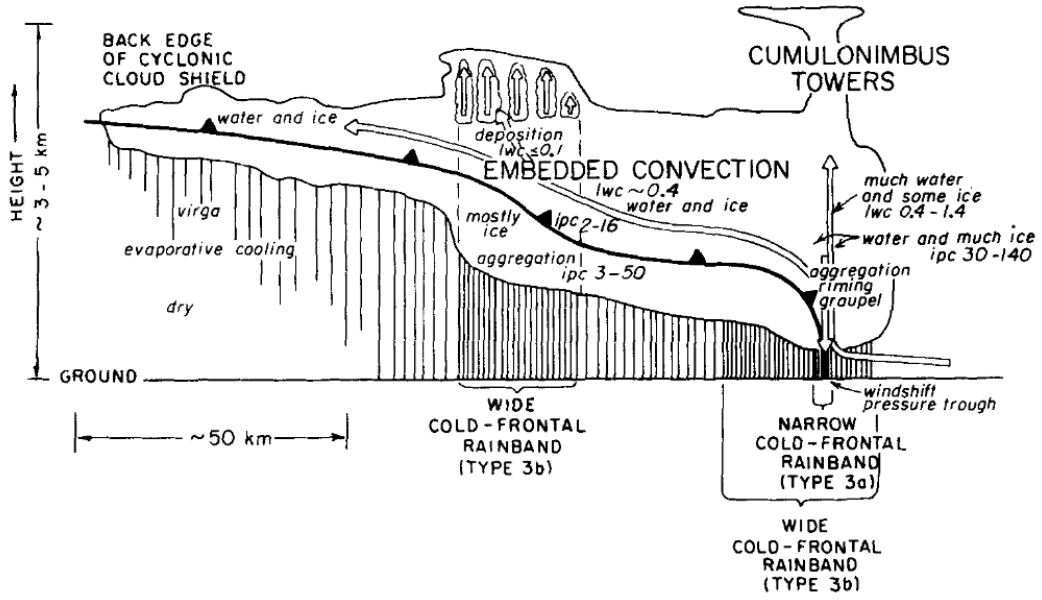

Fig. 1.7: Vertical cross section of clouds and precipitation associated with a cold front. Evaporation and sublimation is only depicted below cloud bases, especially high cloud bases with virga. Figure 8 from Matejka et al. (1980).

winds show that locally enhanced reflectivity features often appear as tilted features that are advected by the horizontal wind. Falling precipitation particles can bend sharply through layers of high wind shear. In different parts of a storm, regions with precipitation-sized ice corresponding to $Z > 0$ dBZ can be more spatially continuous (Fig. 1.8 top panel), as well as more spotty (Fig. 1.8 bottom panel). These mesoscale and convective scale details wash out at synoptic scales. The sounding data set utilized in this analysis is at 100 m scale in the vertical and could either hit or miss fine scale variability in the horizontal. While it is recognized that mesoscale and convective processes are relevant for winter storms (e.g. Ganetis et al. 2018; Keeler et al. 2016a), the research in this area is incomplete and the conceptual models have yet to be updated to account for this.

1.1.2 Reductions in Ice Mass from Sublimation

Significant environmental latent heat energy is consumed during the sublimation of ice precipitation, which cools the nearby air and can affect the thermodynamic stability of the storm. Harris (1977) modeled the sublimation of ice precipitation falling into a layer of still, $RH_{ice} <$ 100% air. Harris constructed different experiments of ice spheres falling into a subsaturated layer using the Marshall-Palmer precipitation particle size distribution (Marshall and Palmer

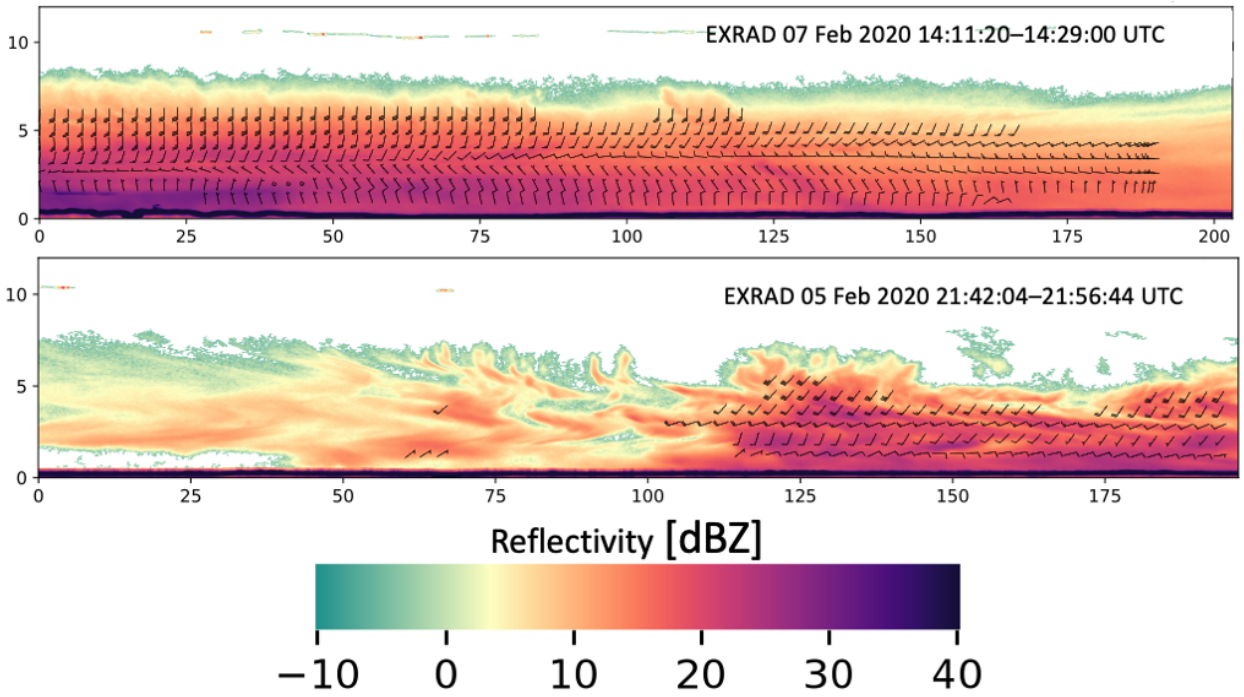

Figure 1.8: Example profiles of NASA ER-2 airborne radar EXRAD reflectivity and derived horizontal winds from NASA IMPACTS (McMurdie et al. 2022). (top panel) 200 km leg from flight on 7 Feb 2020. (bottom panel) 200 km leg from flight on 5 Feb 2020. Winds are shown for portions of flight legs with higher data quality. This airborne radar is more sensitive than NWS WSR-88D radars. Reflectivity values < 0 dBZ would typically have few if any precipitation-sized ice particles. Figure from Tomkins et al. (2022a)

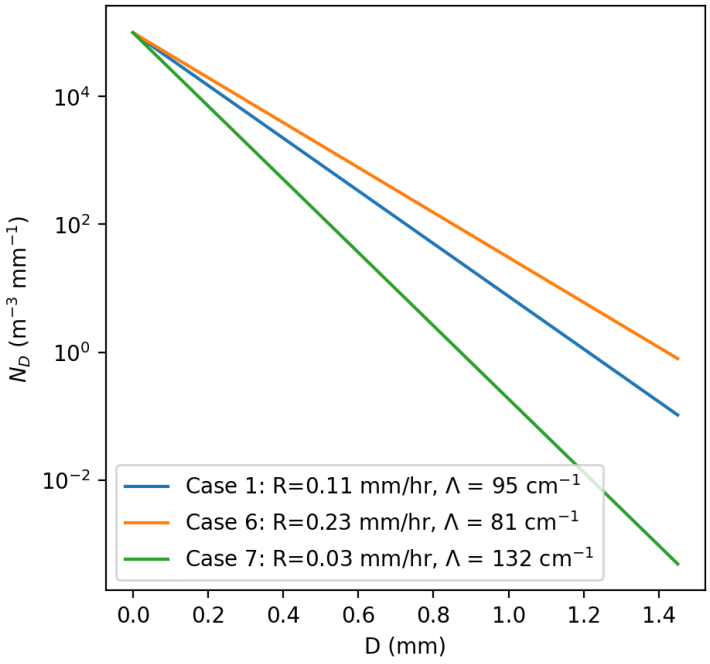

Figure 1.9: Selected ice particle size distributions from Harris (1977) used in his sublimation calculations. N_0=1 for each scenario.

1948): $N_D = N_0 e^{-\Lambda D_i} \Delta D$, where D is the diameter of the precipitation particle, N_D is the number of drops of diameter between D and ΔD, and N_0 is the value of N_D for D = 0. Marshall and Palmer (1948) found that Λ is a function of rain rate (R). Harris (1977) computed the effects of sublimation for several different scenarios of ice precipitation. Findings relevant to this study can be summarized by three of his scenarios; the ice particle distributions for these are shown in Figure 1.9.

Overall, the Harris calculations indicate that the most cooling occurs near the top of the $RH_{ice} < 100\%$ layer (Figure 1.10), where the large number of small ice precipitation particles completely sublimate shortly after entering the layer. For the light precipitation case (line 7, annotated green), this peak cooling occurs after 0.1 km of descent. There are significantly more large particles in the heavy precipitation case (line 6, orange) and these larger particles can descend further before this distribution reaches its level of maximum cooling around 0.2 km. From the experiments, the magnitude of cooling is shown to have the largest sensitivity to precipitation rate (R, mm h^{-1}). Heavy precipitation in case 6 has the greatest temperature reduction compared to the control (case 1), and light precipitation (case 7). Figure 1.11 shows how the cooling from sublimation alters the thermodynamic stability. Within the dry layer, layers above the level of maximum cooling have increased stability. Below this, stability is decreased proportionally to the magnitude of cooling and the depth of the cooled layer.

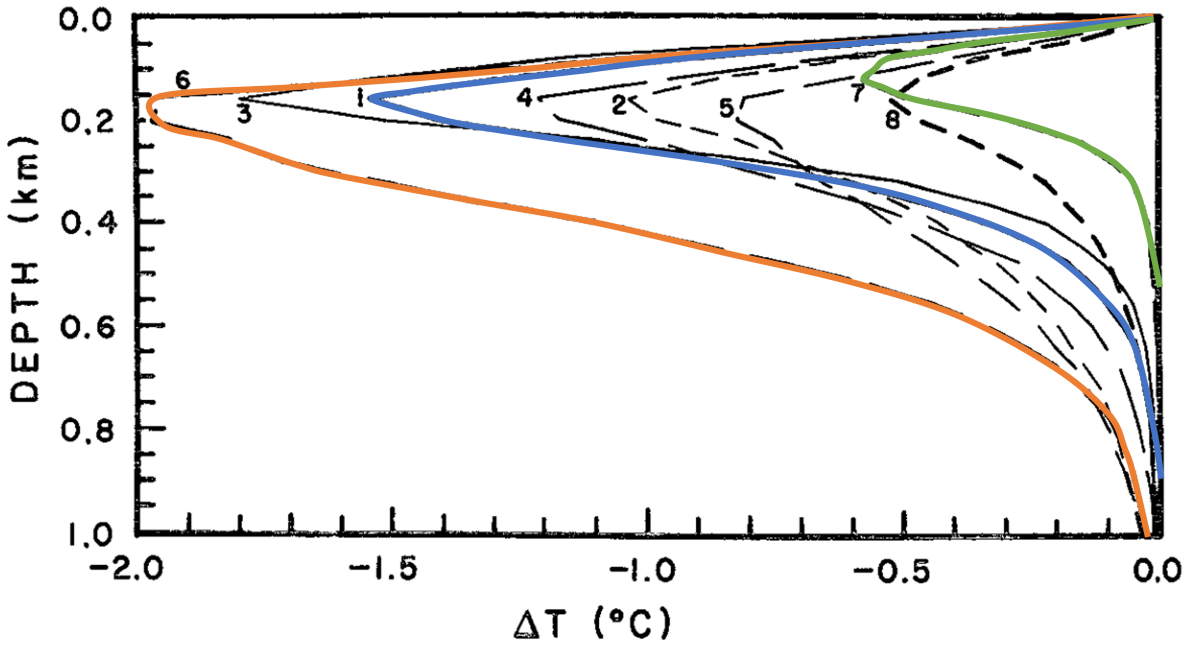

Fig. 1.10: Height profiles of air temperature deficit after 1 hr of sublimation for 8 experiments. Figure 5 from Harris (1977) with colors added. Colors correspond to ice particle size distributions from Figure 1.9.

Clough and Franks (1991) described how the sublimation of ice precipitation is different from evaporation of rain. They also used the Marshall-Palmer precipitation particle size distributions for both rain and snow falling into an environment with $RH_{water} = 60\%$. The depth over which precipitation mass is lost is shown in Figure 1.12 where line "a" is constant density snow and line "h" is rain.

Calculations show that 95% of ice precipitation mass is lost after only ~700 m compared to ~7,000 m for rain. Clough and Franks found that the low density and low terminal velocity of ice precipitation are the primary factors as to why ice precipitation can sublimate in a shallower depth than rain. Clough et al. (2000) modeled the dynamical effects of the sublimating ice precipitation, noting sublimation could enhance the descent of air parcels and create circulations around a front, but they did not find the stability changes predicted by Harris (1977).

These studies demonstrate that the time and depth scales for sublimation are much smaller than those for the evaporation of rain. Sublimation also occurs in conditions of very small subsaturations with respect to ice. This indicates that significant ice mass can be lost in a shallow layer of $RH_{ice} < 100\%$.

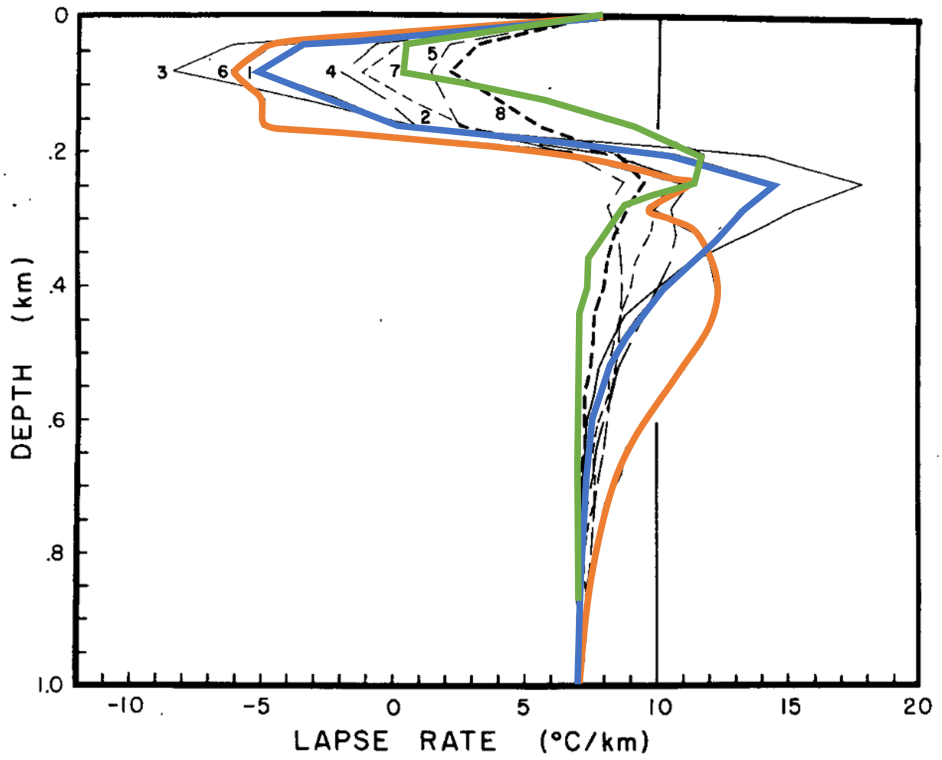

Fig. 1.11: Height profiles of air temperature lapse rate after 1 hr of sublimation for 8 experiments as in Figure 1.10. Larger lapse rates are less stable. Figure 6 from Harris (1977) with colors added. Colors correspond to ice particle size distributions from Figure 1.9.

Aircraft observations during the NASA IMPACTS field campaign (McMurdie et al. 2022) used both in-situ and remote measurements and found precipitation particles in conditions with $RH_{ice} < 100\%$ (Allen et al. 2021; Peele et al. 2021).

Images of individual particles that had partially sublimated were captured. One example is shown here in Figure 1.13. When the crystal formed it would have had sharp edges; the rounded edges in this image indicate that some of its original mass had sublimated. The sublimated crystal then experienced riming, as seen by the frozen droplets on the edges of the rounded branches. In the IMPACTS particle imaging data sets, many precipitation-sized particles were found in environments of $RH_{ice} < 100\%$ at altitudes above the lowest cloud base. This suggests that sublimation could play a critical role to reduce precipitation ice mass inside the vertical extent of the storm, not just below the lowest cloud base.

Aircraft observation campaigns are limited in time and space and hence represent small sample sizes. We desired to explore these $RH_{ice} < 100\%$ regions with another dataset: the archive of upper air radiosondes. Though radiosondes have temporal and spatial limitations

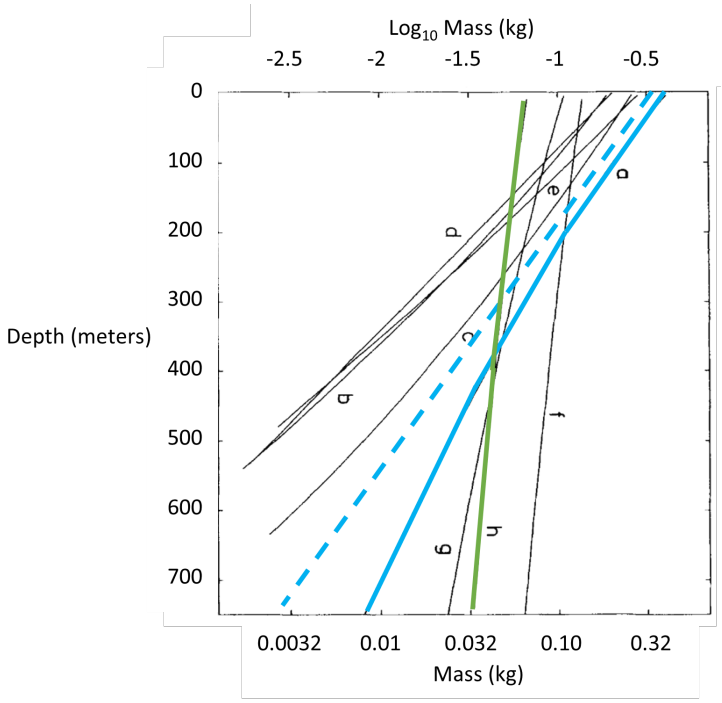

Fig. 1.12: Changes in precipitation mass after descending a given depth in an environment of 850 mb, 273 K, $RH_{water} = 60\%$. Solid blue line, a, is constant density snow (R=0.11 mm h^{-1}, N_0=0.025 cm^{-4}, Λ=18.8 cm^{-1}). Solid green line, h, is rain (R=0.11 mm h^{-1}, N_0=0.08 cm^{-4}, Λ=42.8 cm^{-1}). Dashed blue line is a straight reference line. The rate at which snow mass is lost slows as precipitation descends further into the dry environment. Based on Figure 3 from Clough and Franks (1991)

compared to an aircraft field campaign, they are launched frequently and provide excellent vertical resolution of the thermodynamics of the atmosphere. If layers of $RH_{ice} < 100\%$ and precipitation ice particles can be consistently detected within storms using radiosondes, that will provide strong evidence that sublimation is routinely reducing precipitation ice mass and affecting the structures of winter storms.

1.1.3 Increases in Ice Mass Associated with Instabilities

Cloud top instability can be manifested in generating cells which could serve as key sources for enhanced ice mass growth (Crosier et al. 2014; Evans et al. 2005; Herzegh and Hobbs 1980; Houze et al. 1981; Matejka et al. 1980; Plummer et al. 2014). This process is represented in Figure 1.14. An unstable layer near the top of the storm produces convective overturning, and the upward segments of this circulation locally increase the RH to enhance the growth of precipitation ice mass.

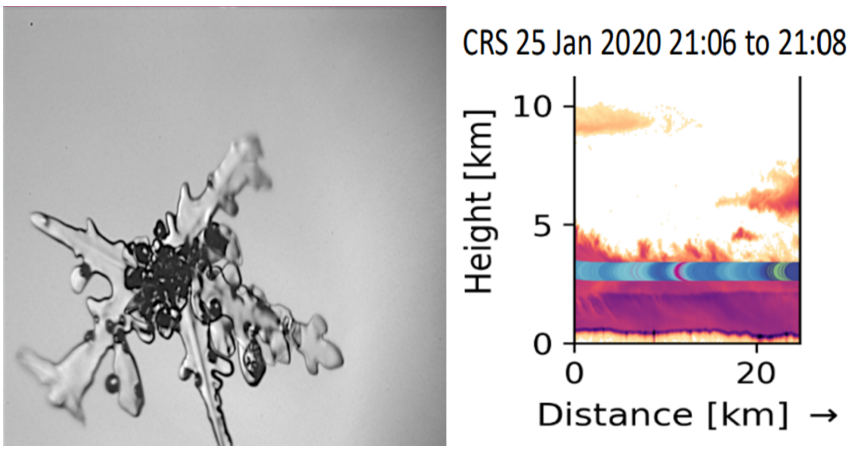

Fig. 1.13: Left: An ice particle captured by the Particle Habit Imaging and Polar Scattering (PHIPS) probe. Right. The RH_{ice} at the flight altitude of the PHIPS sensor when this image was collected ($\sim$ 3.5 km), overlaid on the vertical cross-section of reflectivity. $RH_{ice} > 95\%$ are colored green, $< 95\%$ are blue. Selection from Peele et al. (2021)

There are several possible sources of instability at and near cloud top. If the environmental lapse rate is between the saturated and dry adiabatic lapse rates, then the local environment is "conditionally" unstable. The condition for stability is whether the lifted parcel is saturated or not. If the lifted parcel is not saturated, it will cool quickly at the dry adiabatic lapse rate and become colder than the environment (i.e. stable condition). If the lifted parcel is saturated, it will cool slowly at the moist adiabatic lapse rate, and become unstable when it is warmer than the environment.

Dryer air above the moisture within the storm can create potential instability at the cloud top. Saturated air from inside the storm's vertical extent that is displaced upward will cool at the moist adiabatic lapse rate; this is slower than the dry air above the storm cooling quickly at the dry adiabatic lapse rate. Thus, if the layer of air across the storm top is lifted, the bottom of the layer will become warmer than the top, creating instability. Potential instability has been linked by previous studies to the occurrence of generating cells (Wexler and Atlas 1959; Kumjian et al. 2014)

Shear instabilities use energy from air motions to redistribute vorticity present in the shear layer. Vertical shear instability (a.k.a. Kelvin-Helmholtz instability) additionally must overcome the stable stratification from the atmosphere's density gradient in the vertical direction. For vertical shear instability to exist, the work required to overturn two parcels must be less than the kinetic energy extracted from the mean flow during the overturning. For saturated conditions, this requirement is met when the moist Richardson number is < 0.25 (see Section 3.5.2 from Markowski and Richardson (2010)).

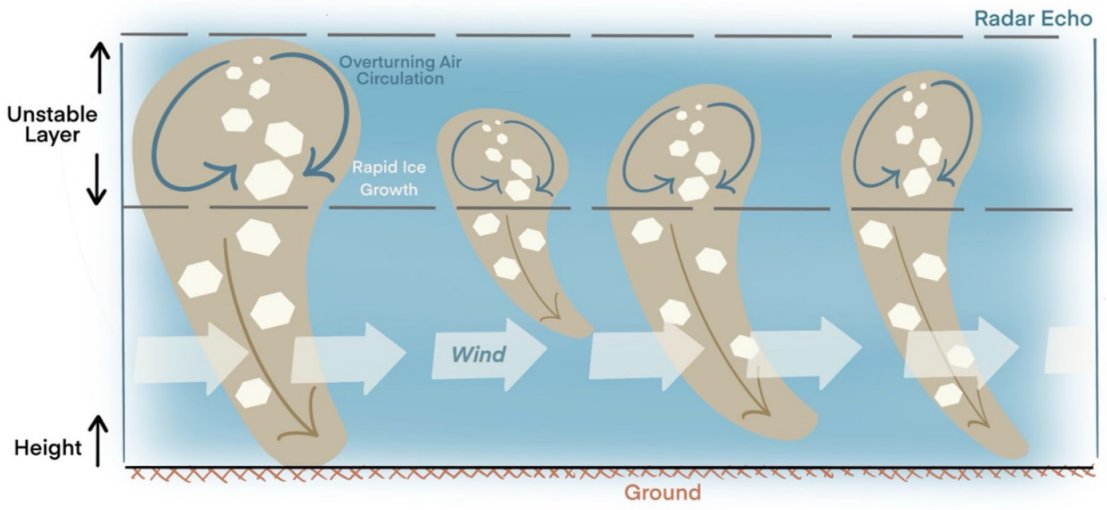

Fig. 1.14: Idealized depiction of generating cells and ice streamers in a time height plot. The upward branch of the overturning convective cell creates a local increase in RH which contributes to ice mass growth when $RH_{ice} < 100\%$. Figure 1.1 from Kent (2021)

A final source of instability considered here is cloud top radiative cooling. When longwave radiation emitted by the cloud top exceeds the incoming shortwave and long wave radiation, a cooler layer over a warmer layer of air develops and can yield convective overturning and generating cells (Keeler et al. 2016a). A modeling study by Keeler et al. (2016a,b, 2017) suggested that generating cells were more vigorous at night and attributed this to the enhanced radiative cooling when no incoming shortwave is present. However, a radar observational study by Kent (2021), which used ice streamers as a proxy for generating cells, did not find a robust diurnal cycle in ice streamers. She suggested that it was possible that the modeling study overestimated the differences between day and night radiation balances.

Figure 1.15 shows the possibility of a weak diurnal cycle with a slight increase in ice streamers near dawn (orange line). Kent performed Monte Carlo significance tests on several metrics of the ice streamer time series, and the results for the mean difference between the frequency of ice streamers between day and night are shown in Figure 1.16. The actual observed difference between the day and night ice streamer frequency is well below the 99% and 95% significance levels, indicating there is no significant difference in the frequency of ice streamers between the day and night periods. This lack of a robust diurnal cycle suggests that radiative cloud top cooling may not be a primary factor of cloud top instability.

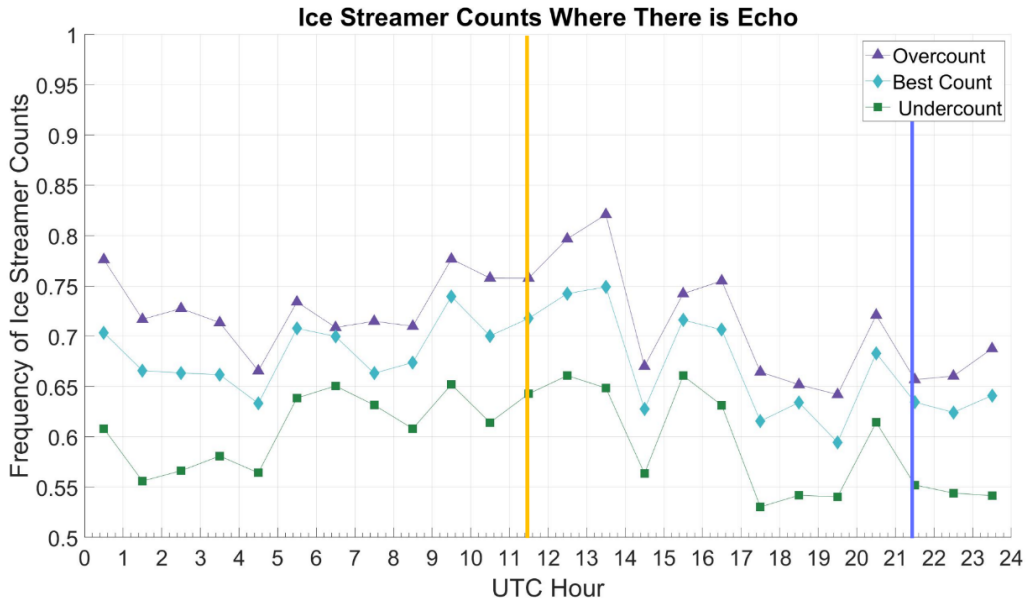

Fig. 1.15: Ice streamer counts divided by instances of echo for each hour. Three series represent different methods of counting ice streamers. Sunrise is marked by orange line; sunset by blue. Figure 3.7 from Kent (2021)

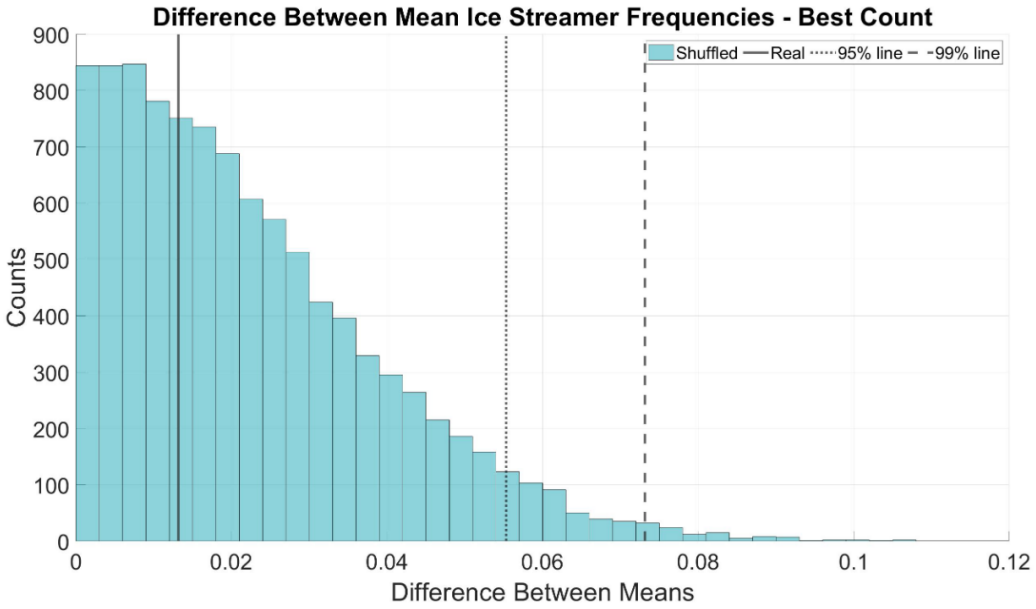

Fig. 1.16: Day/Night best estimate distribution of the difference between the six hour mean for the day (13 to 19 UTC, 0800 to 1400 local time) and the 6 hour mean for the night (0 to 6 UTC, 1900 to 0100 local time) of the shuffled Monte Carlo data of ice streamer frequencies. The 95th percentile and 99th percentile of the differences are the dotted and dashed lines. The difference between the actual 6 hour mean for the day and 6 hour mean for the night of the observed data is the solid line. Figure 3.16 from Kent (2021)

1.2 Road Map

Much of current winter storm research is fundamentally investigating the causes of the often large magnitude errors in quantitative precipitation estimation forecasts of snow fall (Kocin and Uccellini 2004). Research on the mesoscale precipitation structures within northeast US winter storms indicates snow bands and inferred locations of precipitation growth are not exclusively associated with regions of frontogenesis (Ganetis et al. 2018). As a result, research attention has shifted from slower, synoptic scale processes depicted in idealized conceptual models (e.g. Figs 1.5, 1.4, 1.6, 1.7), to shorter and smaller mesoscale and convective scale processes. This study aims to investigate two potentially relevant mesoscale to convective scale processes: 1) a possible source of ice mass loss within winter storms, namely sublimation of precipitation-size ice, and 2) where instabilities that would potentially increase ice mass by riming and/or vapor deposition are present.

This study will utilize a large data set ($>$ 1500 radiosondes) obtained in more than 700 winter storms in the northeast US since 2005. The radiosonde data set will be matched with surface observations as well as National Weather Service scanning weather radar data. This yields a unique view of observed vertical profile characteristics within winter storms in a spatial framework relative to the low pressure center of the storm.

Details on the data and methods are presented in Chapter 2. Analysis of the geographic spatial patterns and vertical distributions of key variables related to moisture and instabilities within the storm are presented in Chapter 3. Specific hypotheses that were tested and associated evidence are described in Chapter 4. Key findings and suggestions for future work are summarized in Chapter 5.

As it turned out, most of our inferences based on the NASA IMPACTS data sets turned out to be mistaken when evaluated with the multi-decade upper air sounding archive. All the testable hypotheses from the Ph.D. prospectus are examined in Chapter 4. Each hypothesis was either rejected or had insufficient information to be robustly evaluated. These negative results are instructive and valuable for showing the lack of relevance of sublimation of precipitation-sized ice within the vertical extent of the cloud.

On the positive side, the more exploratory observation analysis presented in Chapter 3 is compared to expected conditions inferred from idealized conceptual models and will be the focus of the journal articles based on this work. It is important to note that the radiosondes observations (with caveats for measurement uncertainty) represent the real world with more fidelity than reanalysis, which is a blend of assimilated observations and numerical models.

CHAPTER

2

DATA AND METHODS

2.1 Radiosonde Data

Radiosondes (aka upper-air soundings) are the key data set for this analysis. The radiosonde's measurements of pressure, air temperature, moisture, and wind are foundational for deriving information on the vertical profiles of cloud, instabilities, and environments for precipitation particle growth and shrinkage. Since August 2005, high-resolution sounding data, with temporal resolution as high as 1 second, have been made available for many sites globally (National Centers for Environmental Information and Yin 2021). These high-resolution soundings yield several thousand vertical measurements for a single sounding profile and provide new details on shallow layers within storms that were not previously accessible with lower resolution data. This sounding data is stored by NCEI in Binary Universal Form for the Representation of meteorological data (BUFR) format (World Meteorological Organization 2022). For the purposes of this analysis, we focus on continental United States sounding launch sites north of 33°N and east of 94°W where winter storms with snow and/or mixed precipitation frequently occur.

Variables from the BUFR soundings used in this study are listed in Table 2.1. The time and latitude/longitude displacement since launch are converted to a UTC timestamp and geographic coordinate, respectively, based upon the launch time and location. Additional parameters are computed from these variables; these calculations are detailed in Appendix B.

Table 2.1: Sounding variables used from BUFR sounding format

Variable	Units
Time since launch	s
Pressure	Pa
Geopotential height	m
Latitude displacement since launch	degree
Longitude displacement since launch	degree
Air Temperature	K
Dewpoint Temperature	K
Wind Direction	degree, True
Wind Speed	m/s

2.1.1 Derived sounding characteristics within layers

Some parameters (e.g. wind shear, lapse rates, conditional and potential instability) must be considered over a layer of the atmosphere instead of at an individual measurement level. These layers need to be computed from regular height intervals, but the sonde does not take measurements at specified altitudes or height intervals. Therefore, the high-resolution sounding measurements are linearly interpolated to regular height values. If the sounding measurement is more than 10 meters above/below the target height, the interpolation is not permitted. These interpolated measurements are used to compute the layer properties. The variables computed for layers are listed in Table 2.2.

Table 2.2: Derived variables for atmospheric layers

Element	Units
Potential Temperature Lapse Rate	K/km
Equivalent Potential Temperature Lapse Rate	K/km
Equivalent Saturation Potential Temperature Lapse Rate	K/km
Wind shear	s^{-1}
Pseudo-Adiabatic Lapse Rate	K/km
Moist Richardson Number	dimensionless

We examined layer thicknesses of 50 m, 100 m, 250 m and 500 m and found that 100 m worked best for the purposes of this study. Fovell and Gallagher (2020) found that sounding wind measurements below 250 m AGL often have large errors related to GPS altitude and wind anomalies. Following their recommendation, we do not utilize any variables derived from wind direction or speed data < 250 m AGL in this analysis.

2.2 Low-Pressure Center Detection

Idealized conceptual models of extratropical cyclones indicate the location of surface fronts, frontal surfaces, and the associated stability profiles, moisture profiles, and cloud conditions for different quadrants relative to the low pressure center (see Figure 1.1). As part of the analysis, the observed characteristics derived from the upper air soundings are put into spatial context relative to the low pressure centers of winter cyclones so that findings can be related to previous work.

Mean sea level pressure reanalysis data from the ERA5 (Hersbach et al. 2018) from 2005 to 2023 was used to find the locations of synoptic-scale low pressure centers relevant to the region (25°- 55°N, 90°– 60°W) and time period of this analysis (L. Tomkins, personal communication). Synoptic-scale low pressure centers were required to have at least a 7.5 mb / 1000 km gradient somewhere within 200 km of the low pressure center and a pressure minimum less than 1010 mb. We designate low pressure centers meeting these criteria as "trackable lows". Spatial and temporal checks were employed to prevent erratic, nonphysical movement of the identified lows.

This procedure yielded 690 days with 701 low pressure centers that occurred between August 2005 and January 2023. The low tracks are shown in Figure 2.1.

The nearest low pressure center to each NWS soundings launch location and time was determined, and sounding observations within 500 km of synoptic low pressure centers were retained for further analysis.

From the over 5,400 soundings in the domain during winter months, there were 1,635 soundings within 500 km of a trackable low pressure center. Of these, 45 had missing data and/or anomalous measurements that prevented some of the data processing steps. These soundings were omitted, yielding 1,590 valid soundings within 500 km of 424 unique trackable low pressure centers. The median number of soundings per cyclone track was 3 (the mean was 3.75 and maximum was 14 soundings per track). Additional subsets of the data based on weather conditions are enumerated in Table 2.3.

Figure 2.2 shows the location of soundings with and without surface precipitation relative to the low pressure center. Soundings associated with precipitation at the surface (described

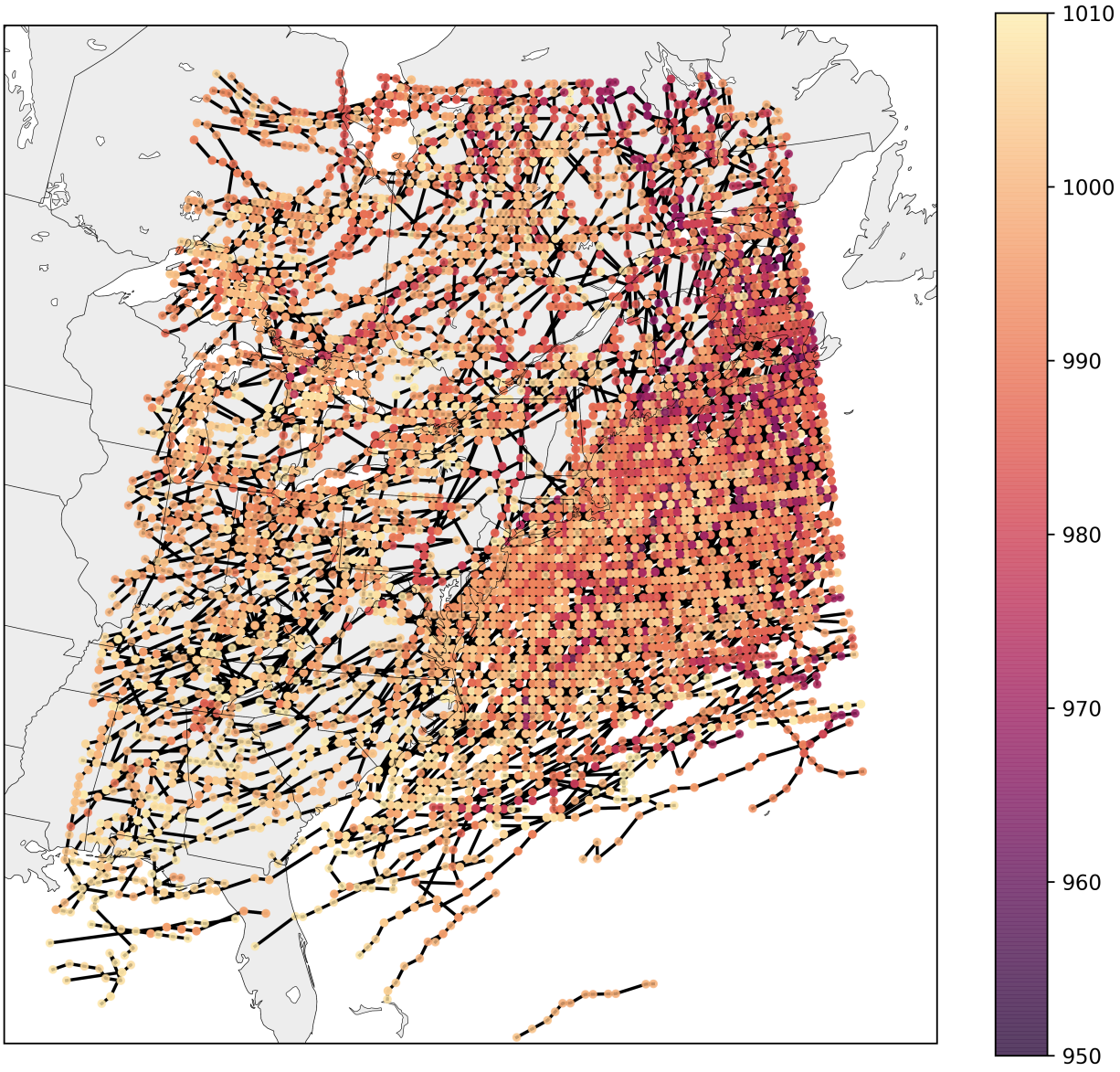

Figure 2.1: Path of all 701 trackable lows from August 2005 to January 2023. Minimum pressure in mb along the path is color-coded. Figure courtesy of L. Tomkins

Table 2.3: Sounding subset totals

	With surface precipitation	Without surface precipitation
Within 500 km of trackable lows	1,025	565
Within 500 km of trackable lows and surface temperatures <0 °C	522	243

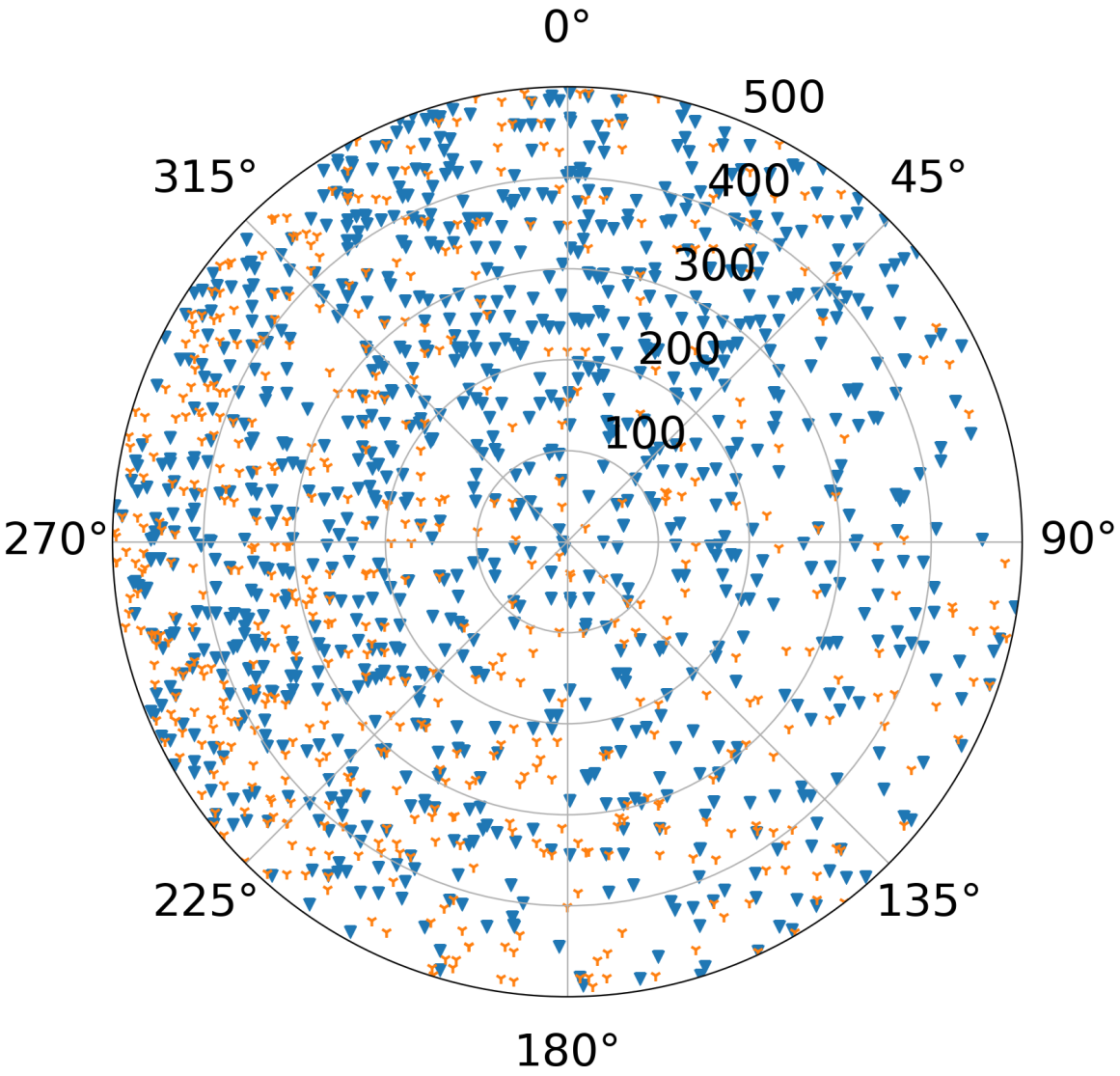

Figure 2.2: Cyclone-relative positions of soundings within 500 km radius of trackable low pressure centers. Soundings with surface precipitation are marked with blue, filled triangles and soundings without surface precipitation are marked with orange "Y"s.

in Section 2.2.1) are marked with filled triangles. Soundings without surface precipitation are marked with a "Y". This marking scheme will be used throughout the paper. Figure 2.2 additionally uses color to separate precipitating (blue) from non-precipitating (orange) soundings. Since in the northeast US many winter low pressure systems have low centers offshore in the Atlantic Ocean (e.g. Ganetis et al. 2018), there are more sounding samples to the west of the low pressure center. Figure 2.3 illustrates the 950 mb wind direction and speed measured by the soundings. The expected counter-clockwise circulation around the low pressure center is clearly displayed.

2.2.1 Conditional selection based on weather conditions

Proximity to a low pressure center during midlatitude winter months does not guarantee that a particular sounding is measuring the characteristics of a storm with surface snowfall. Surface observations from Meteorological Aerodrome Reports (METARs) will be used to conditionally select soundings that have surface characteristics associated with surface snowfall, such as temperatures < 0 °C and precipitation. This study will categorize any precipitation type (snow, rain, mixed, unknown, etc) observed with surface temperatures below freezing as a precipitating case. METARs are a type of surface observation reported from airports around the globe and their sensors are routinely maintained to preserve the safety of flight operations. Use of METARs will ensure a standard of quality and reliability for the surface observations. The Integrated Surface Dataset, ISD, (Smith et al. 2011) is the source for historical METARs in this study. In order for a METAR to be associated with a radiosonde, the sounding launch site and the METAR observation must be within 50 km of each other. Surface observations within a 3 hour window (1 hour prior or 2 hours after the sounding launch time) will be deemed as 'concurrent' with the sounding.

A relational database using Structured Query Language (SQL) is used to organize the surface and upper air data. SQL queries can then be used to select a subset of the data *based on conditions specified for both the surface and upper air observations*. For example, soundings with cloud bases below 2 km in the northeast quadrant of the low pressure center that had surface precipitation with surface temperatures below freezing can be easily subset from the larger database.

2.3 Radar Data

In this analysis, weather radar reflectivity measurements are paired with the sounding to determine if the sonde was collocated with precipitation-sized particles. The capability to

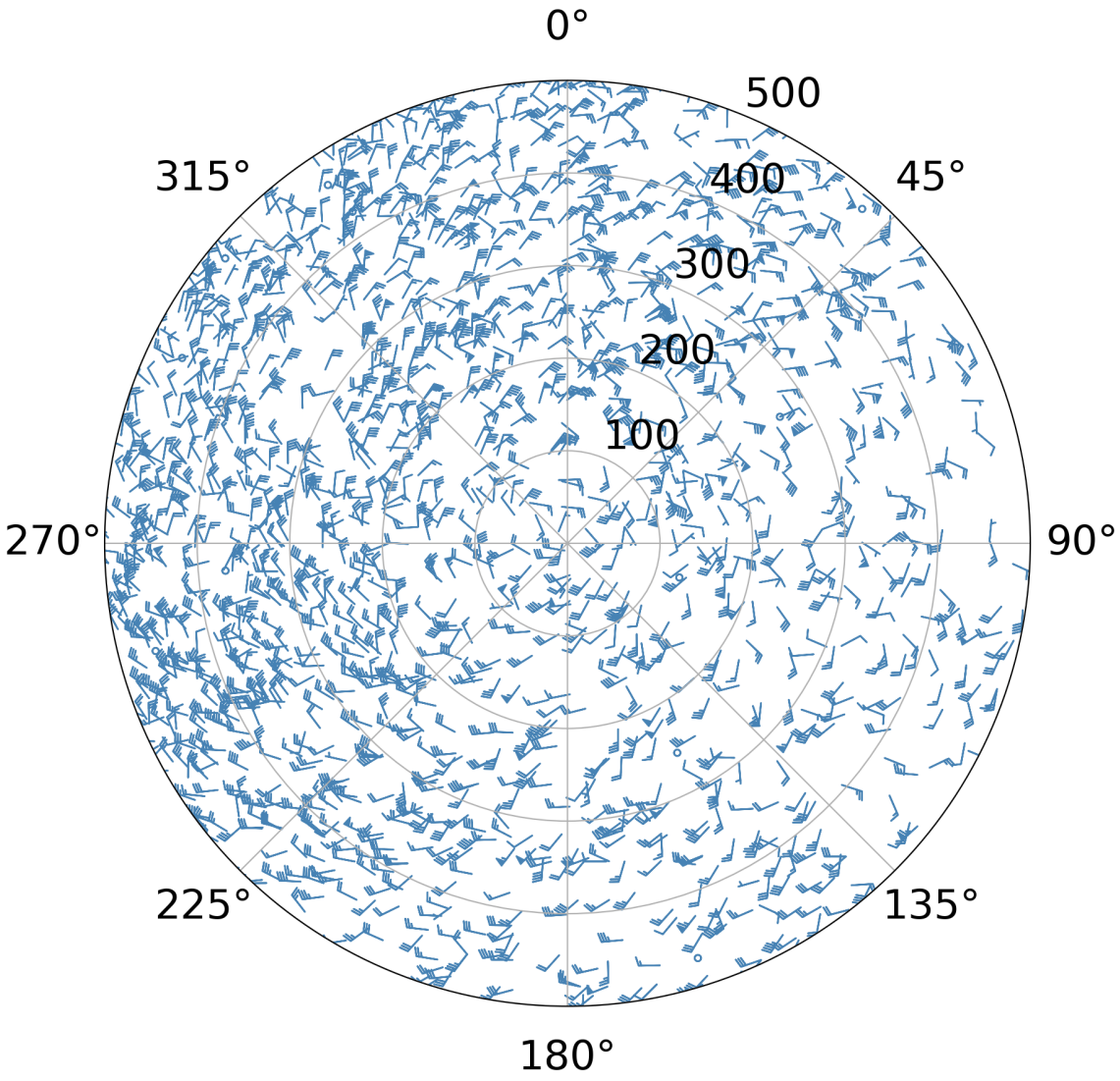

Figure 2.3: 950 mb wind speed (kts) and direction at cyclone-relative positions of soundings within 500 km radius of trackable low pressure centers. Expected cyclonic rotation is clearly depicted.

determine the radar reflectivity along the sonde's 3D path in the atmosphere is not available in standard skew-T plots and has not been previously used for a large sample size. The radar data is from Next Generation Weather Radar (NEXRAD) network accessed via Amazon Web Services (Registry of Open Data on AWS 2022).

The location and timestamp for each level of the sonde is referenced to the closest and most recent radar data to determine if an echo is present at that location and altitude. It takes several minutes to complete a radar volume coverage pattern (VCP) consisting of a set of elevation angles. Since a typical sonde flight is over an hour, multiple radar scans occur as it ascends. Radar scan times matched to a given sonde location and time are based on the most recent scan available at that time.

Radar data is read using the Python ARM Radar Toolkit (Helmus and Collis 2016) and converted to Cartesian coordinates. SciPy (Virtanen et al. 2020) is used to create a kd-tree (Maneewongvatana and Mount 2002) that allows for fast interpolation of the sonde's location to the nearest radar reflectivity measurement. The Cartesian altitude of the radar observations assumes standard atmospheric refraction of the radar beam (Helmus and Collis 2016). Computing the beam geometry with standard refraction assumes the Earth's effective radius, R', is 1.333 times the actual radius, R_e (Barton 2013). The magnitude of the radar beam altitude error in meters increases with increasing distance from the radar antenna. The median surface distance from all sonde positions to the nearest NEXRAD is 36.5 km. At this distance, the estimated altitude error from non-standard refraction is less than 100 m. At the maximum distance of 248 km, the vertical error is estimated at over 1 km. These values are computed using non-standard refraction between $1.1R_e$ and $1.6R_e$.

The "cone of silence" directly above the radar geographic location in the VCP is a common cause for why a sonde's position may not intersect any radar beam. Over 40% of radiosonde launch sites in the United States are located within 5 km of a NEXRAD site, so the sonde needs to drift a horizontal distance of 7-10 km or more before the radiosonde intersects with the highest VCP elevation angle (usually 19.5°). Additionally, the NEXRAD VCPs typically have vertical gaps, especially between higher elevation angles. When the sonde is not within the radar beam, no radar data will be matched to that measurement (i.e. marked as missing). The combination of these factors can result in significant data gaps in the vertical profile of the radar data (see Figure 2.4).

When considering vertical layers (described in 2.1.1), over 50% of the layer depth is required to have radar coverage in order to assign a radar measurement to a given sounding layer. If the coverage requirement was met, the highest observed reflectivity in the layer was assigned for the entire layer. In this analysis, reflectivity is used only to determine if precipitation-sized particles were present or not, so this method is deemed sufficient. The depth of layers used in

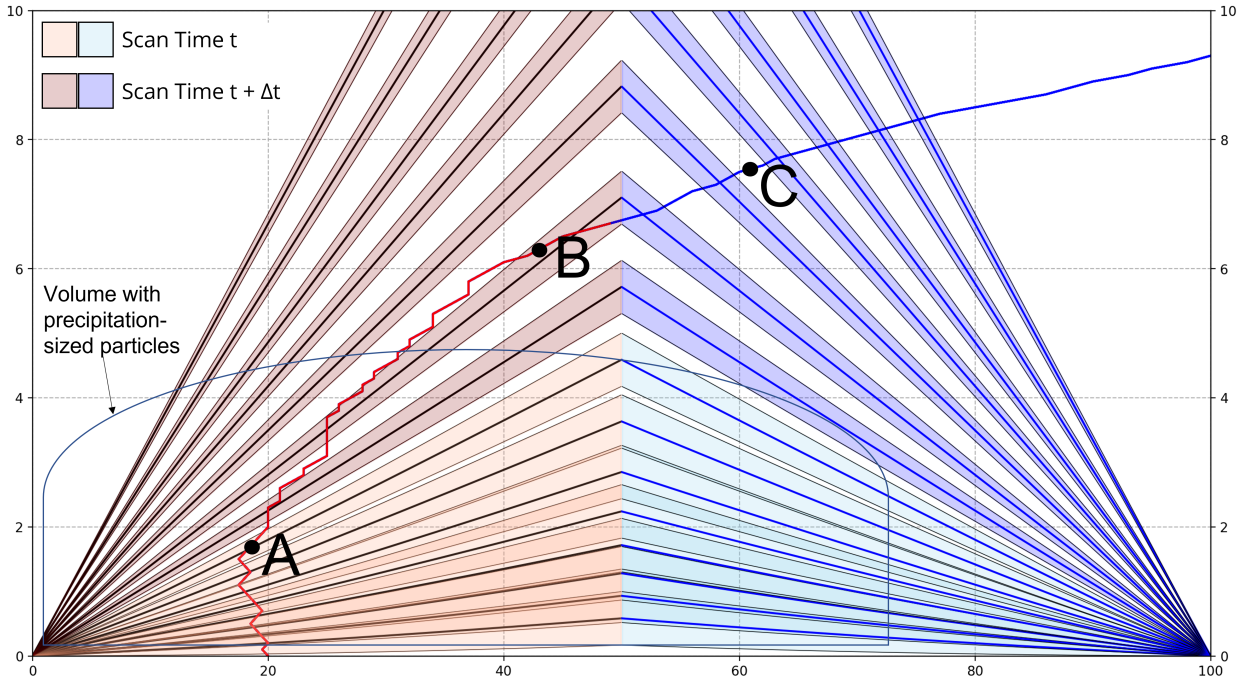

Figure 2.4: A hypothetical sounding trajectory through VCPs scanned by two neighboring NEXRAD sites. As the sounding ascends from the surface and then through A to B to C and beyond, the balloon moves horizontally with the wind and the sonde passes through different elevation angles of the radar scan. Points A and B are matched with data from the radar on the left. Point C is matched with data from the radar on the right. Horizontal and vertical axis units are km.

the sounding analysis are usually smaller (100 m) than the radar vertical beam width (> 500 m at ranges from the radar > 30 km). Radar beam filling will tend to decrease the radar-observed reflectivity in the radar resolution volume when variability in precipitation ice water contents smaller than the radar resolution volume are present. We use a 0 dBZ threshold to denote the presence of precipitation-size particles in the NWS radar data.

Most VCPs have more scans at low elevation angles (Office of the Federal Coordinator for Meteorological Services 2011). Thus, the distribution of sounding altitudes with radar coverage is skewed to lower altitudes, as shown in Figure 2.5A.

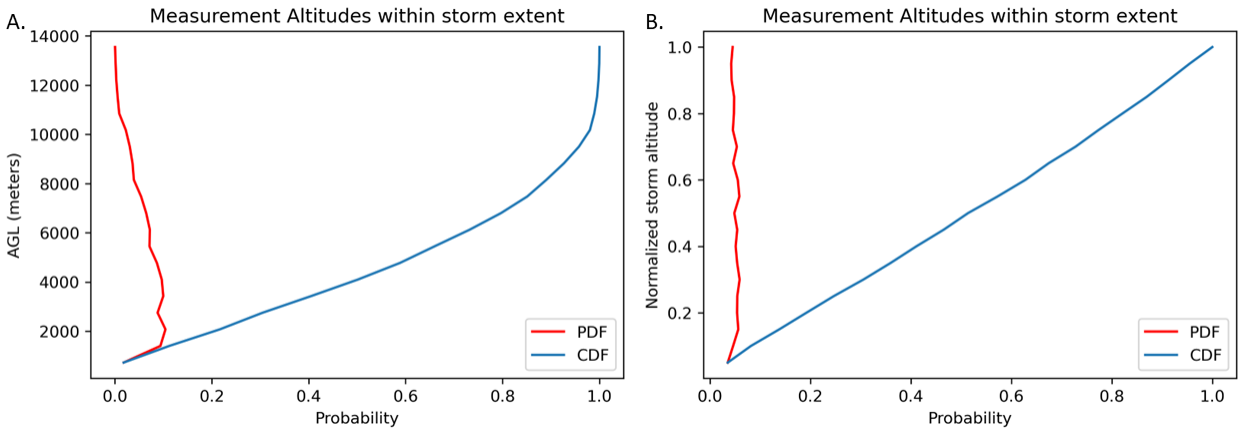

Figure 2.5: Probability Density Functions (PDF) and Cumulative Distribution Function (CDF) for the altitude of soundings measurements with radar coverage within the storm vertical extent. Panel A is altitude AGL; Panel B is storm relative altitude

This suggests there should be fewer radar measurements near the tops of storms. After transforming the altitude above ground level (AGL) to a storm-relative altitude (see Section 2.5), Figure 2.5B shows that radar coverage within the storm extent for the entire database is fairly uniform. Figure 2.6 shows the raw counts and normalized fraction of reflectivity values in the storm relative altitude (defined later in Section 2.5.2). The lowest storm relative altitude has the highest count and fraction of sonde measurements that are outside of radar coverage. This is due to 1) measurements below the lowest radar beam and 2) the sonde ascending through the cone of silence. There are slightly more sonde positions outside of radar coverage (indicated by boundary between gray and black shading in Fig. 2.6B)in the top half of the storm extent than the bottom half (the mean count per altitude bin without radar coverage in the top half is 3418 compared to 3210 in the bottom). This sampling discrepancy is attributed to the increase of gaps between radar beams at high altitudes (see Fig 2.4), but the decrease in

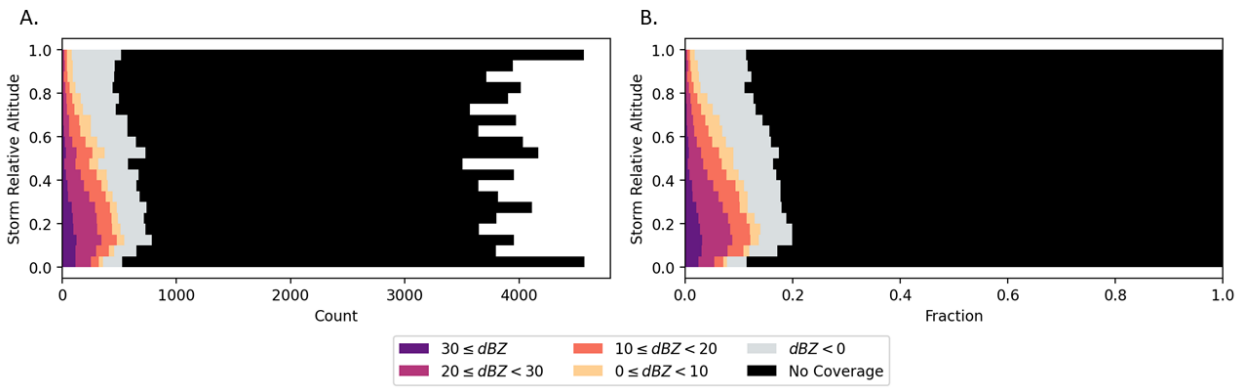

Figure 2.6: Stacked histogram of radar measurements paired to all sonde positions within 500 km of trackable pressure centers in the storm relative altitude. Panel A is the observation count at each altitude; Panel B is normalized by the number of observations in each altitude bin.

available observations is small.

2.4 Stability, Ice, and Radar Multiplots

The skew-T/log-P thermodynamic diagram is a very common tool for visualizing atmospheric soundings, but many of the indices and methods used in skew-T analysis are designed for summer, surface-based convection and are ill-suited to understanding processes within winter storms. For example, the air temperature and dewpoint lines clearly indicate where liquid phase cloud is present (when dewpoint = air temperature), but not ice phase cloud. Lifting Condensation Level provides a metric of liquid phase cloud base for buoyant surface parcels, but not for ice phase cloud base.

A new Stability, Ice, and Radar matched multiplot (SIR plot) for winter storm analysis is described here. The main goal of these plots is to simplify interpretation of the juxtapositions of thermodynamic and stability conditions at any one level (examine graphs along a given altitude) as well as their vertical variability. The combination of sounding-measured and derived variables with the NEXRAD radar data along the sounding trajectory is a new and original way to view and analyze winter storms characteristics. The SIR plots also illustrate several key variables derived from the soundings and used in this analysis.

An example SIR plot is show in Figure 2.7. It is composed of seven sub-plots designed to highlight features in the vertical distribution of stability, saturation, and precipitation-sized particles. Along with the dry-bulb and dewpoint temperatures, the wet-bulb and frost-point temperatures are plotted to show layers with potential for evaporative cooling and ice formation, respectively. The wet-bulb temperature is a better estimate of the temperature on the surface

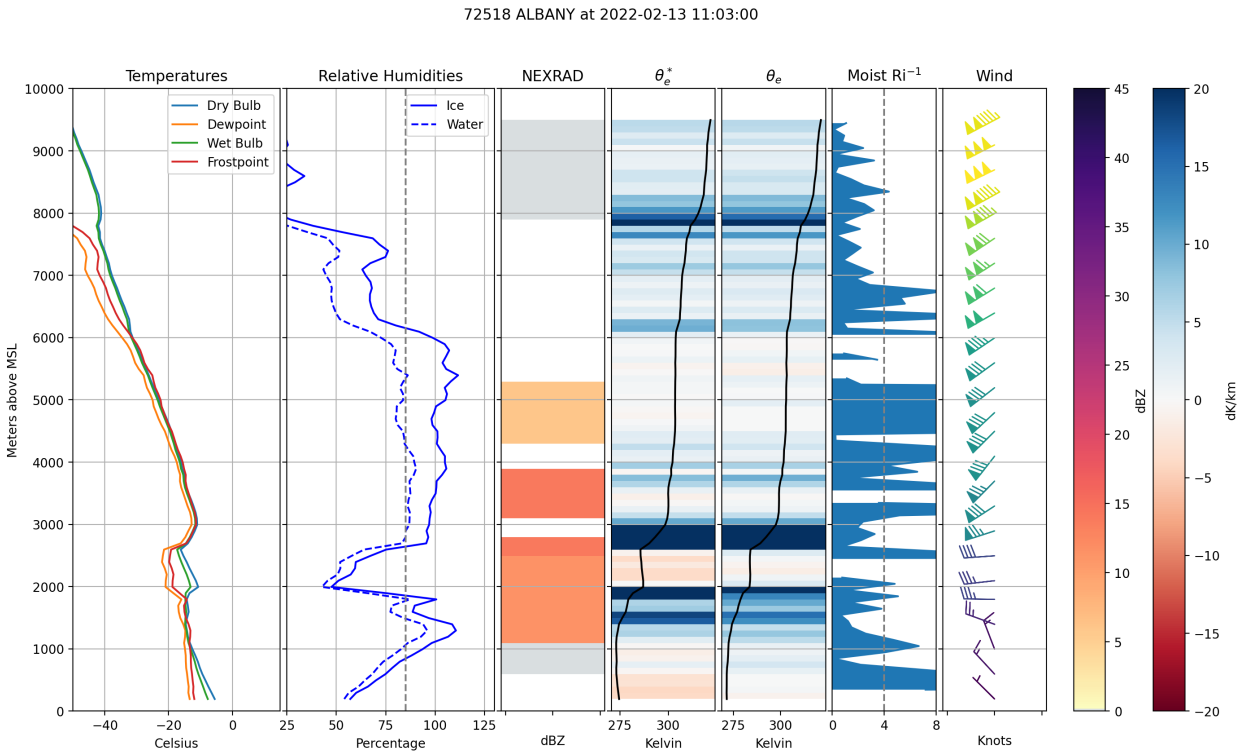

Figure 2.7: An example SIR plot for the Albany, NY sounding launched on 2022-02-13 at 11:03UTC. Components of the plot and meteorological significance are discussed in Section 2.4.

of a precipitation particle than the ambient air temperature. It is also better at distinguishing "warm noses" when ice particles cross over to temperatures > 0°C. RH_{ice} is shown to identify layers where ice clouds can exist. RH_{water} close to 100% is necessary for persistence of cloud water and potential riming locations. Relative humidity = 85% is marked by a dashed line, and serves as an approximate lower bound between regions with and without ice clouds (see Section 2.5 for further discussion of RH_{ice} thresholds for ice cloud detection).

The reflectivity measurement valid at the sonde's position indicates if precipitation-sized particles were present. A perceptually uniform color scale utilized by Tomkins et al. (2022b) prevents undue focus on arbitrary reflectivity thresholds. When the sonde is inside the radar beam, but the measured reflectivity is below the lowest desired threshold, that level is plotted in gray (no echo). When the sonde is outside of the radar beam, that vertical level is left blank (white, missing data) because no measurement occurred.

Local, layer by layer, conditional and potential instability are depicted by the profiles of saturation equivalent potential temperature (θ_e^*) and equivalent potential temperature (θ_e), respectively. The θ_e^* and θ_e lapse rates are additionally color coded along with the temperature trace. Layers where θ_e^* or θ_e decrease with height are unstable and shaded in red.

Local, layer static stability is part of criteria needed to assess non-local static stability that accounts for the motions of rising and sinking parcels (Stull 1991).

Shear instability is represented by the moist Richardson number (mRi) and the wind profile. The moist Richardson number is calculated using the moist Brunt-Väisälä frequency, which represents buoyant oscillations in a saturated environment. Since these stability metrics are being used to assess structures within storms, the moist version of the Richardson number is more appropriate than the "dry" Richardson number. Vertical shear instability occurs when the vertical shear of the horizontal motion yields sufficiently strong vorticity to overcome the static stability of the layer (Houze 1993). This threshold is called the critical Richardson number (Ri_c); when the Richardson number is < 0.25 conditions are favorable for Kelvin-Hemmholtz instability and turbulence to develop. Once started, turbulent motions can persist in conditions up to mRi=1.0. The inverse of the mRi is shown in the SIR plot. This is so that layers where instability could exist are easily identifiable as $mRi^{-1} > 4$, and layers with little wind shear where $mRi \rightarrow \infty$ are visually minimized. At the far right of the SIR plot, wind barbs are plotted to illustrate the wind shear component of the shear instability. Regardless of the vertical resolution of the data, a maximum of only 25 wind barbs are plotted to prevent the chart from becoming too cluttered.

The example SIR plot in Figure 2.7 shows subsaturated conditions below 1000 m and between 1900-2800 m. Matched reflectivity measurements indicate that while there were precipitation-sized particles above 1100 m, they do not persist in the dry conditions below that

level. Higher reflectivity values above 2800 m transitioning to lower values alongside the dry layer suggest that sublimation is occurring there. The conditional instability around 2800 m also exhibits the stable over unstable profile expected from sublimation as modeled by Harris (1977). Potential instability has a similar, but weaker signal. The estimated cloud top around 6100 m is accompanied with decreased conditional and potential instability. Vertical shear instability increases with a strong layer of speed shear above cloud top. Much of the profile between 3000-5400 m has vertical shear instability but very little wind shear; this is due to the nearly neutral conditions present in these layers.

2.5 Cloud boundaries from RH_{ice}

While $RH_{water} = 100\%$ works well in practice for defining cloud boundaries for liquid phase cloud, aircraft in situ data obtained by NASA IMPACTS (McMurdie et al. 2022) indicates cloud-sized ice particles are often present for RH_{ice} down to $\sim 85\%$ (Figure 2.8, L. Allen, personal communication).

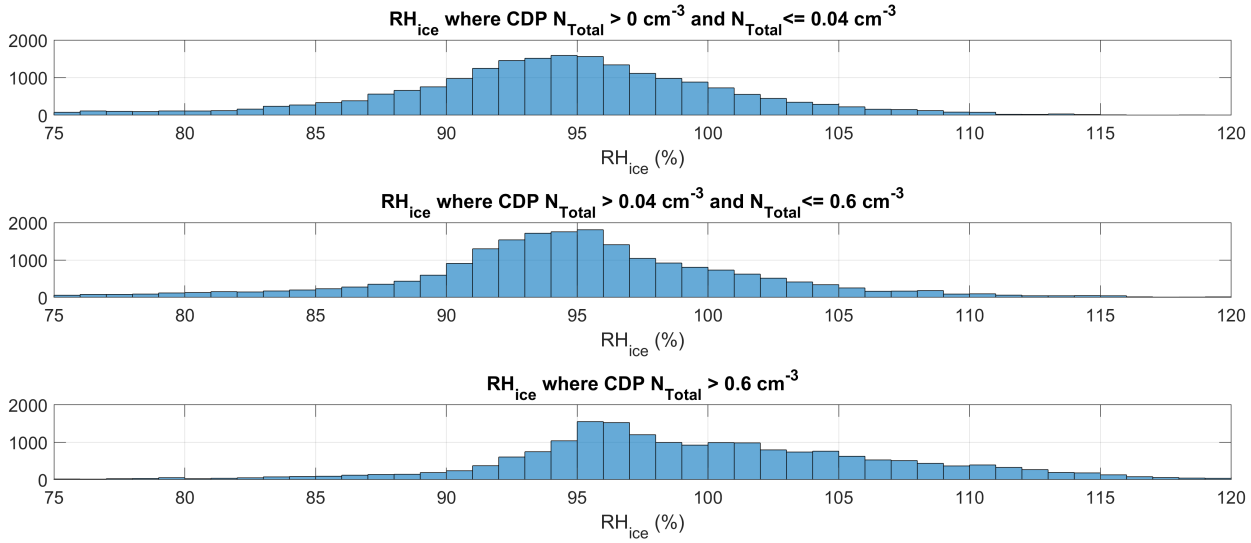

Figure 2.8: Cloud Droplet Probe (CDP) histograms of RH_{ice} in cloud particle concentrations (N_T) between (top panel) 0 and 0.04 cm^{-3}, (middle) > 0.4 and <= 0.6 cm^{-3}, and (bottom) > 0.06 cm^{-3}. In the lowest concentrations of cloud ice particles (top panel), over half of the observations have $RH_{ice} < 95\%$. Figure courtesy of L. Allen, data from NASA IMPACTS (McMurdie et al. 2022).

There are some indications that the dewpoint sensor on the NASA P-3 aircraft may have accuracy issues (M. Miller personal communication). These issues will likely not be resolved until the legacy dewpoint sensor is compared against a laser hygrometer (which was deployed in January and February 2023, data is not expected until after September 2023). Comparison of RH_{ice} at the altitude of ASOS ceilometer cloud base did not reveal a single robust threshold to use for ice cloud boundary detection (Fig. 2.9), but suggests that $RH_{ice} = 85\%$ is a reasonable lower bound.

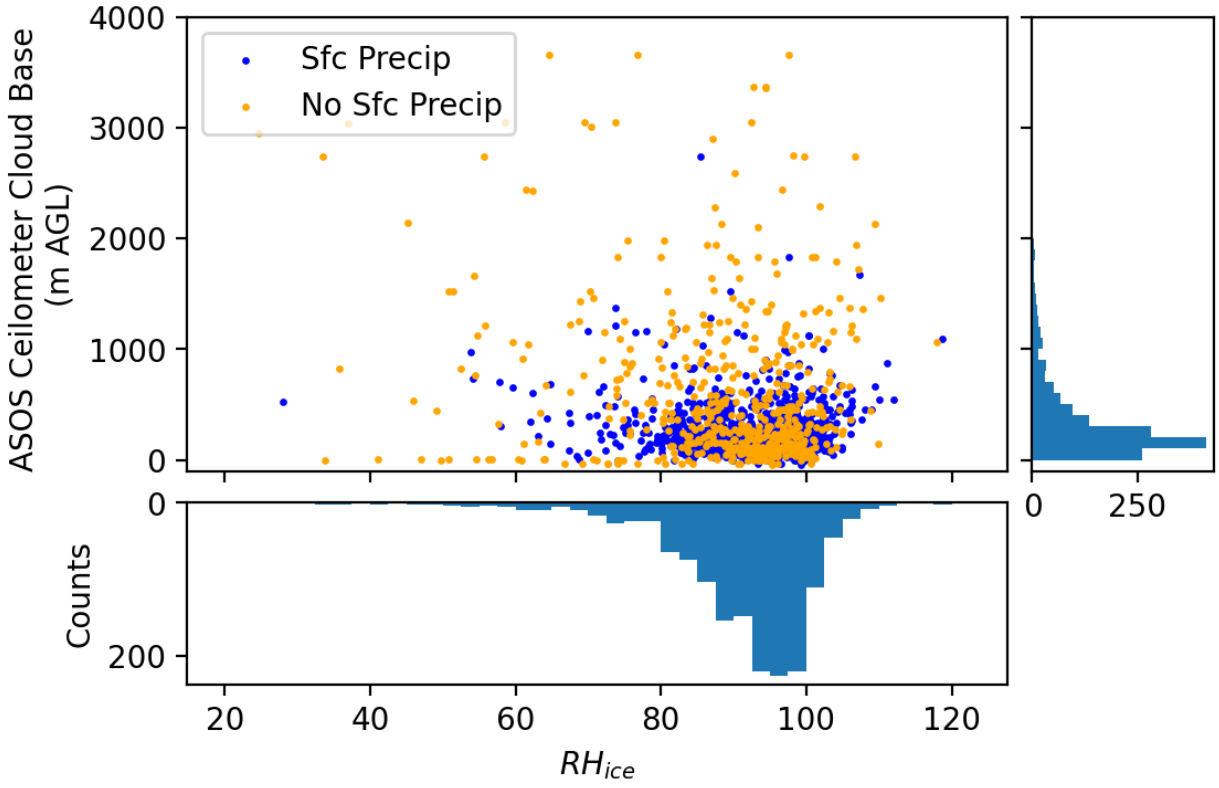

Figure 2.9: Scatter plot of RH_{ice} at the ASOS ceilometer cloud base altitude for all 1,590 soundings within 500 km of trackable lows. Histogram at right shows distribution of ceilometer cloud base heights. Histogram at bottom shows distribution of RH_{ice} values. Points are color coded whether the sounding is associated with surface precipitation.

2.5.1 Cloud Base

Two methods of estimating the cloud base from sounding variables were attempted. First, cloud base was estimated at the lowest altitude where a single level (~5 mb) of RH_{ice} meet either the

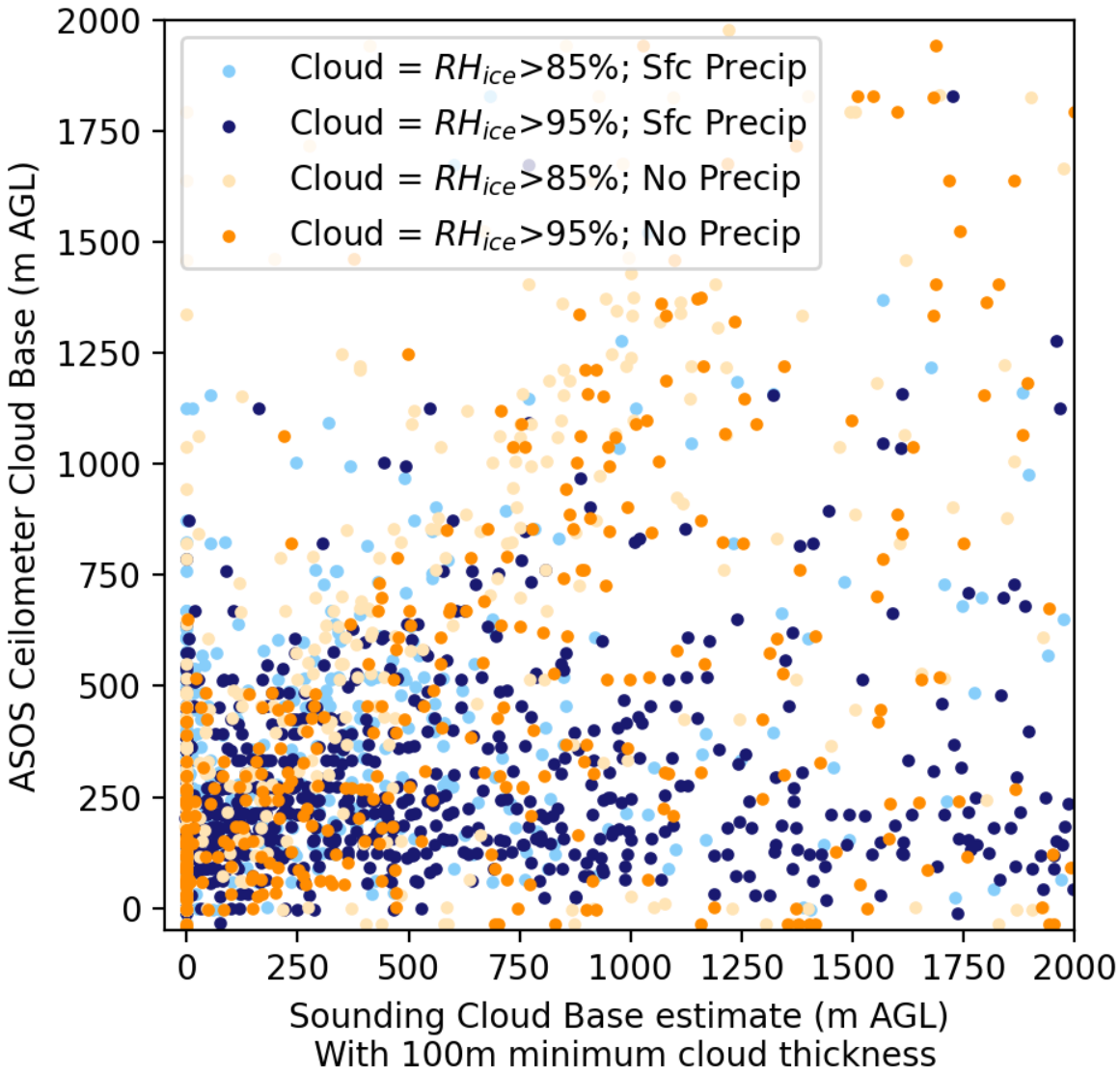

Figure 2.10: ASOS ceilometer cloud base compared to the lowest height of a contiguous layer with $RH_{ice} \geq 85\%$ and $\geq 95\%$ that is more than 100 m thick. Values are compared for all 1,590 soundings within 500 km of trackable lows.

85% or 95% threshold (not shown). Second, RH_{ice} meeting either threshold was required to extend vertically for a contiguous 100 m before the base of that layer was designated as the cloud base (Fig. 2.10). The second method was used to prevent single levels of high RH_{ice} in otherwise dry conditions from being marked as the cloud base. Both methods performed poorly compared to the ASOS ceilometer cloud base. Exceptionally high RH values in precipitating conditions and fog/mist conditions at the surface were key factors for underestimating cloud base heights compared to the ceilometer.

For the purposes of this analysis, we used the ASOS ceilometer to determine cloud base altitude above ground level. This sensor is widely used by the aviation community which has a vested interest in accurate cloud base measurements. Ceilometer observations were paired with the sounding data in time and space as described in Section 2.2.1 with a few additional steps. The minimum ceilometer cloud base AGL in the 3 hour time window was selected to represent the lowest cloud base for the sounding. The ASOS elevation was added to the ceilometer measurement to obtain the cloud base above MSL. The elevation of the sounding launch location was used to convert the MSL cloud base to AGL relative to the sounding's location.

2.5.2 Cloud Top

Unfortunately, there are no operational sonde-independent measurements of cloud ice boundaries above cloud base. We use a range of RH_{ice} values to bracket the likely cloud ice boundaries and examine the sensitivity of our findings to the different thresholds. We use $RH_{ice} = 85\%$ as a lower bound and use $RH_{ice} = 95\%$ as an upper bound. These values are informed by the NASA IMPACTS data analysis.

The estimate of the highest cloud top from the sounding data was the highest altitude in the profile where RH_{ice} was greater than the chosen threshold. The median difference between cloud top height estimates using $RH_{ice} = 95\%$ versus 85% was only 124 meters; 63% were less than 500 m different and 73% were less than 1 km (Figures 2.11 and 2.12). Additionally, the $RH_{ice} = 95\%$ threshold would sometimes leave large vertical extents of reflectivity above the estimated cloud top, suggesting this threshold was too strict. For the purposes of this analysis, $RH_{ice} = 85\%$ was selected as the threshold for the ice cloud boundaries.

The overall qualities of the following analysis are not sensitive to the differences in defining cloud top using $RH_{ice} = 95\%$ versus $RH_{ice} = 85\%$. To illustrate this, selected figures from Chapters 3 and 4 are recomputed using the $RH_{ice} = 95\%$ threshold and included in Appendix A.

The total vertical extent of a winter storm will be defined between the *lowest* cloud base

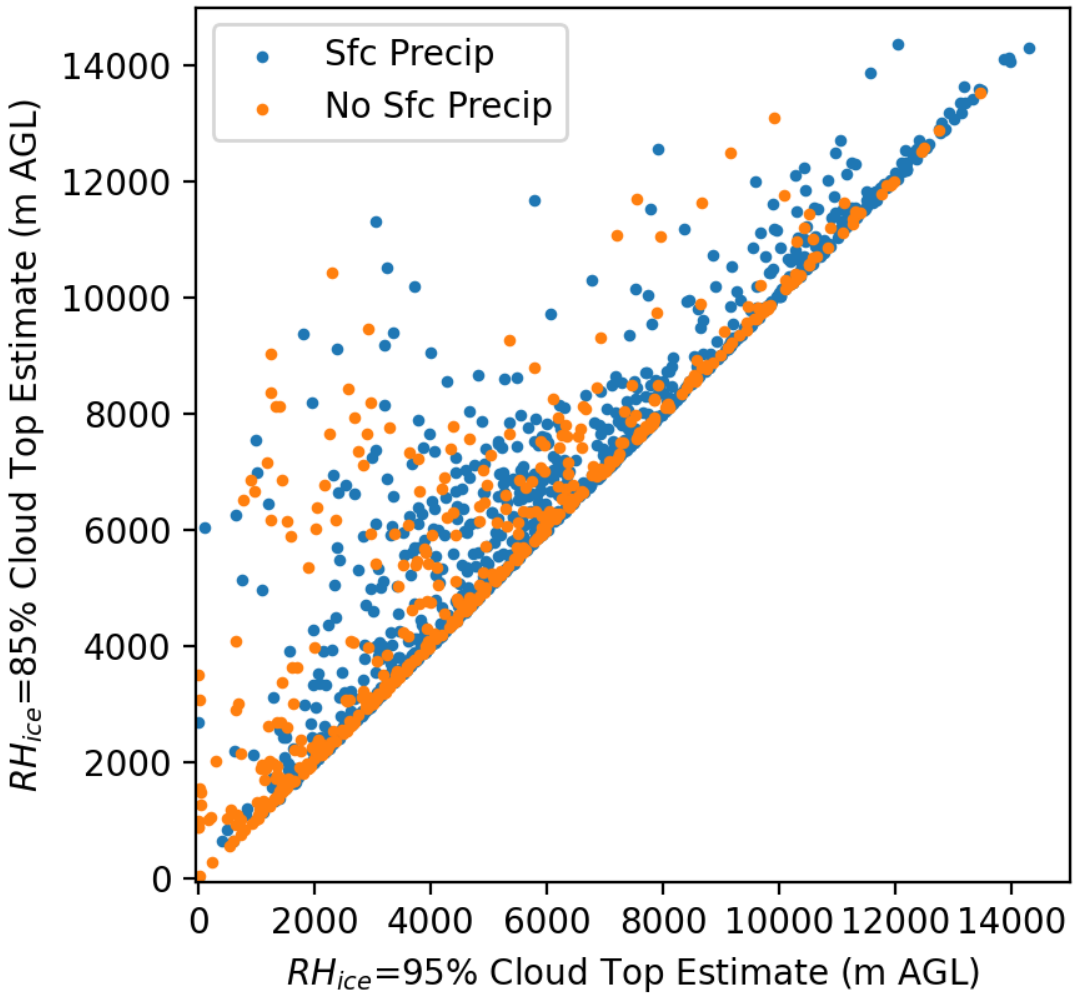

Figure 2.11: Comparison of cloud top height estimates using RH_{ice} thresholds of 85% and 95%. Values are compared for all soundings within 500 km of trackable lows.

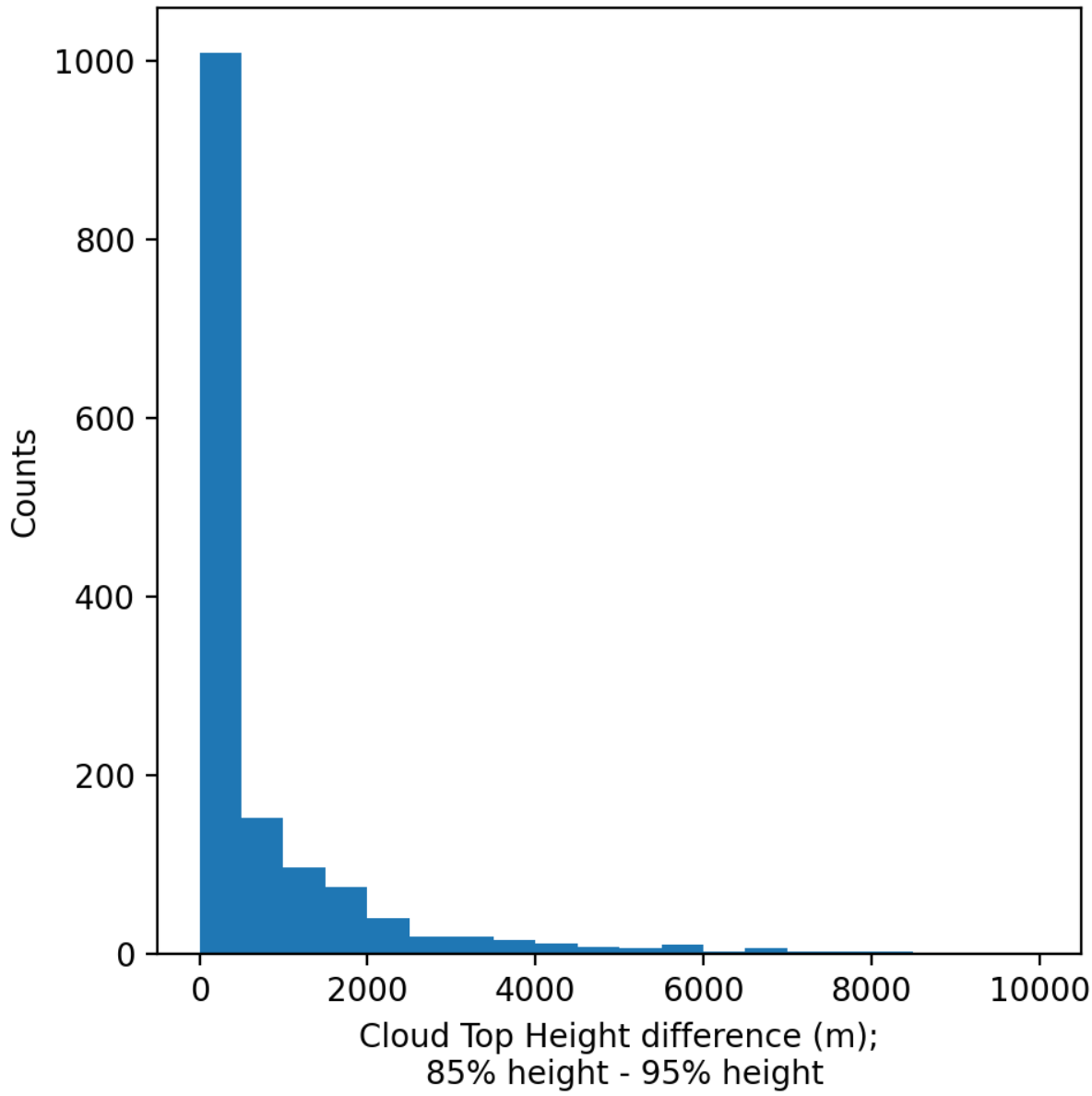

Figure 2.12: Histogram of cloud top height differences using RH_{ice} thresholds of 85% and 95%. Values are compared for all soundings within 500 km of trackable lows.

and *highest* cloud top. A storm relative altitude Z_{sr} is defined as:

$$Z_{sr} = \frac{Z - Z_{cb}}{Z_{ct} - Z_{cb}}$$

where Z is a given altitude, Z_{cb} is the height of the lowest cloud base, and Z_{ct} is the height of the highest cloud top (all heights are above ground level).

CHAPTER

3

RESULTS

3.1 Low-relative sounding parameter mosaics

3.1.1 All soundings

We present several storm parameters as mosaics in a low pressure center relative framework to illustrate the variability of characteristics of actual snowing winter storm data. Each point represents one sounding (or the ASOS data matched to that sounding). As described in Section 2.2 the median number of soundings for a given cyclone track is 3. These plots aggregate the information in the sample used and can be compared to simplified conceptual models. These plots also provide context for the results of hypothesis testing in Chapter 4. Initially we will consider soundings that are matched to lows, regardless of the minimum pressure. The pattern of soundings with surface precipitation was previously shown in Figure 2.2.

The minimum ASOS temperature associated with the soundings are shown in Figure 3.1. The warm sector from the conceptual model (Figure 1.1) is depicted in this mosaic.

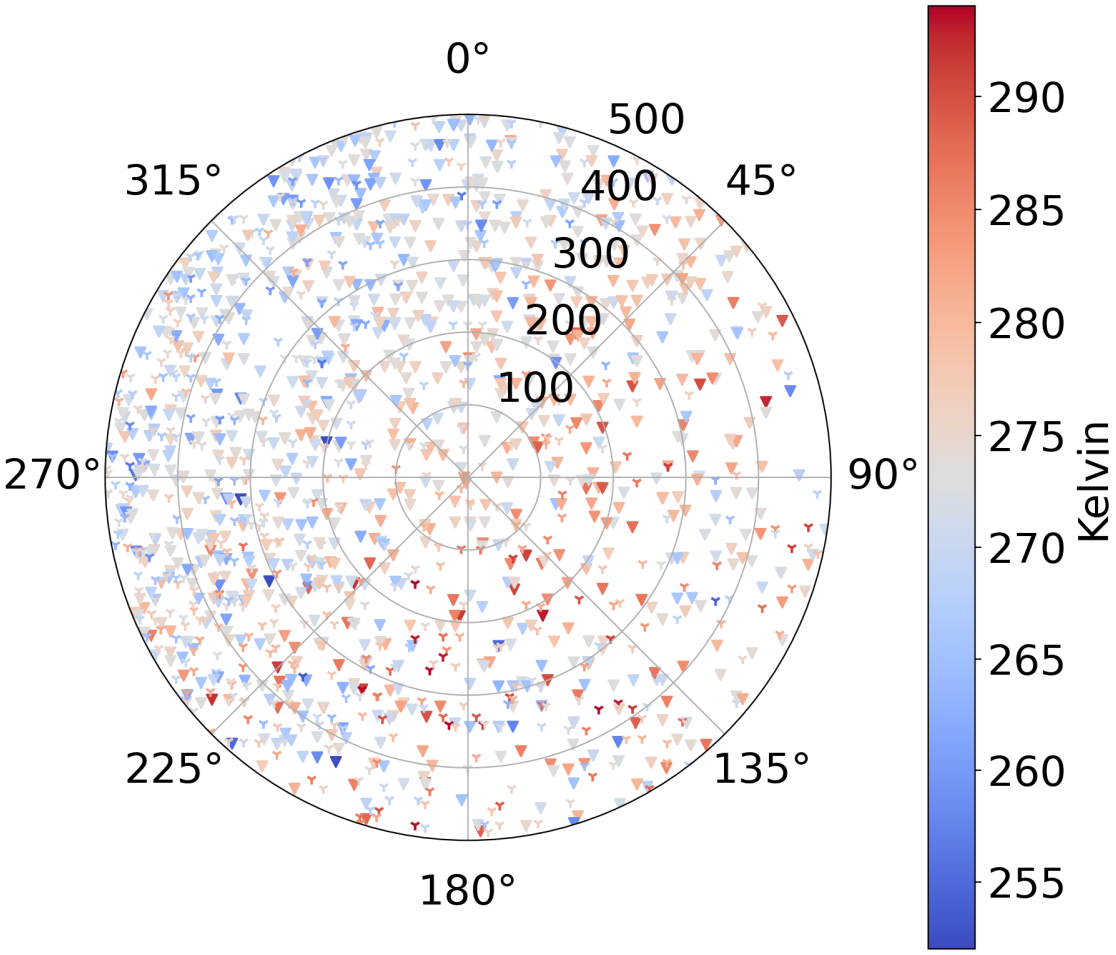

Figure 3.1: Mosaic of ASOS surface temperatures relative to trackable low pressure centers within 500 km. Soundings with surface precipitation are marked with a filled triangle. Soundings without associated surface precipitation marked with a "Y".

3.1.2 Subset of soundings with surface temperature < 0 °C and precipitation

As summarized in Table 2.3, the full dataset has 1,590 soundings within 500 km of trackable lows. The hypotheses tested in Chapter 4 focus on the effects of sublimation, so soundings with significant melting should be excluded. Therefore, ASOS temperatures are required to be below freezing. This alone does not guarantee that precipitation reaching the surface is frozen, but it is a good approximation. This requirement reduces the number of available soundings to 765, and is also detrimental to the spatial distribution of observations since surface temperature is not uniformly distributed. To ensure that significant precipitation processes were occurring within the storm, the corresponding ASOS was also required to have observed precipitation of any type (snow, rain, mixed, unkown, etc...) concurrent with the sounding. Thus the final number of soundings available for interrogation was 522. Versions of the following figures for the 243 soundings without surface precipitation are included in Appendix C.

Relative Humidity with Respect to Ice

As described in Section 2.5, the estimate of cloud top is determined only by the vertical extent of RH_{ice}. Plotting this estimate relative to the low pressure center (Figure 3.2) shows the tallest clouds to the north of the low pressure center. This pattern agrees with typical cloud distributions about an extratropical cyclone (see Figure 9 from McMurdie et al. (2022), reproduced here as Figure 1.3). Since the distribution of the ASOS lowest cloud base relative to the low pressure center is fairly uniform (Figure 3.3), the pattern of the storm depth relative to the low pressure center (not shown) is quite similar to the pattern of cloud tops.

In addition to plotting aspects of RH_{ice} relative to the low pressure center, all the sounding profiles of RH_{ice} with surface temperatures < 0 °C and precipitation are shown in Figure 3.4. The profiles are first sorted by their cloud top heights, shown as black dots, then base the ASOS ceilometer cloud base, shown as orange. This sort method based on the cloud boundary is applied to all compilations of profiled variables. (Note: colors of the cloud top and ASOS ceilometer cloud base change for the different profiles to allow for improved contrast.)

A significant number of the precipitating sounding profiles have areas of no ice cloud (RH_{ice} < 85%). These dry regions occur most often in the top half of the storm's vertical extent, but there are several examples below 2 km AGL. All of the no-ice-cloud regions within the storm's extent offer potential to sublimate ice particles of any size.

The total depth of layers with RH_{ice} < 85% within the storm extent is shown relative to the low pressure center in Figure 3.5 and as a histogram in Figure 3.6 for soundings within 500 km of trackable lows with surface temperatures < 0 °C. Over half of the soundings (both with and without associated surface precipitation) have some dry layers within the storm extent. For

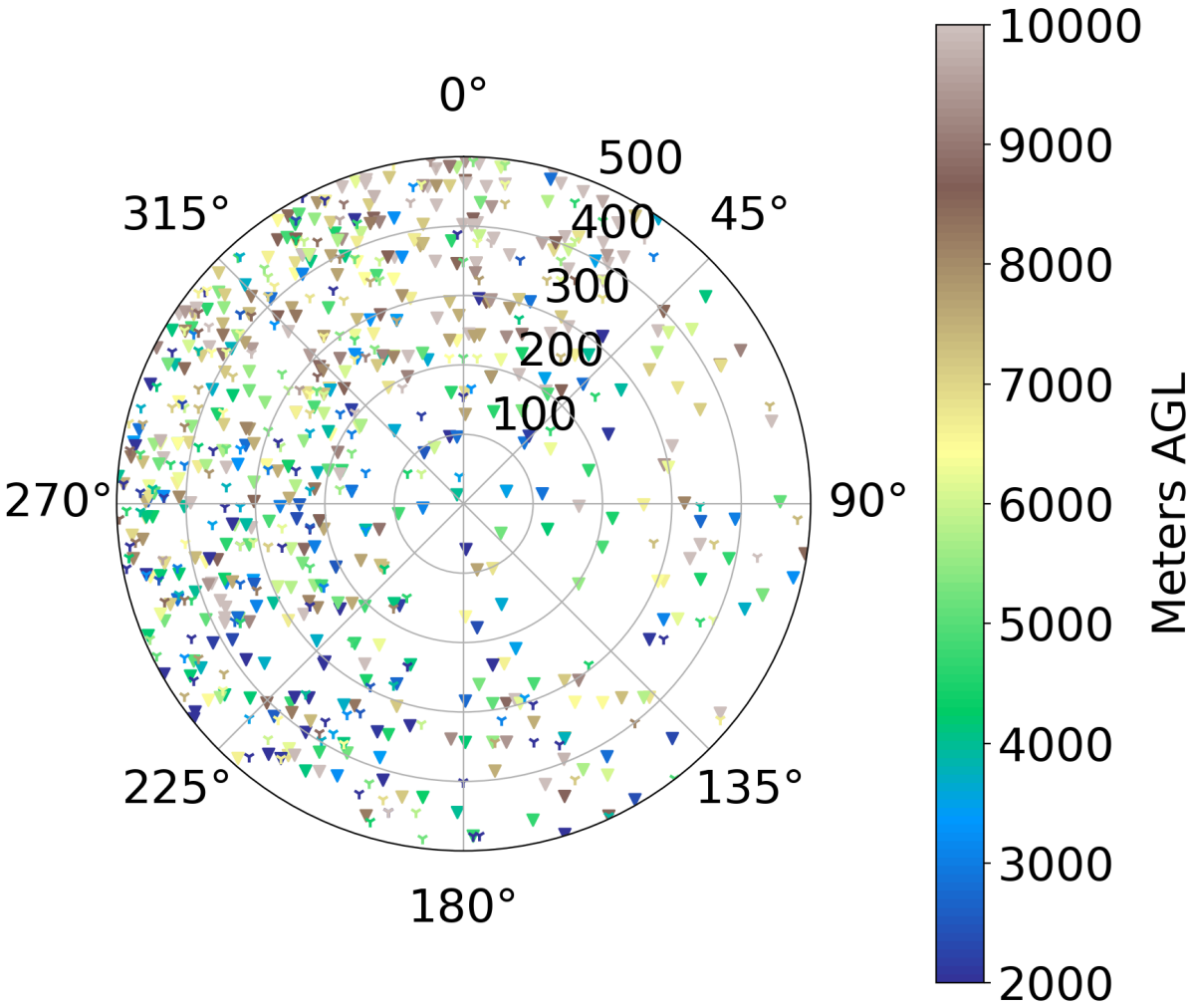

Figure 3.2: Mosaic of cloud top altitude relative to trackable low pressure centers for soundings with surface temperatures < 0 °C. Soundings with surface precipitation are marked with a filled triangle; without surface precipitation marked with a "Y". Color coding is cloud top altitude. Higher cloud tops are most prevalent north and northwest of the low.

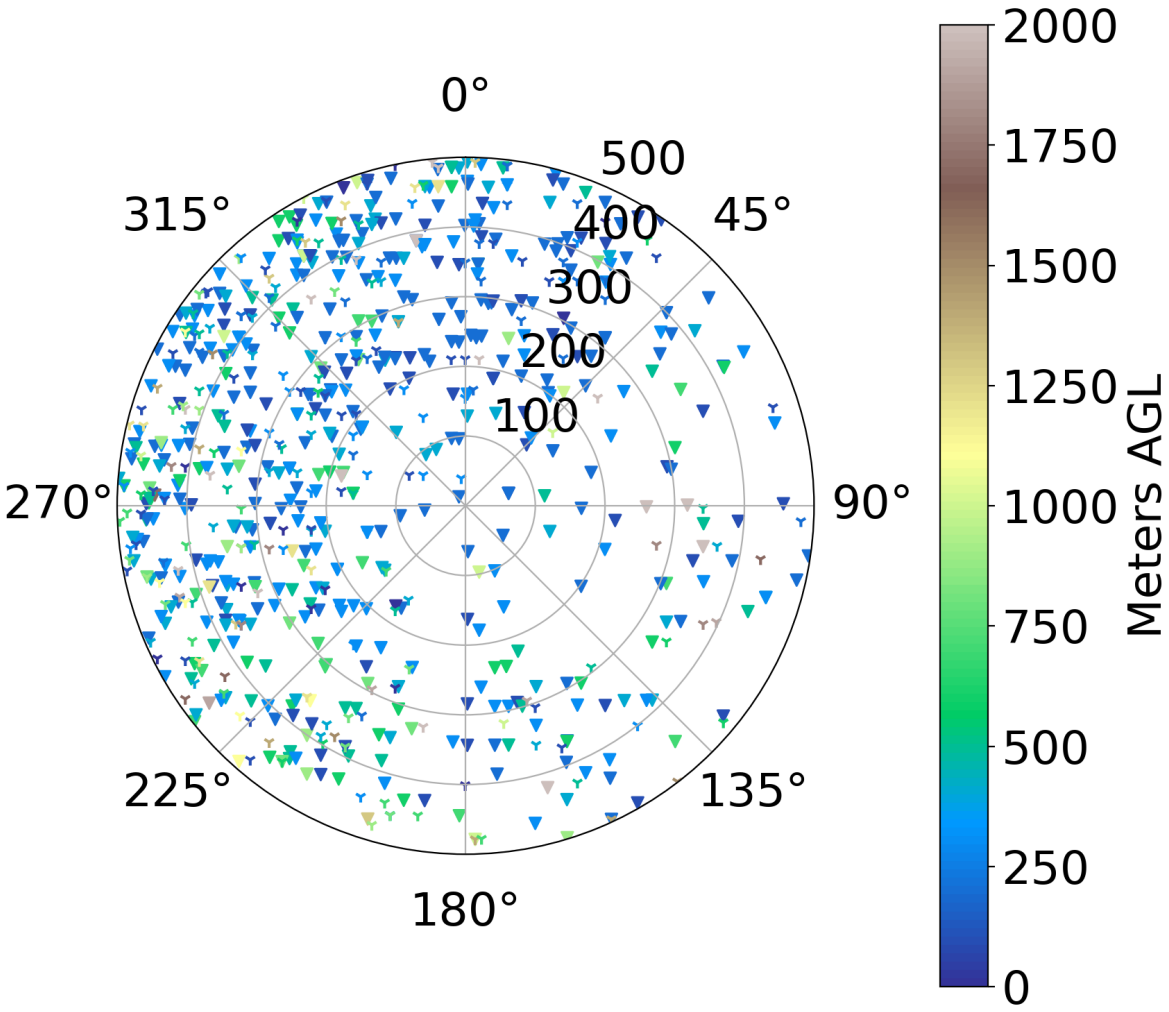

Figure 3.3: Mosaic of ASOS ceilometer cloud base heights relative to trackable low pressure centers for soundings with surface temperatures < 0 °C. Soundings with surface precipitation are marked with a filled triangle; without surface precipitation marked with a "Y". Color coding is ASOS ceilometer cloud base heights. Cloud bases are fairly uniform in all quadrants relative to the low.

Table 3.1: Characteristics for each quadrant relative to the low pressure center. Averages, medians and interquartile ranges (25th to 75th percent) are meters.

Counts	Precipitating soundings	Non-Precipitating soundings	Total
NW	350	182	532
NE	256	59	315
SE	159	99	258
SW	260	225	485
Cloud Top AGL (m)	Average (m)	Median (m)	IQR (m)
NW	6169	6400	4200
NE	7462	7400	4450
SE	5837	6250	4225
SW	4876	4800	4300
Cloud Base AGL			
NW	699	400	600
NE	1283	600	2200
SE	1618	1700	2300
SW	1262	800	1700
Depth of dBZ>0 in storm extent			
NW	514	0	300
NE	875	0	1100
SE	478	0	275
SW	200	0	0
Depth of mRi^{-1}>4 in storm extent			
NW	548	500	600
NE	563	500	600
SE	492	350	600
SW	370	200	600

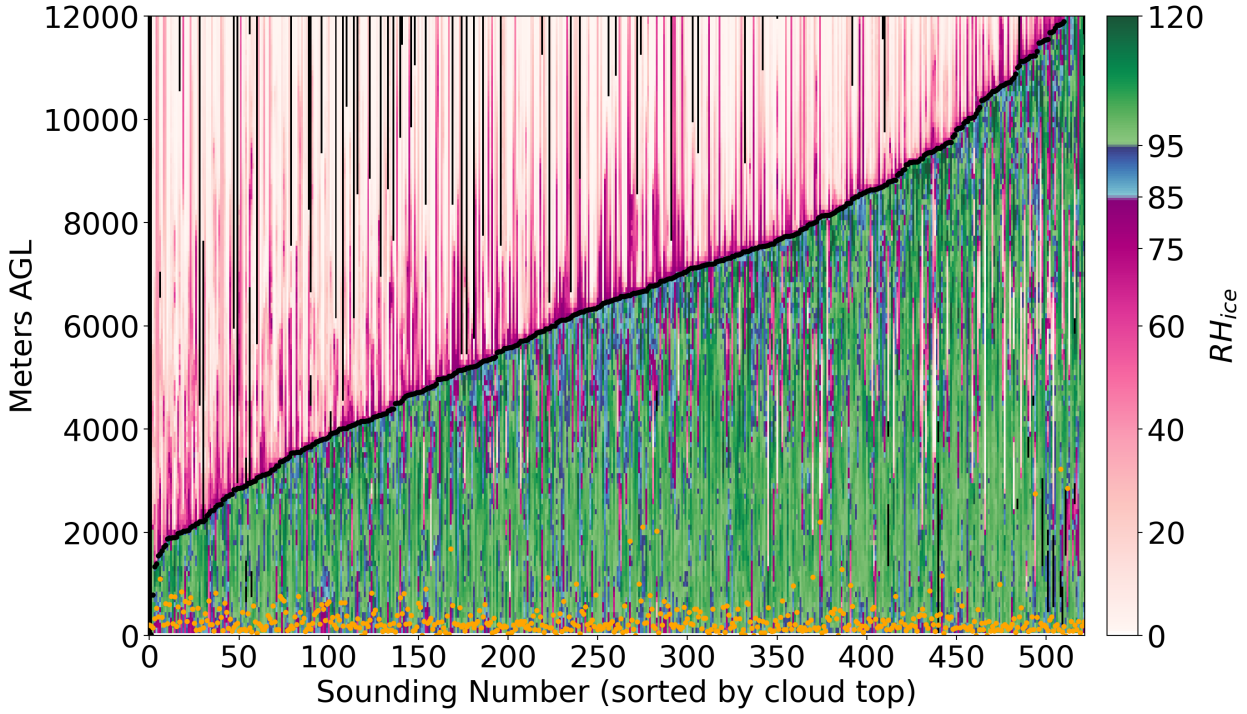

Figure 3.4: Profiles of RH_{ice} from soundings with surface temperatures < 0 °C and surface precipitation within 500 km of trackable low pressure centers. Profiles are color coded by RH_{ice} value in each 100 m layer. Each column represents one sounding. Soundings are sorted based on first the estimated cloud top (black, median value is 6.5 km) and second on the ASOS ceilometer cloud base (orange). Many profiles have areas of RH_{ice}<85% between the cloud base and top indicating likely zones of sublimation. Most of these non-cloud areas are located in the top-half of the storm's vertical extent, but there are several examples within 1 km of the cloud base as well.

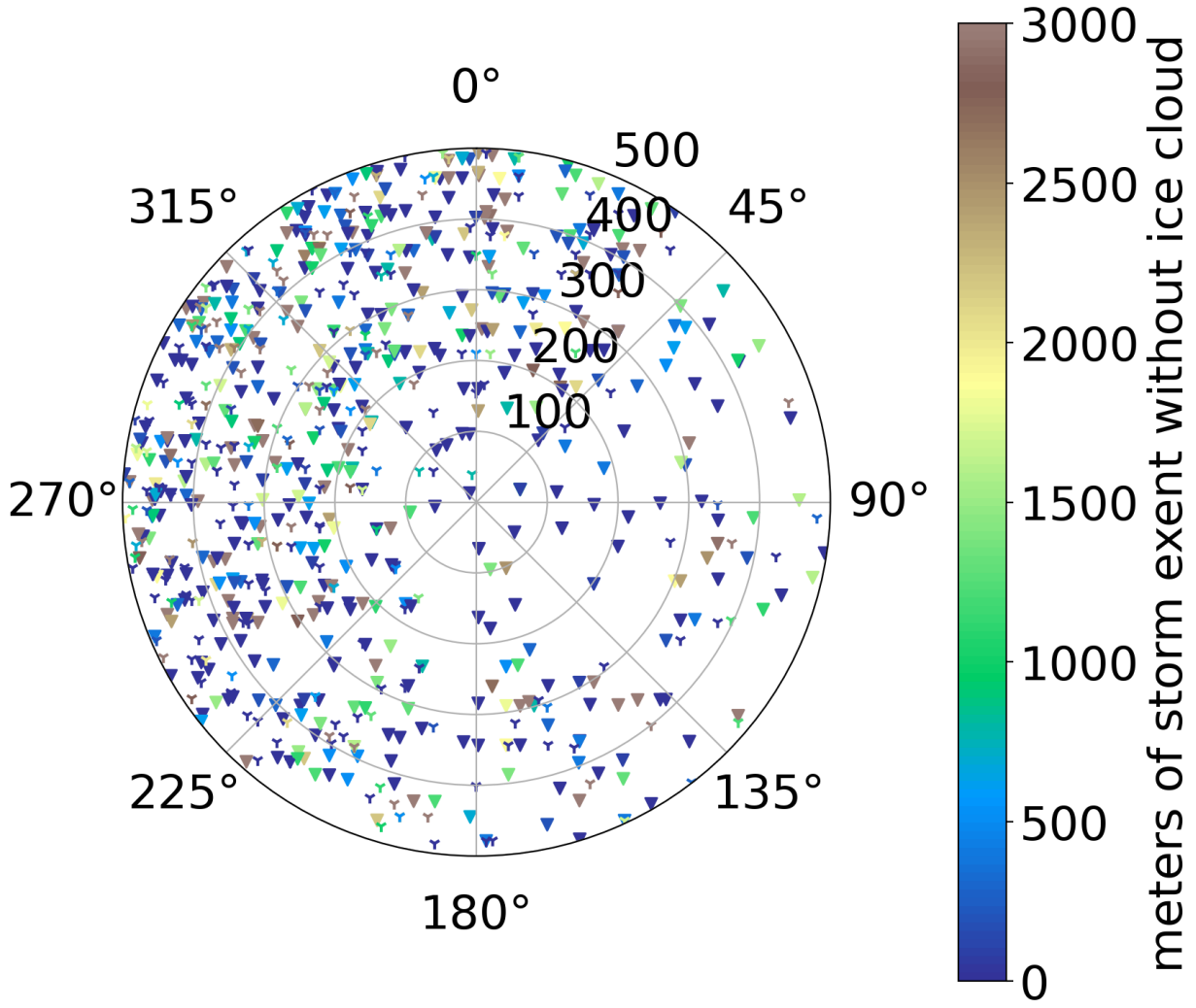

Figure 3.5: Mosaic of the depth of $RH_{ice} < 85\%$ layers within the storm vertical extent for all soundings within 500 km of trackable lows with surface temperatures < 0 °C. Soundings with surface precipitation are marked with a filled triangle; without surface precipitation marked with a "Y"

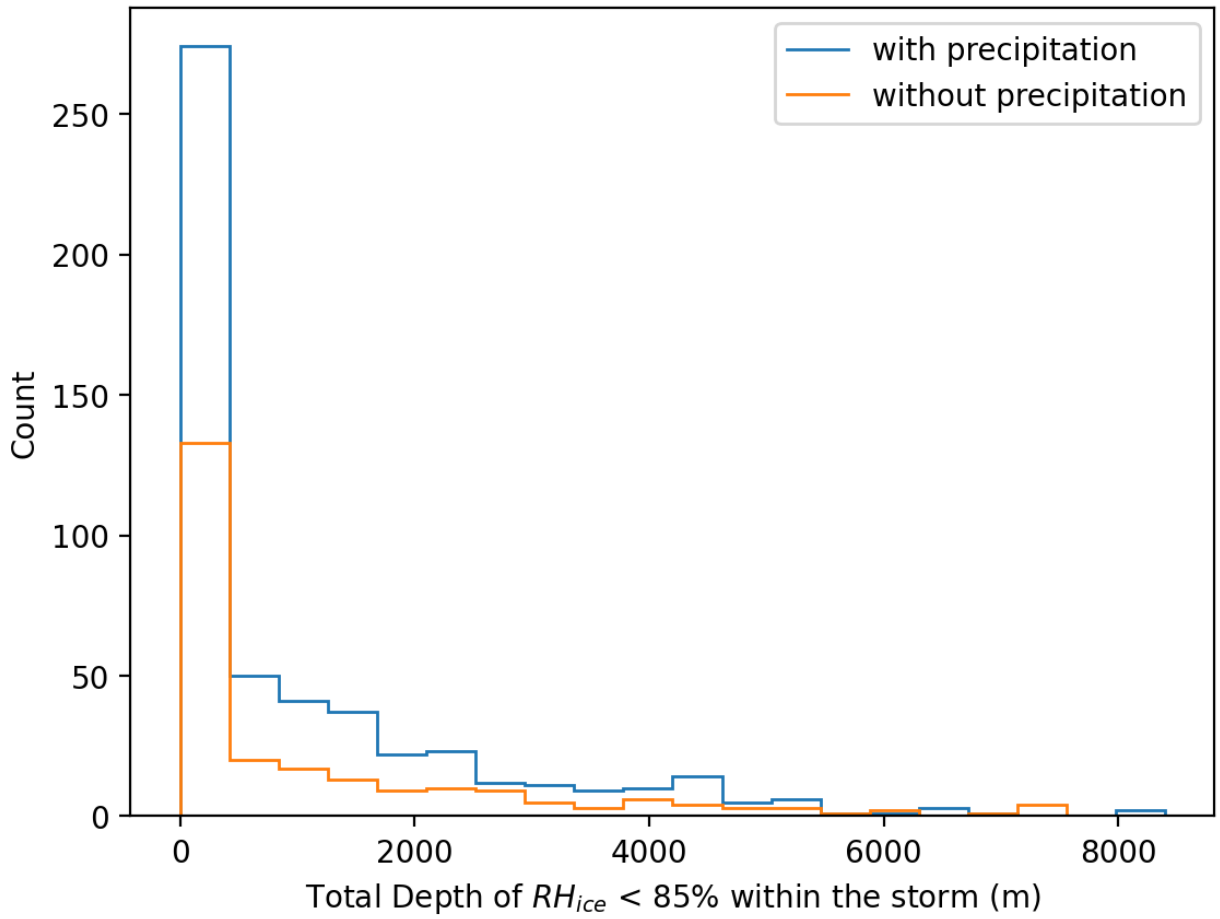

Figure 3.6: Histogram of the total depth of $RH_{ice} < 85\%$ layers within the storm vertical extent for all soundings within 500 km of trackable lows with surface temperatures < 0 °C, separated by soundings with and without surface precipitation. The long tail in both distributions show that over half of the soundings have some dry layers within the storm extent.

soundings that do have a layer subsaturated with respect to ice, the median total depth of the dry layer is 1.2 km. There is no distinct spatial pattern as to where more or less dry layer depth occurs relative to the low pressure center.

Initially, the histograms in Figure 3.6 may seem counter-intuitive; soundings without precipitation are expected to be dryer than soundings with precipitation. The reason for the observed distribution is two-fold. First, for surface temperatures below freezing, there are double the number of soundings associated with precipitation (522) compared to soundings without precipitation (243). Second, the storm vertical extent is much greater in soundings associated with precipitation (median 5,300 m) than those without precipitation (median 3,500 m). Together, this means there are far more individual 100 m layers to sample in soundings with precipitation, thus the total count of subsaturated layers is larger.

Precipitation Radar Echo

Plotting the total depth of reflectivities > 0 dBZ relative to the trackable lows was expected to produce patterns similar to the cloud top mosaic (Figure 3.2). The observed pattern (shown in Figure 3.7) shows only a slight preference for the largest depths of positive reflectivities to the north of the tracked low pressure center; depths less than 2 km are prevalent in all quadrants.

Plotting profiles of radar reflectivity provide additional context to the low pressure center relative mosaic. Soundings with surface temperature < 0 °C and precipitation are shown in Figure 3.8. The same sort order from Figure 3.4 is used. Similar to the SIR plots (Section 2.4), reflectivity values greater than 0 dBZ are color coded. When the sonde is within the radar beam but reflectivity is less than 0 dBZ, the layer is plotted gray. Layers outside of radar coverage are white (no data).

Regardless of the cloud top height, most radar echos are lower than 4 km AGL, and rarely exceed 5-6 km AGL. Thus using reflectivity measurements as a proxy for the depth of winter storms appears to be inaccurate. It is possible that low concentrations of precipitation sized ice particles at higher altitudes and longer slant ranges from the radar are not sufficient to be detected by the NEXRAD network. As expected with descending precipitation, the highest reflectivity values are located at lower altitudes.

For comparison, the reflectivity profiles for soundings with surface temperatures < 0 °C but *without* surface precipitation within 500 km of trackable low pressure centers are shown in Figure 3.9.

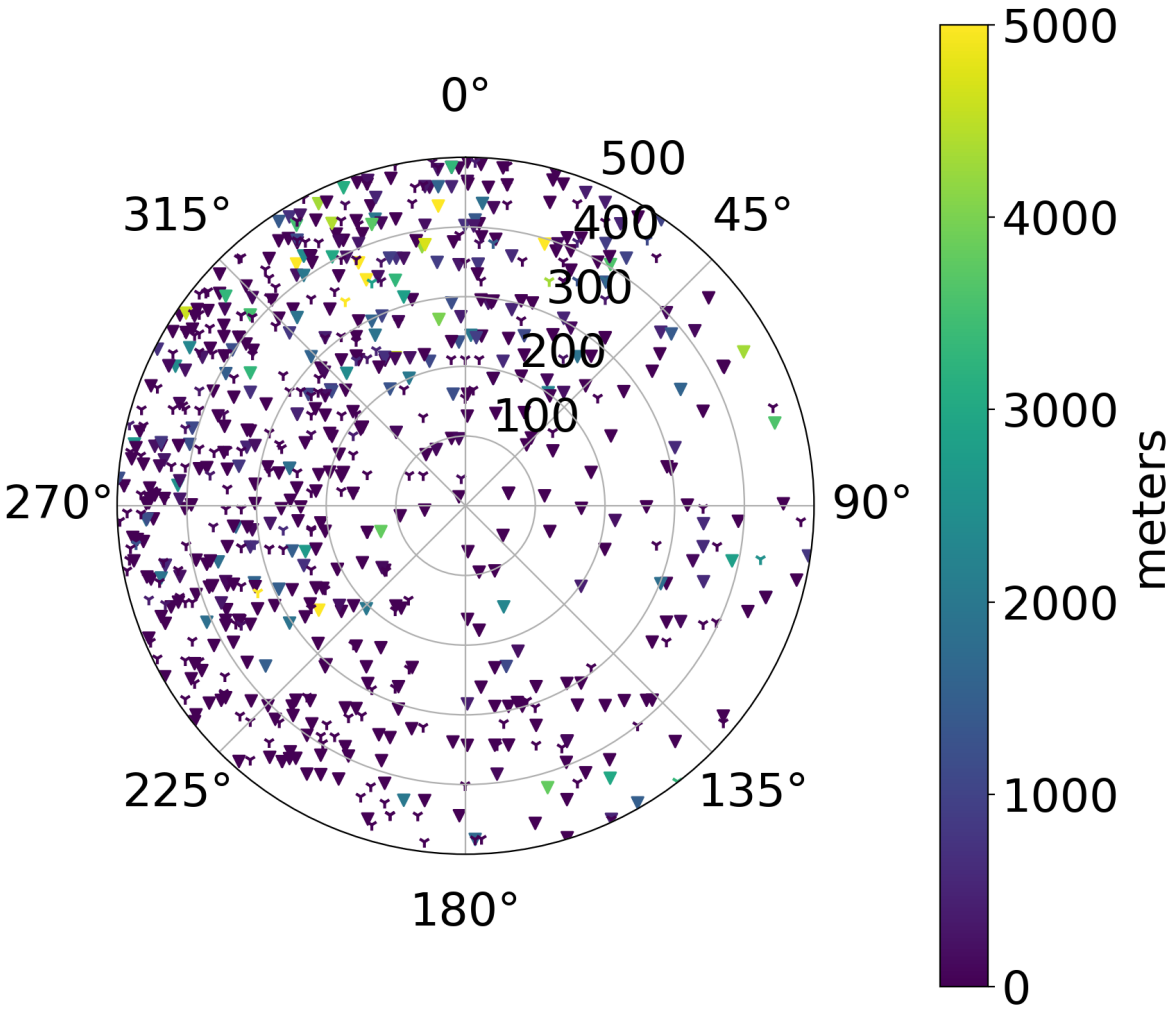

Figure 3.7: Mosaic of the total depth of radar reflectivity > 0 dBZ relative to trackable low pressure centers for soundings with surface temperatures < 0 °C. Soundings with surface precipitation are marked with a filled triangle; without surface precipitation marked with a "Y". Color coding is the total depth of radar reflectivity > 0 dBZ paired with the sounding. The vast majority of soundings have less than 2 km total depth of dBZ > 0. The largest depths of reflectivity occur to the north of the trackable lows.

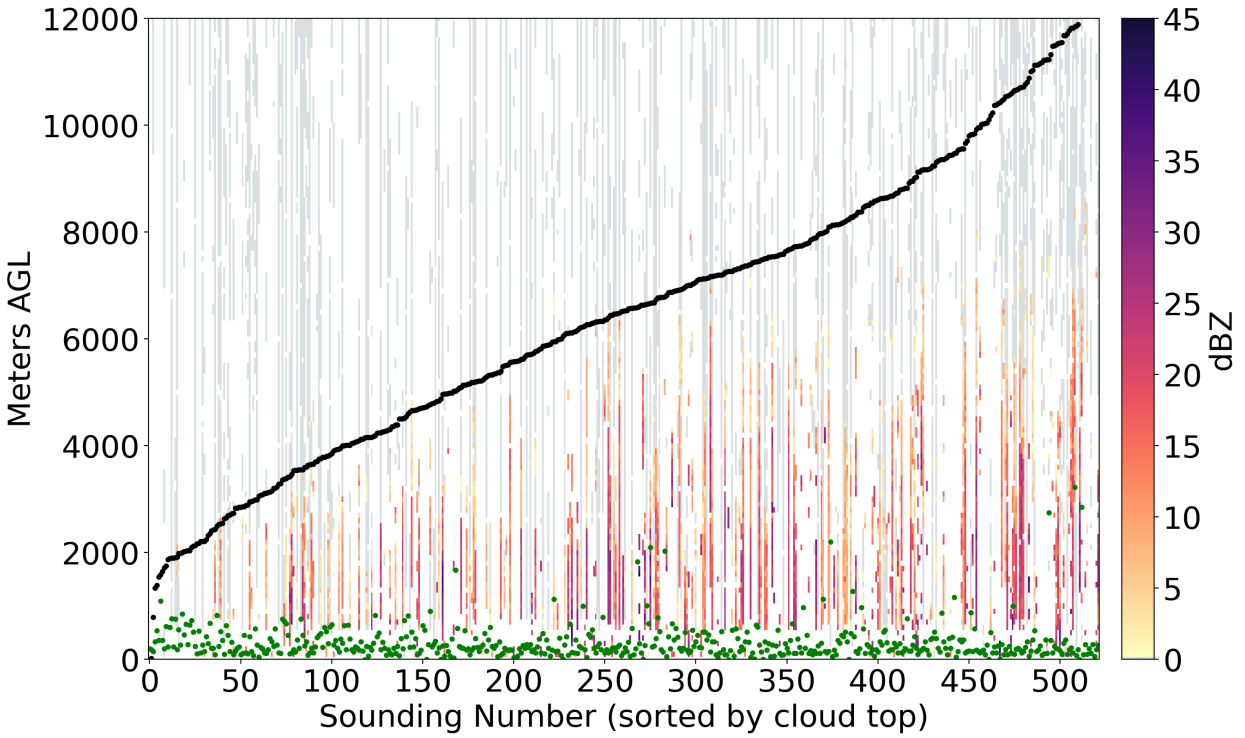

Figure 3.8: Profiles of NEXRAD reflectivity matched to sonde positions for soundings with surface temperatures < 0 °C and surface precipitation within 500 km of trackable low pressure centers. Reflectivity values greater than 0 dBZ are color coded, areas with radar coverage but dBZ <0 are gray. Layers when the sonde is outside of the radar beam are white (no data). Cloud base indicated by green dots and cloud top by black dots.

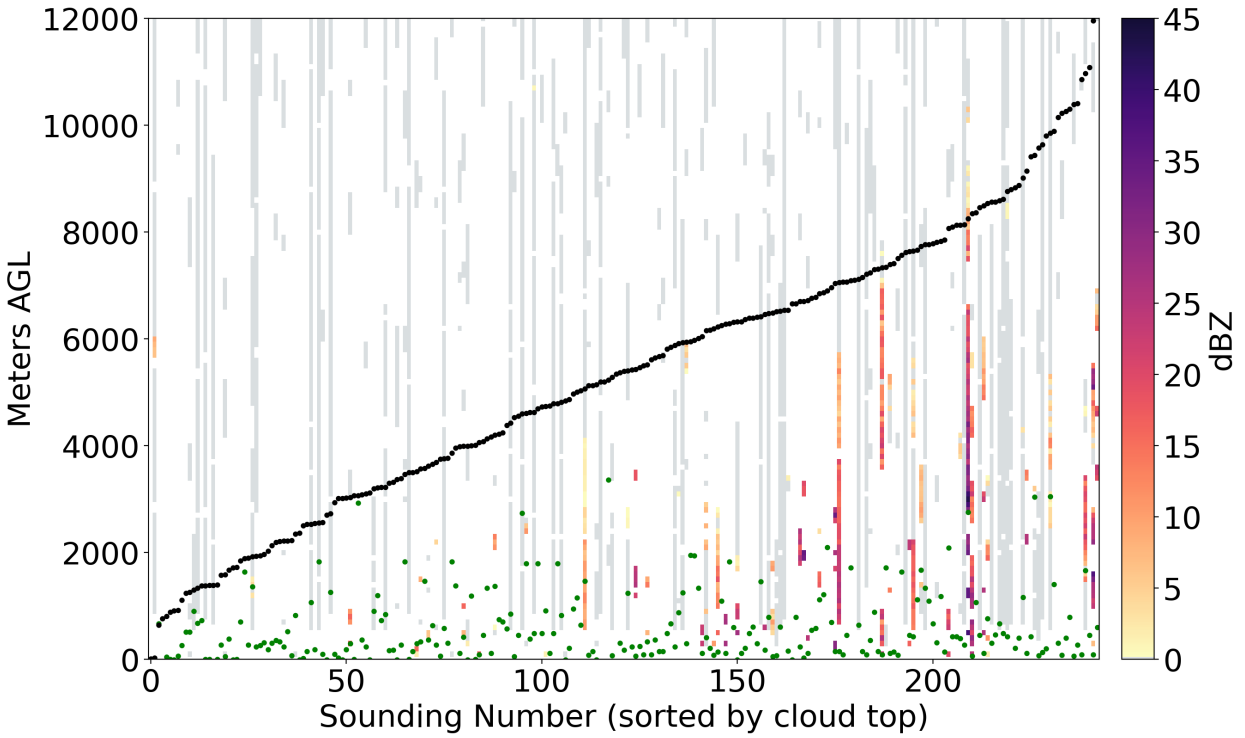

Figure 3.9: Profiles of NEXRAD reflectivity matched to sonde positions for soundings with surface temperatures < 0 °C and *without* surface precipitation within 500 km of trackable low pressure centers. Reflectivity values greater than 0 dBZ are color coded, areas with radar coverage but dBZ <0 are gray. Layers when the sonde is outside of the radar beam are white (no data). Cloud base indicated by green dots and cloud top by black dots.

Conditional Instability

For this study, lapse rates within ± 0.5 K/km of isothermal conditions will be considered as neutral. The strict definition for moist neutral conditions, $\partial \bar{\theta}_e^* / \partial z$=0, rarely occurs in the dataset, and instrumentation error is a large source of uncertainty in the potential temperature calculations. Sounding instruments can have uncertainties of 0.3 °C for temperature and 4% for relative humidity (Vaisala 2017). For typical temperatures and pressures (National Oceanic and Atmospheric Administration et al. 1976) this translates to an average θ_e^* uncertainty of 1.0 K. Therefore, small changes in the θ_e^* lapse rate are not trusted to be significant.

The number of 100 m layers with local conditional instability found 1 km above and below cloud top is shown in Figure 3.10. While neutral conditions are the most frequent near cloud top, there are more occurrences of stable lapse rates above the cloud top than below.

Profiles of θ_E^* lapse rates from soundings with surface temperatures < 0 °C and surface precipitation within 500 km of trackable low pressure centers are shown in Figure 3.11. Immediately above the surface there is often a slight unstable layer that quickly transitions to stable layer below 2 km. Above this stable layer, neutral to slightly stable conditions dominate throughout the vertical extent of the storm; conditionally unstable layers are infrequent. The neutral to stable transition at cloud top becomes sharper as cloud tops increase.

Potential Instability

Similar to conditional instability, histograms of cloud top stability and profiles of θ_E lapse rates are shown in Figures 3.12 and 3.13. Again, lapse rates within ± 0.5 K/km of isothermal conditions will be considered as neutral. Including RH measurement uncertainty in the calculation of θ_e increases the average uncertainty to 1.5 K. Overall, the pattern of potential instability is comparable to conditional instability. A slightly unstable layer immediately at the surface is capped by stable conditions below 2 km. Neutral conditions dominate above 2 km throughout the depth of the storm, switching to stable layers above cloud top.

The profiles show several potentially unstable layers near cloud tops between 3 and 4 km, but Figure 3.12 shows there are overall fewer layers of potential instability near cloud top compared to conditional instability.

To demonstrate how similar the conditional and potential stability values are, a scatter plot of the two is presented in Figure 3.14. The correlation coefficient is 0.98.

Shear Instability

Vertical shear instability (as measured by the inverse moist Richardson number, mRi^{-1}) near cloud top is shown in Figure 3.15 and via profiles in Figure 3.17 for soundings with surface

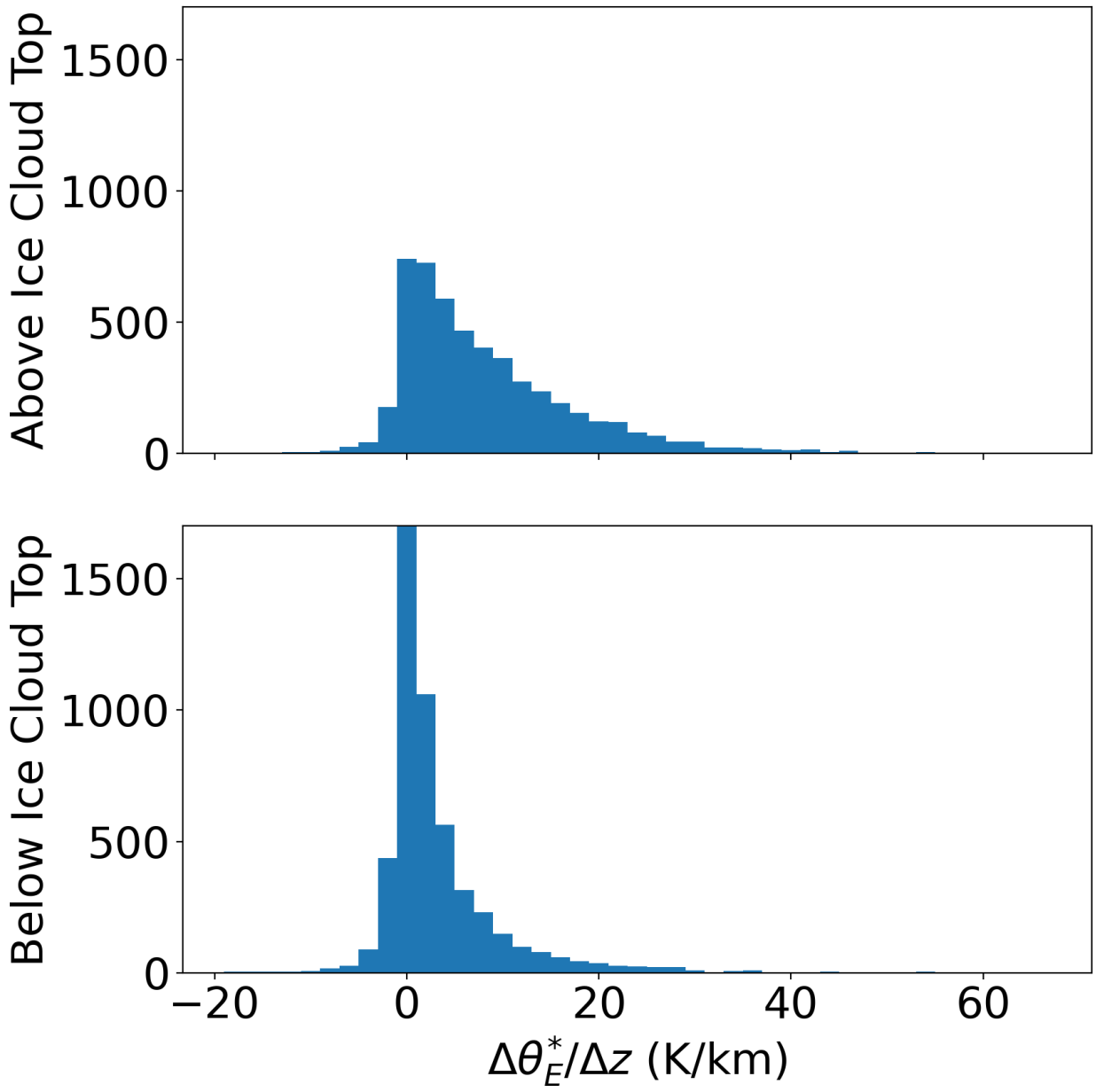

Figure 3.10: Histograms of θ_E^* lapse rates 1 km above and 1 km below cloud top from soundings with surface temperatures < 0 °C and precipitation within 500 km of trackable low pressure centers. Values <0 K/km are conditionally unstable. The longer tail of stable lapse rates above the cloud top indicates increased stability above the storm vertical extent.

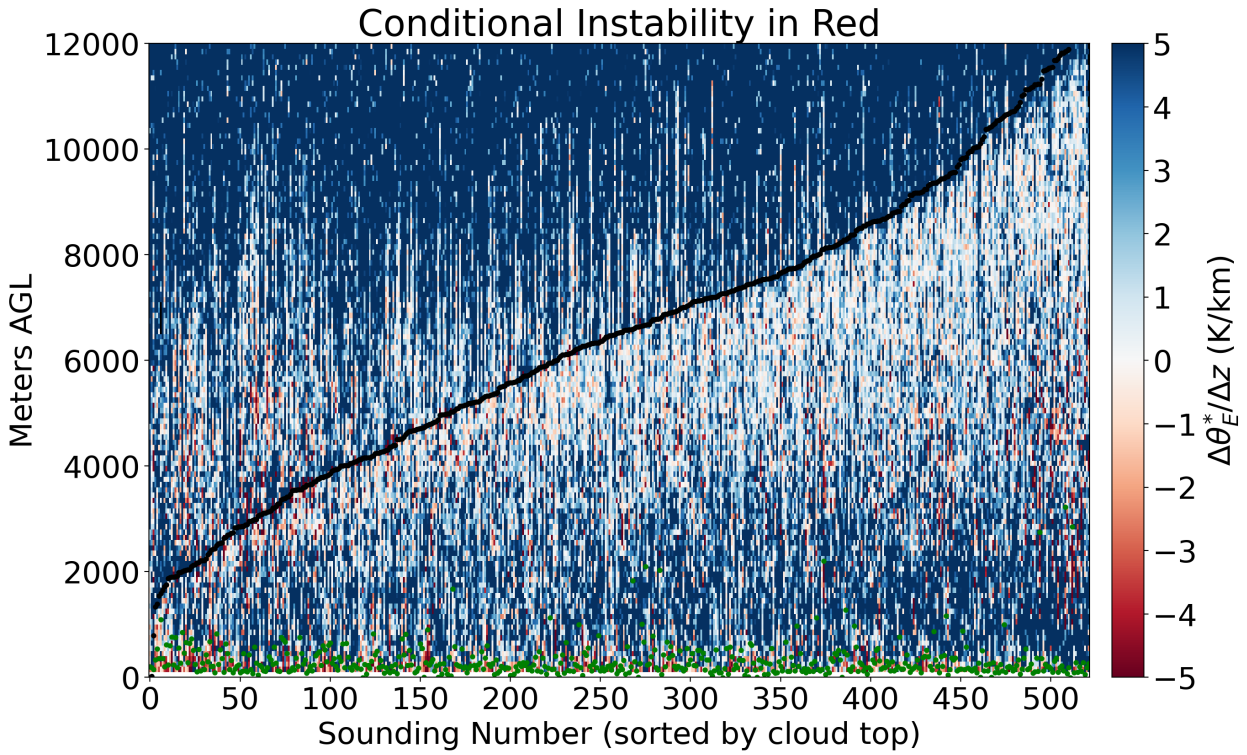

Figure 3.11: Profiles of θ_E^* lapse rates for soundings with surface temperatures < 0 °C and surface precipitation within 500 km of trackable low pressure centers. Values less (greater) than 0 K/km are conditionally unstable (stable) and are shaded red (blue). Cloud base indicated by green dots and cloud top by black dots.

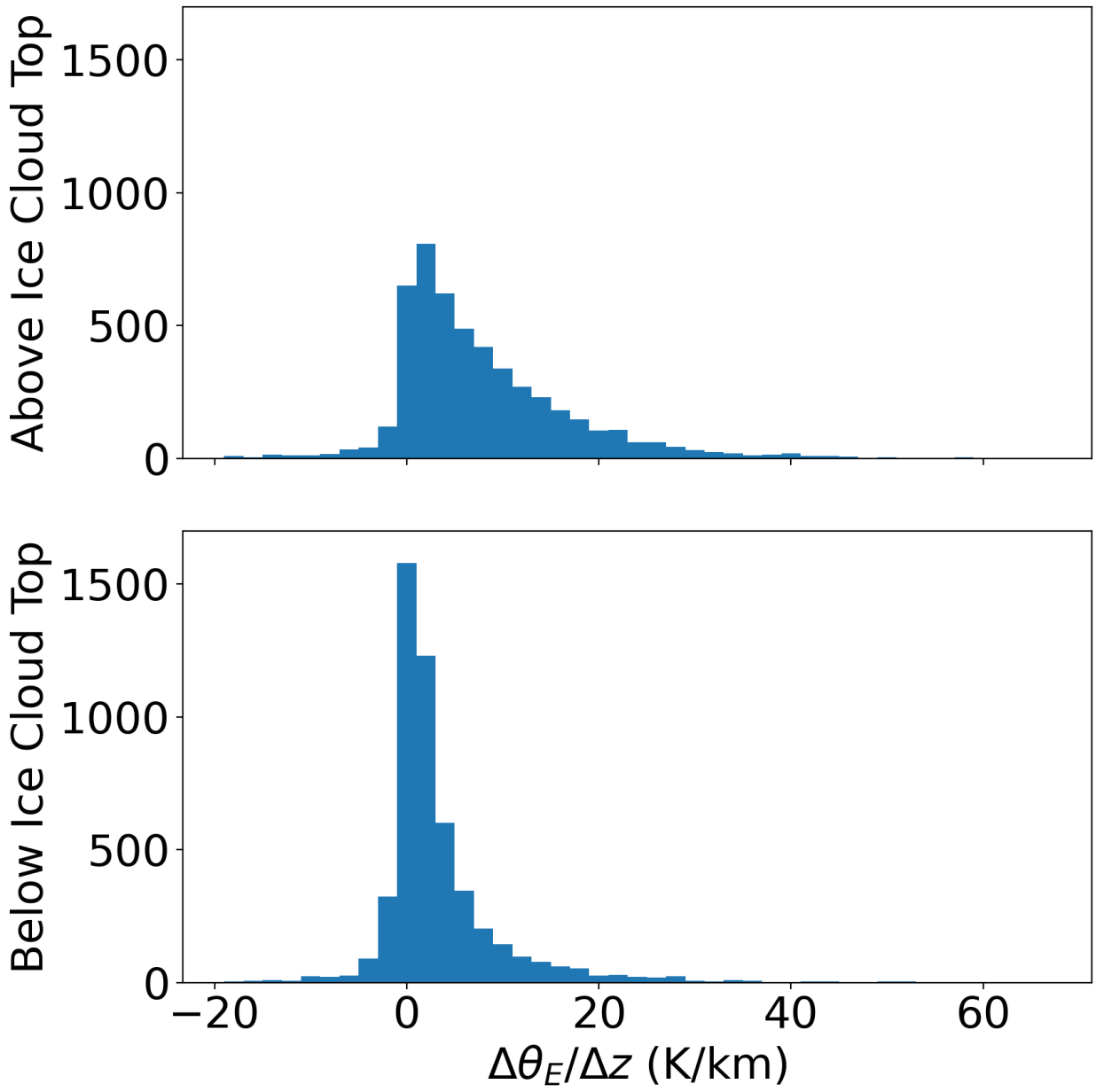

Figure 3.12: Histograms of θ_E lapse rates 1 km above and 1 km below cloud top from soundings with surface temperatures < 0 °C and precipitation within 500 km of trackable low pressure centers. Values <0 K/km are potentially unstable. The longer tail of stable lapse rates above the cloud top indicates increased stability above the storm vertical extent.

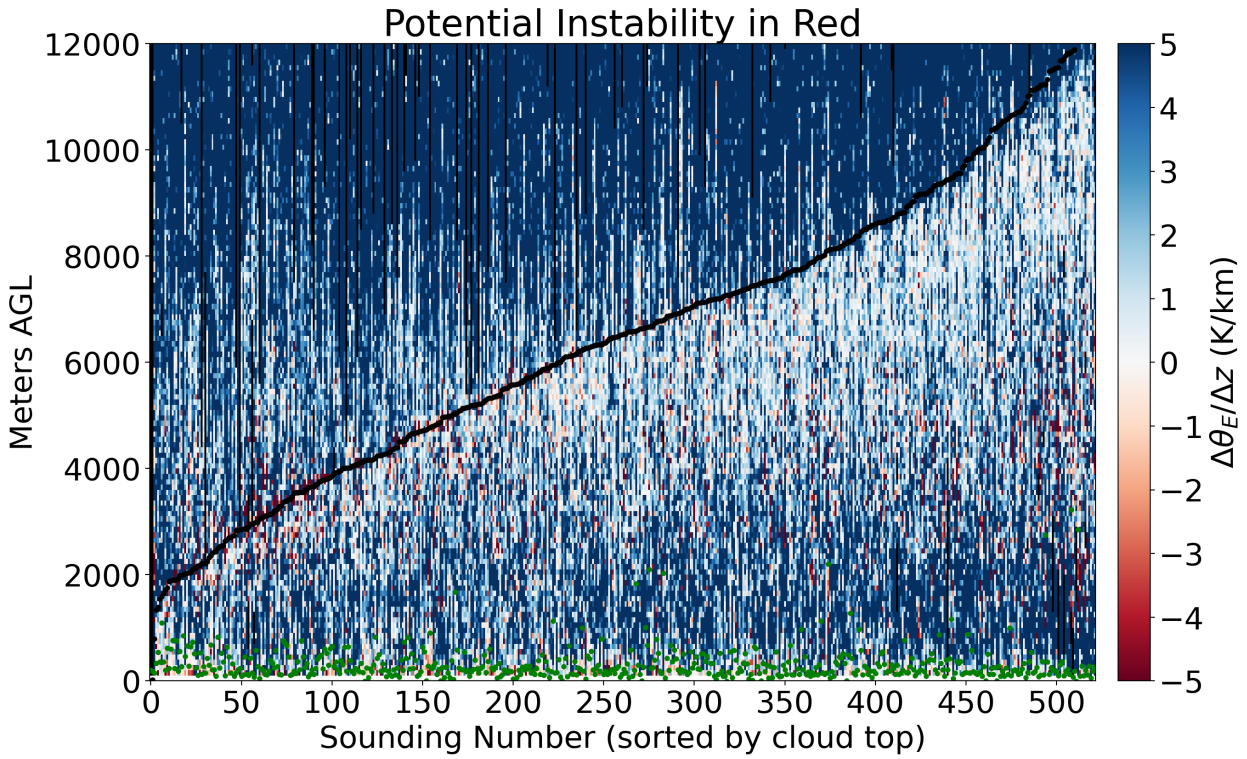

Figure 3.13: Profiles of θ_E lapse rates for soundings with surface temperatures < 0 °C and surface precipitation within 500 km of trackable low pressure centers. Values less (greater) than 0 K/km are potentially unstable (stable) and are shaded red (blue). Cloud base indicated by green dots and cloud top by black dots.

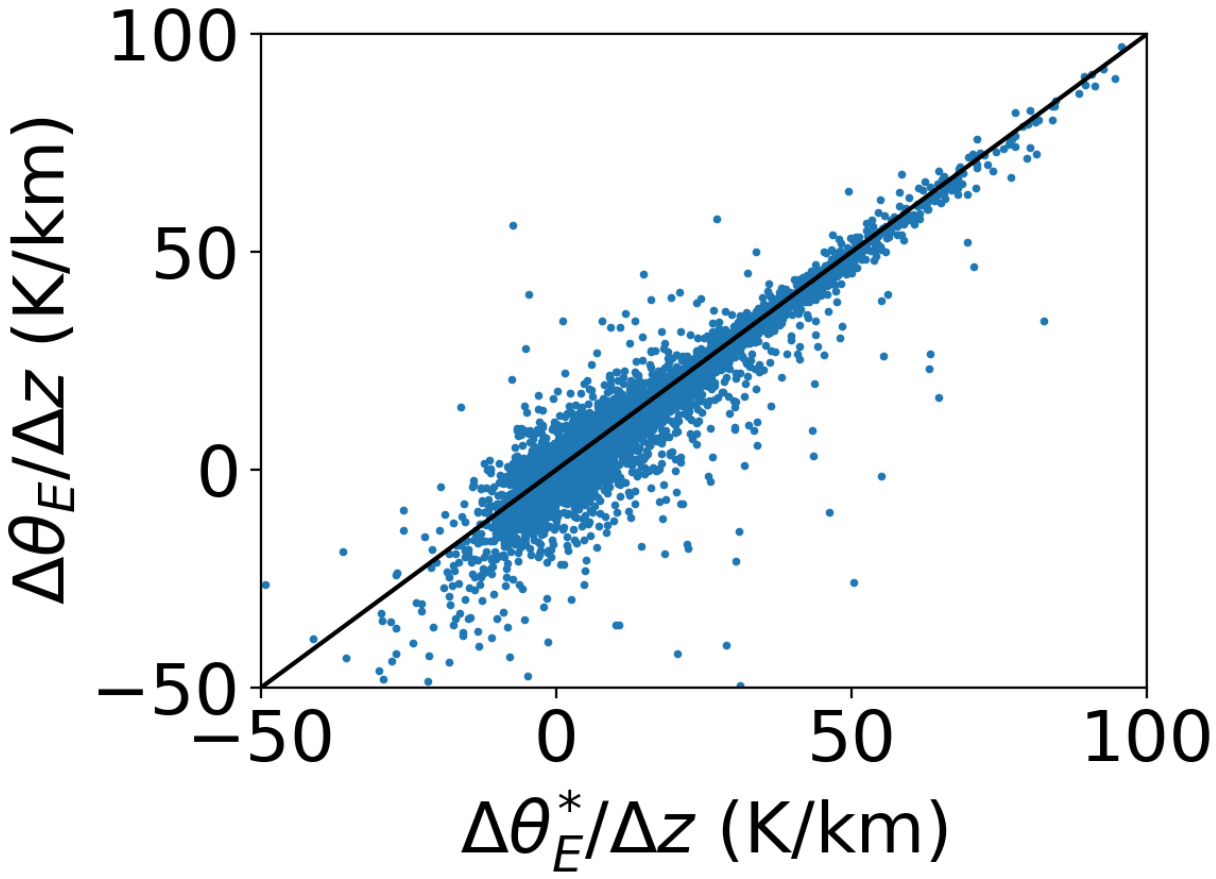

Figure 3.14: Scatterplot of conditional stability lapse rate compared to potential stability lapse rates for soundings with surface temperatures < 0 °C and precipitation within 500 km of low pressure centers.

temperatures < 0 °C and surface precipitation within 500 km of trackable low pressure centers. As with conditional and potential instability, there is less vertical shear instability above the cloud top.

The vertical profiles of mRi^{-1} are very noisy and have many layers where the moist Brunt-Väisälä frequency is undefined, adding missing data to the noise. Thus, the components of the mRi are plotted separately in Figures 3.19 and 3.20.

The profiles of mBV are similar to those of conditional and potential stability. A larger mBV frequency indicates that an air parcel displaced in statically stable air would experience a larger restoring buoyant force (more stable). The mBV profiles show that below 2 km AGL there is increased stability. For the rest of the storm extent conditions are close to neutral. The mBV profiles also indicate increased stability above cloud top.

The wind shear component of the mRi shows a different signal contributing to vertical shear instability. Shear is computed here by the vector difference between the 2D winds at the top and bottom of each 100 m layer. Larger values of wind shear provide more kinetic energy to overturn parcels, leading to instability. Below 2 km there are relatively large values of the shear component; this is expected from friction in the boundary layer. (Also recall that Fovell and Gallagher (2020) noted that winds below 250 m should not be trusted.) There is also a layer of increased wind at the cloud top boundary. In general, the shear increases with cloud top. This increased kinetic energy combined with near neutral conditions immediately below cloud top suggests that overturning and cloud top entrainment is present in most storms.

3.2 Summary

For storms associated with wintery precipitation, about 11% of storm depth is subsaturated with respect to ice (< 85% RH_{ice}). Most of these dry layers are in the upper portion of the cloud. Very few layers subsaturated with respect to ice are colocated with weather radar echo > 0 dBZ. Weather radar echoes greater than 0 dBZ, indicative of precipitation-sized ice, occur primarily below 4 km and rarely exceed 6 km AGL in these storms, regardless of the storm depth. Hence, dry air entrainment will reduce cloud-ice mass more commonly than precipitation-ice mass.

As expected from conceptual models, the layer above 1 km cloud top is more locally stable for conditional, potential, and shear instabilities than the layer 1 km below cloud top. Observing this expected pattern gives confidence that the cloud top estimate used is reasonable. Enhanced wind shear is common within a few 100 m of cloud top which suggests cloud top entrainment of dry air is nearly always occurring (Figs. 3.20 and 3.21). Inside the storm depth, the vast majority of layers have local neutral stability. The moist Richardson number values indicating possible presence of Kelvin-Helmholtz waves occur about 15% of the time at each level throughout

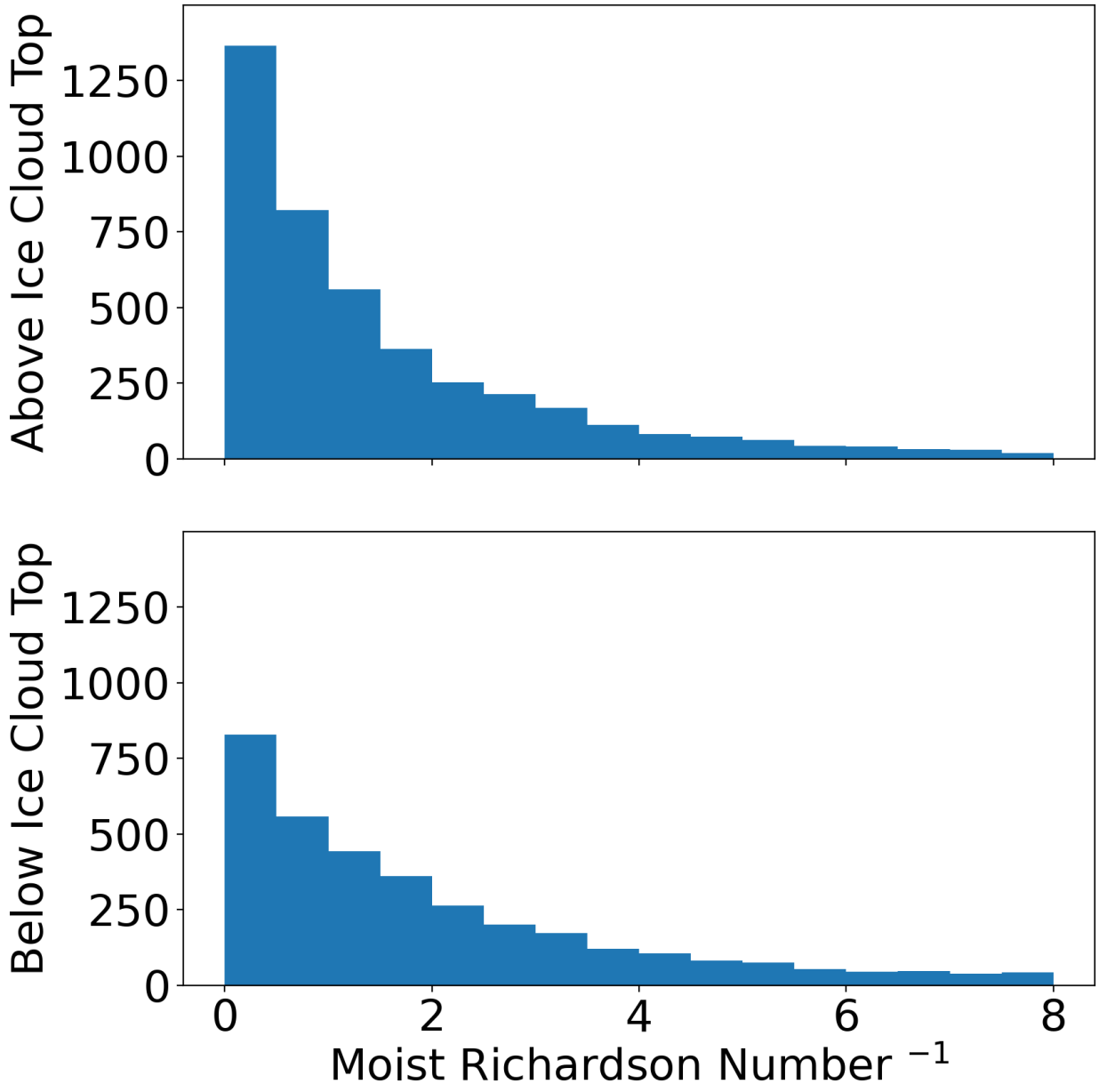

Figure 3.15: Histograms of mRi^{-1} 1 km above and 1 km below cloud top from soundings with surface temperatures < 0 °C and precipitation within 500 km of trackable low pressure centers. Values greater than 4 have vertical shear instability.

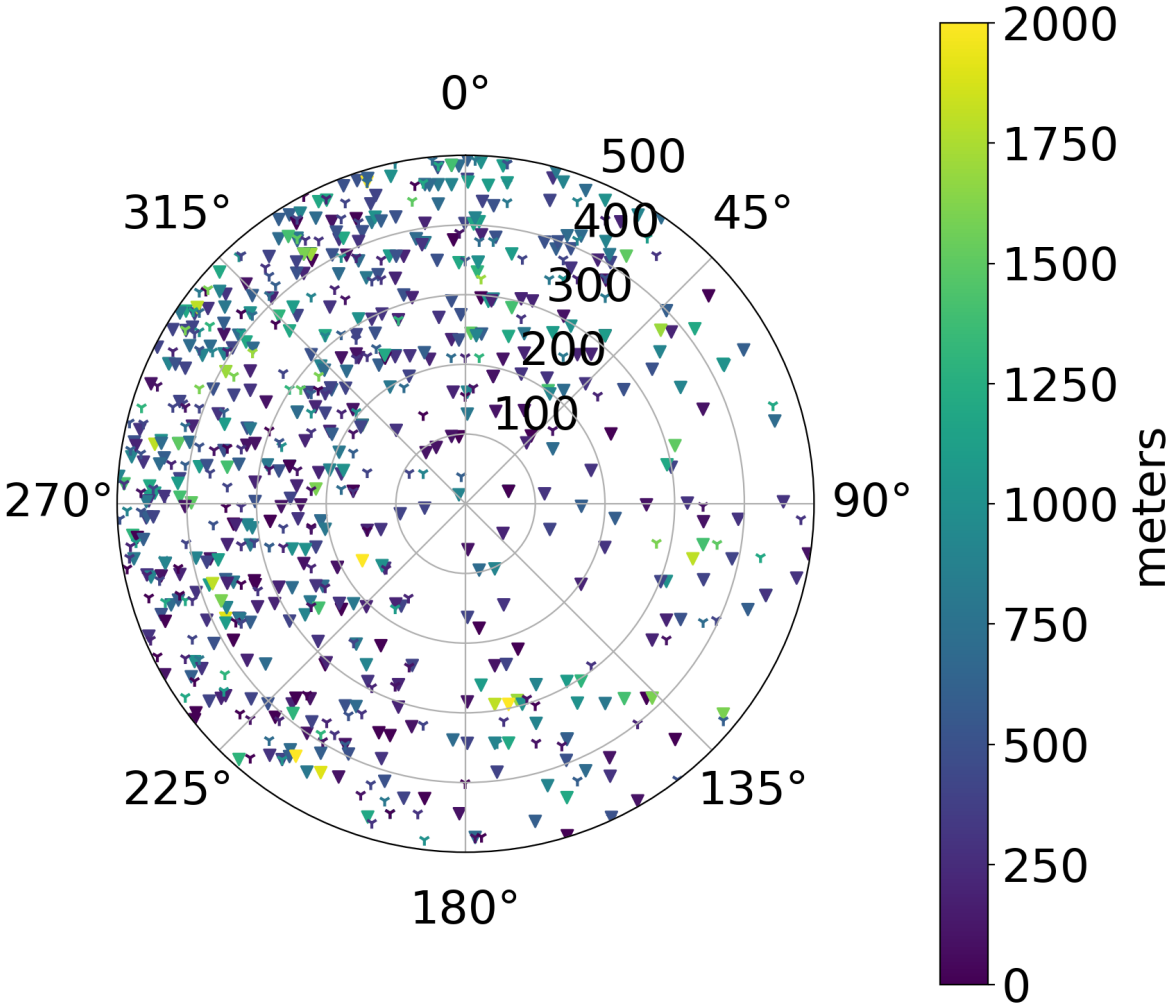

Figure 3.16: Mosaic of the total depth of $mRi^{-1} > 4$ relative to trackable low pressure centers for soundings with surface temperatures < 0 °C. Soundings with surface precipitation are marked with a filled triangle; without surface precipitation marked with a "Y". Color coding is the total depth of $mRi^{-1} > 4$.

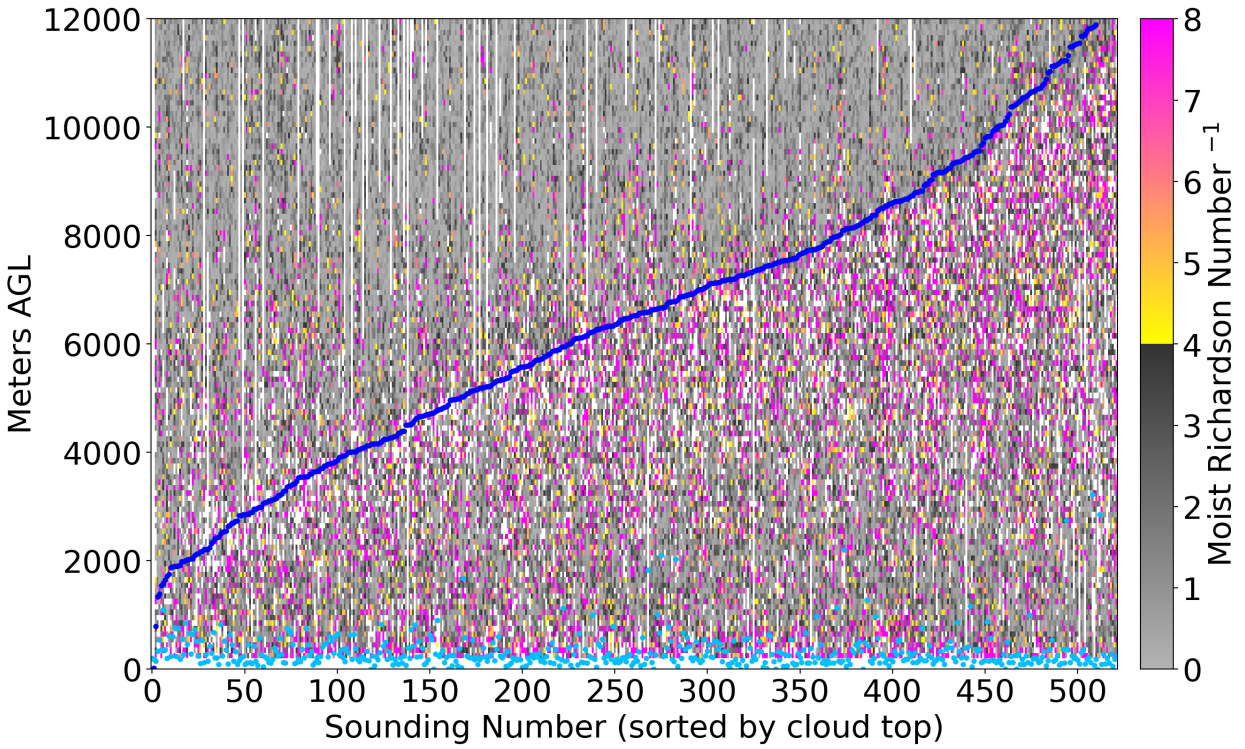

Figure 3.17: Profiles of mRi^{-1} for soundings with surface temperatures < 0 °C and surface precipitation within 500 km of trackable low pressure centers. Values greater than 4 have vertical shear instability and are color coded. Stable values are shown in gray. Cloud base indicated by light blue dots and cloud top by dark blue dots.

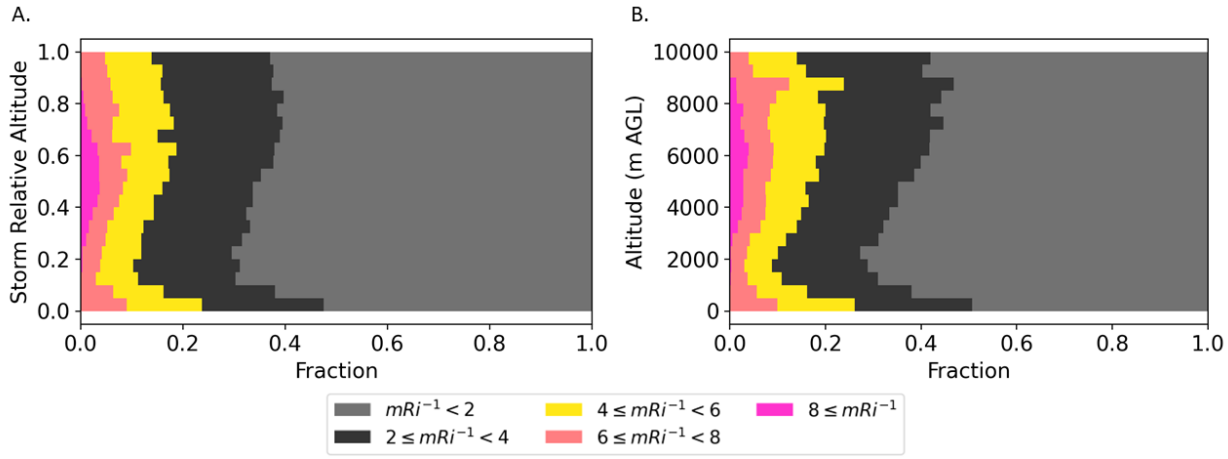

Figure 3.18: Stacked histogram of mRi^{-1} measurements within the storm vertical extent for soundings with surface temperatures < 0 °C and precipitation within 500 km of trackable low pressure centers. Panel A. is binned by storm relative altitudes. Panel B. is binned by altitude AGL. Each histrogram is normalized by the number of observations at each altitude.

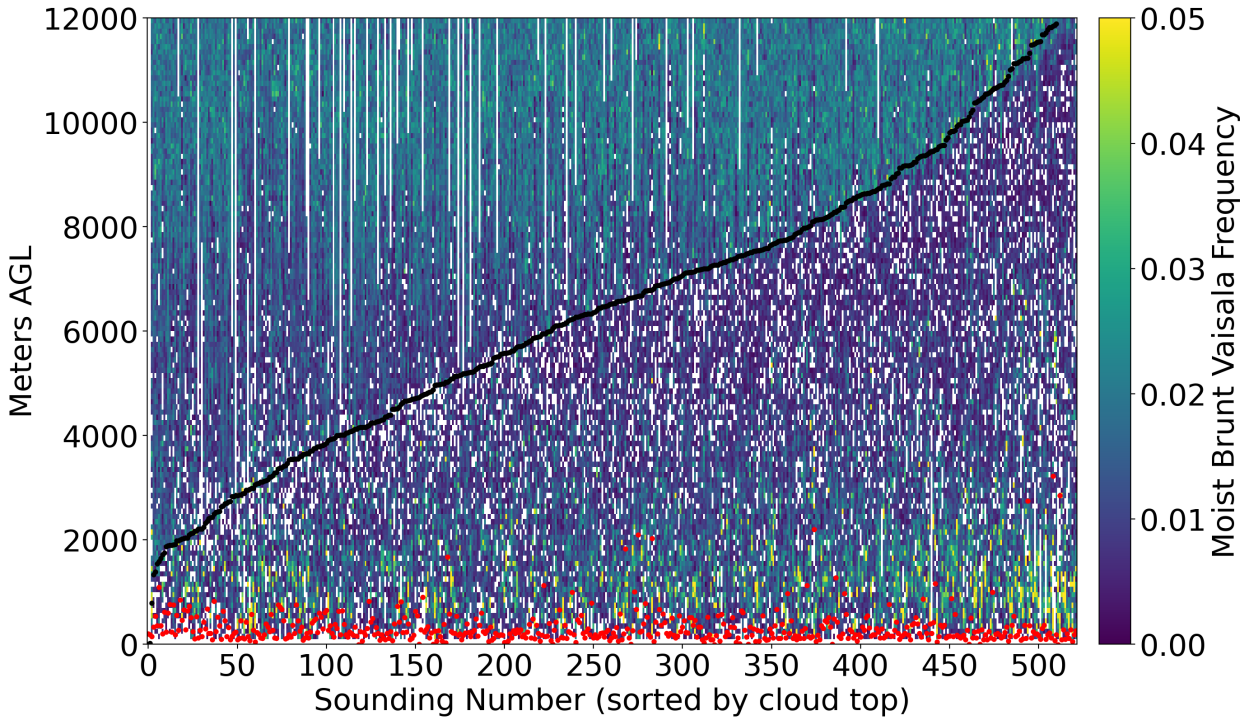

Figure 3.19: Profiles of the moist Brunt-Väisälä frequency for soundings with surface temperatures < 0 °C and surface precipitation within 500 km of trackable low pressure centers. Larger values are more stable. Cloud base indicated by red dots and cloud top indicated by black dots.

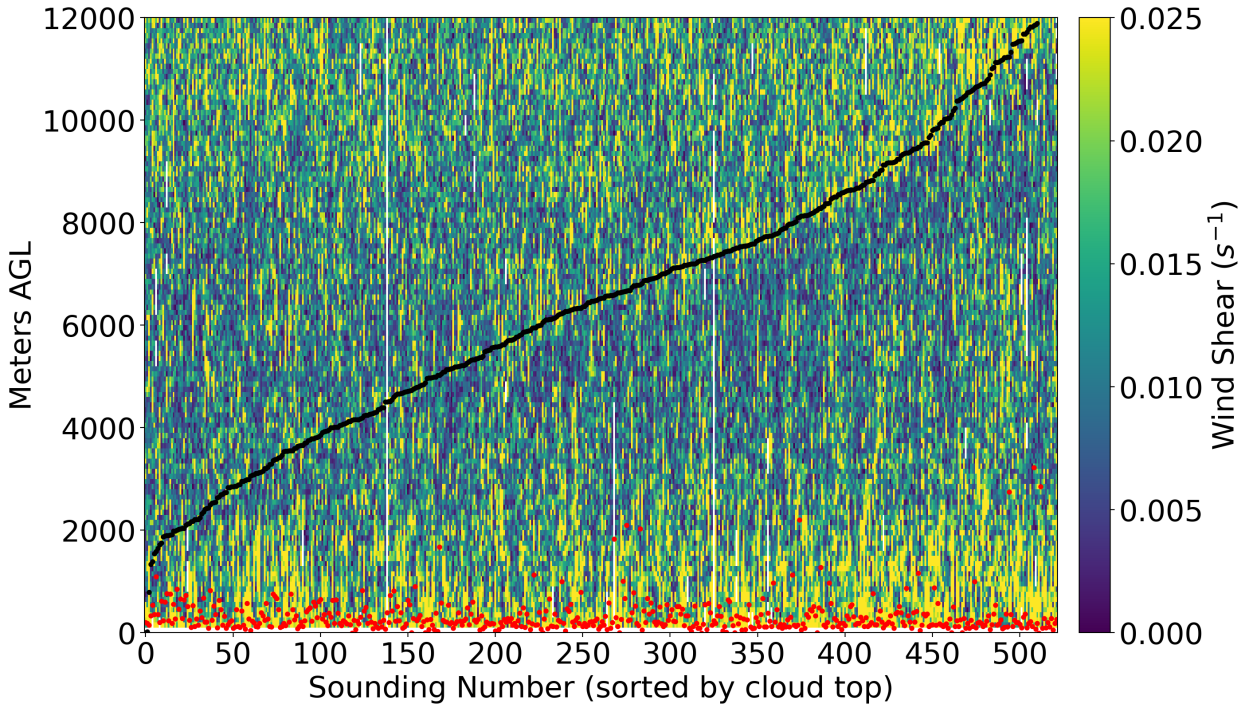

Figure 3.20: Profiles of $\frac{\partial \bar{u}}{\partial z}$ for soundings with surface temperatures < 0 °C and surface precipitation within 500 km of trackable low pressure centers. Cloud base indicated by red dots and cloud top by black dots.

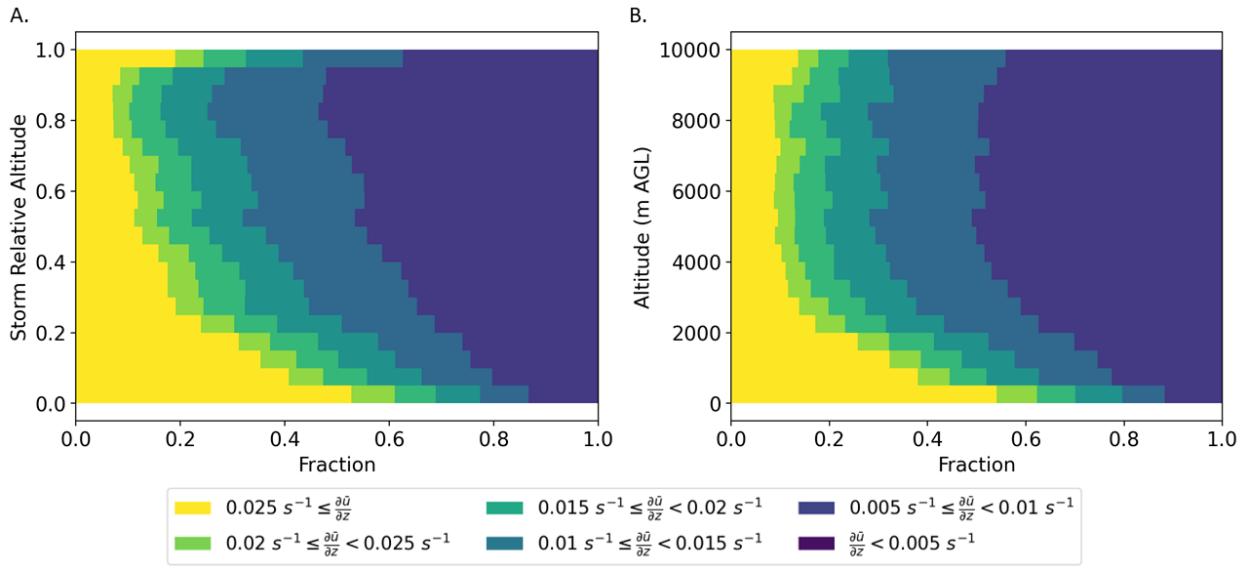

Figure 3.21: Stacked histograms of $\frac{\partial \bar{u}}{\partial z}$ for soundings with surface temperatures < 0 °C and surface precipitation within 500 km of trackable low pressure centers. Panel A. is binned by storm relative altitudes. Panel B. is binned by altitude AGL. Each histrogram is normalized by the number of observations at each altitude.

the vertical extent of the cloud (Figure 3.18). Compared to higher altitudes, the lowest 2 km of the profiles have larger magnitudes of wind shear and more layers with local conditional and potential stability. These competing factors imply that turbulent motions in the boundary layer are frequent, but resultant vertical motions are damped (Figs. 3.20 and 3.21).

For all 1,590 soundings relative to low pressure centers, cloud tops in the NE and NW quadrant have median values 1.5 km higher than the SW quadrant (Table 3.1). This is consistent with expectations from conceptual models where large scale ascent is present (Figs. 1.1). In contrast to conceptual models, which indicate that horizontal advection of dry air intrudes preferentially in the NW quadrant of the cyclone, all four quadrants have similar average total vertical depths of dry layers between the cloud top and cloud base (Table 4.1). There are no obvious gradients in cloud base height with distance from the low pressure center (Fig. 3.3). Median cloud base heights are 400, 600, and 800 m for NW, NE and SW quadrants respectively (Table 3.1). Notably, the NW quadrant has a much smaller interquartile range as compared to NE and SW quadrants. Considering only soundings associated with precipitation, the median cloud base is 200 or 300 m in all quadrants. This is most likely due to precipitation providing ample moisture to the low levels, causing cloud bases to drop to a similar level.

CHAPTER

4

RESULTS - HYPOTHESIS TESTING AND SYNTHESIS

Data from IMPACTS shows that sublimating layers exist within storms, demonstrated in Figure 1.13 by ice-subsaturated regions inside the storm volume alongside ice particles with observed sublimation. Many storms examined by IMPACTS in January-February 2020 had well over half of the observed ice particles in environments well below ice-saturation (Peele et al. 2021). Figure 4.1 shows evidence of potentially sublimating layers from another data source, the Ka-band scanning polarimetric radar (KASPR) at Stony Brook University (Oue et al. 2017). Areas I, II, and III in Figure 4.1 show that there are regions in the storm volume that are nearly devoid of cloud, indicated by low reflectivity. At a later time during the same storm, Area IV has a similar signature of low reflectivity sandwiched in the vertical extent of the storm. At the same altitude as IV, Area V has enhanced reflectivity features, known as fall streaks or ice streamers, that originate from generating cells immediately above Area V. Reflectivity alone cannot differentiate between precipitation ice falling through a cloud layer and precipitation ice falling through a subsaturated, cloud-free layer. Comparing against Area IV, Area V hints at a possible layer of sublimating ice particles, but this cannot be determined without in-situ moisture measurements. Storms that were studied by IMPACTS also had many generating cells produced by cloud top instabiltities (not shown).

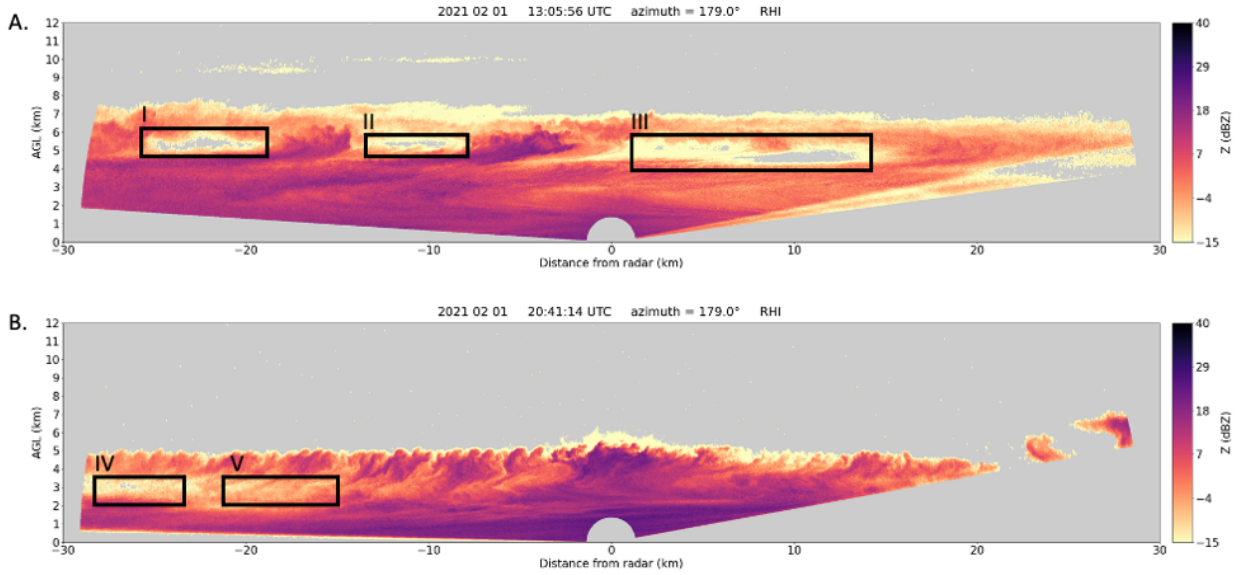

Figure 4.1: Selected Range Height Indicator scans from Ka-band scanning polarimetric radar (KASPR) at Stony Brook University (Oue et al. 2017) on 1 Feb 2021. Areas I, II, and III indicate nearly cloud-free regions within the vertical extent of this storm. Areas IV and V also have low reflectivities between higher relectivities above and below them. Immediately above Area V, generating cells are observed with contiguous areas of enhanced reflectivies extending into Area V.

These features, detected by sensitive research equipment, motivated the hypotheses constructed at the start of this study. We focused on research questions related to 1) the frequency and vertical positioning of sublimating layers (i.e. dry layers with $RH_{ice} < 85\%$ and precipitation-sized ice as determined from radar echo > 0 dBZ) and 2) the frequency of different kinds of instabilities near cloud top.

After compiling the full dataset as described in Chapter 2, it became evident that the conditions specified in the hypotheses were not often observed. Many of the testable hypotheses were rejected and several could not be evaluated because the relevant sample size was too small. In the following subsections, hypotheses for each research question are addressed in turn.

4.1 Prevalence of sublimating layers

Initial investigations into the sounding profiles and aircraft data from NASA IMPACTS suggested that significant portions of winter storm volume with precipitation-sized particles were subsaturated with respect to ice. Subsequently, there have been concerns regarding the NASA

aircraft dewpoint sensors (see Section 2.5). The first portion of this study was to quantify sublimating layers detected by this dataset.

Underlying question: How much of a winter storm's vertical extent is not saturated with respect to ice? Are layers with radar echoes (and thus precipitation-sized particles) but without ice cloud prevalent enough and distributed in such a manner that they should not be ignored in conceptualizations of winter storms?

The first two hypotheses address the extent and location of sublimating layers.

Testable Hypothesis 1a: Radar echo layers without ice cloud comprise more than 20% of the vertical depth of valid radar measurements within the vertical extent of winter storms.

Testable Hypothesis 1b: More than 60% of observed radar echo layers without ice cloud occur in the top half of a storm's vertical extent (between cloud base and top).

Numerical thresholds for the hypotheses were assigned *a priori*. For 1a., assuming an average storm vertical extent of 5 km, 20% of the storm depth would correspond to 1 km. This would be sufficient to sublimate nearly all the ice particles descending through the layer as modeled by Clough and Franks (1991). For 1b., the sublimating areas were anticipated to be at higher elevations in storms due to increased moisture availability at low levels. The threshold of 60% was selected to demonstrate a preference for the higher altitudes.

Both 1a. and 1b. are based on the total amount of valid radar measurements within the storm's extent. Areas of sublimating precipitation cannot be inferred without radar reflectivity to measure precipitation-sized particles. The fairly uniform distribution of radar measurement altitudes within the storm extent (Figures 2.5B and 2.6) was expected to provide a sufficient sample.

Figure 4.2 shows the distributions of RH_{ice} measurements as stacked histograms within vertical extent of storms where the corresponding ASOS recorded surface temperatures < 0 °C and precipitation within 500 km of trackable low pressure centers. Panel A shows the distribution by storm relative altitude. Using the 85% RH_{ice} threshold, 11% of the sampled storm volume does not have ice clouds present; 71% of these dry layers occur in the top half of the storm vertical extent.

The same subset of data is presented in meters AGL in Panels B and C. Since the number of measurements within the vertical extent of the storm decreases with altitude, Panel B is normalized by the number of measurements at each altitude. Raw counts are shown in Panel C. The distributions from the normalized plot in meters AGL agree with the storm relative altitude distribution; higher altitudes within the storm have more layers without ice cloud.

The general shape of the RH_{ice} distributions within radar coverage (not shown) is very similar to the full dataset in Fig. 4.2A. Nine percent of the radar echo subsample has $RH_{ice} <$ 85%, 65% of which are in the top half of the storm's vertical extent.

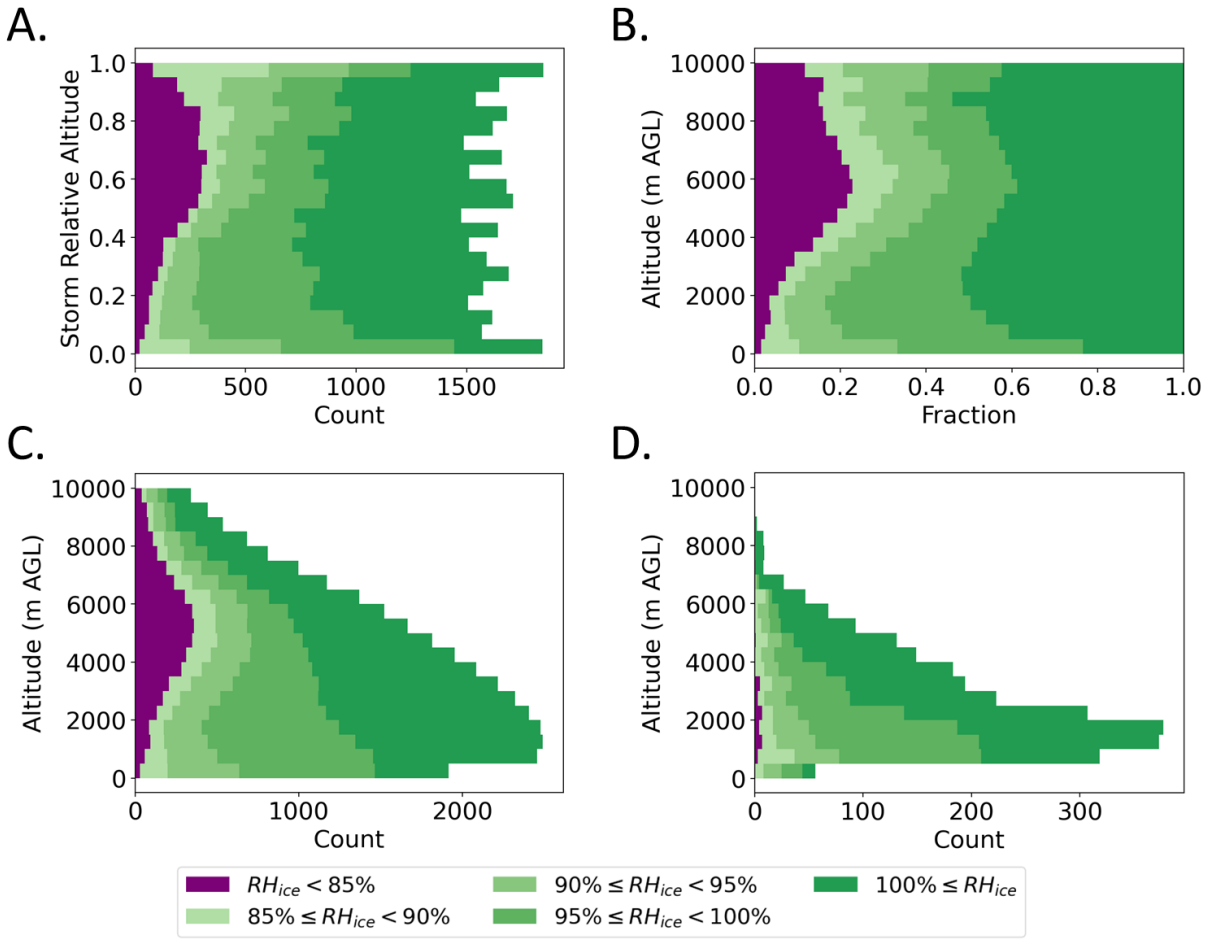

Figure 4.2: Stacked histogram of RH_{ice} measurements within the storm vertical extent for soundings with surface temperatures < 0 °C and precipitation within 500 km of trackable low pressure centers. Panel A. is binned by storm relative altitudes. Panel B. is binned by altitude AGL and normalized by the number of observations at each altitude. Panel C. is binned by altitude AGL. Panel D. is the subset of observations within the vertical extent that also have dBZ > 0, binned by altitude AGL.

Although the frequency of these ice subsaturated layers was lower than anticipated, when they are present they more frequently occur in the top portion of the storm.

Figure 3.8 shows that precipitation radar echos are concentrated at altitudes lower than 4 km. Hence there is a mismatch between where altitudes with precipitation echo are present and altitudes where $RH_{ice} < 85\%$ are more common based on Fig. 4.2. This mismatch was not anticipated when the hypotheses were formulated. Figure 4.2D illustrates this problem: the number of samples with radar precipitation echo altitudes falls off rapidly at altitudes corresponding to > 0.3 of storm vertical extent.

Based on the data available, regions with radar echo > 0 dBZ and sublimating conditions (i.e. sublimation of precipitation-size ice) are very uncommon and suggest that *both hypotheses 1a and 1b should be rejected*. Only 2% of the small sample with radar coverage and precipitation size particles (echo > 0 dBZ) were measured outside of the cloud boundaries (as defined in Section 2.5). For these layers with possible sublimation of precipitation-size ice, 72% were located in the bottom half of the storm. Note that these data sets cannot address sublimation of cloud-sized ice, since the weather radar data are not sensitive enough to detect cloud.

The next hypothesis addresses stability changes that are predicted to be associated with sublimation. If the sublimation occurring within the storm's vertical extent is significant, it should cool the environment enough to influence the local stability profile as modeled by Harris (1977). The predicted signature is a layer of increased stability above the level of maximum sublimative cooling with a layer of decreased stability below it.

Testable Hypothesis 1c: More than 60% of layers without ice cloud but with radar echo in the vertical extent of the storm have an unstable portion in the bottom half of the layer and a stable portion in the upper half of the layer.

As with 1a and 1b, 60% is an *a priori* threshold selected to discern if 'most' of the sublimating layers had the anticipated stability signature.

From the soundings with surface temperatures < 0 °C and surface precipitation within 500 km of trackable low pressure centers, only 19 layers over 15 different soundings were observed with radar echo > 0 dBZ and sublimation ($RH_{ice} < 85\%$). For context, there are 80,149 individual 100 m vertical layers within the storm's extent for 522 soundings within 500 km of trackable lows, with surface precipitation and surface temperatures below freezing. Thus, *there is insufficient data to examine Hypothesis 1c.*

To demonstrate the scarcity of the data, profiles of the conditional and potential stability for only the sublimating layers are shown in Figures 4.3 and 4.4, respectively. Only 1 of the sublimation layers show the hypothesized stable over unstable signature in conditional stability; 4 layers had the signature in potential stability. It is tempting to expand the search criteria to include a more generalized signature of more stability over less stability, but due to the small

number of samples no conclusion would be robust.

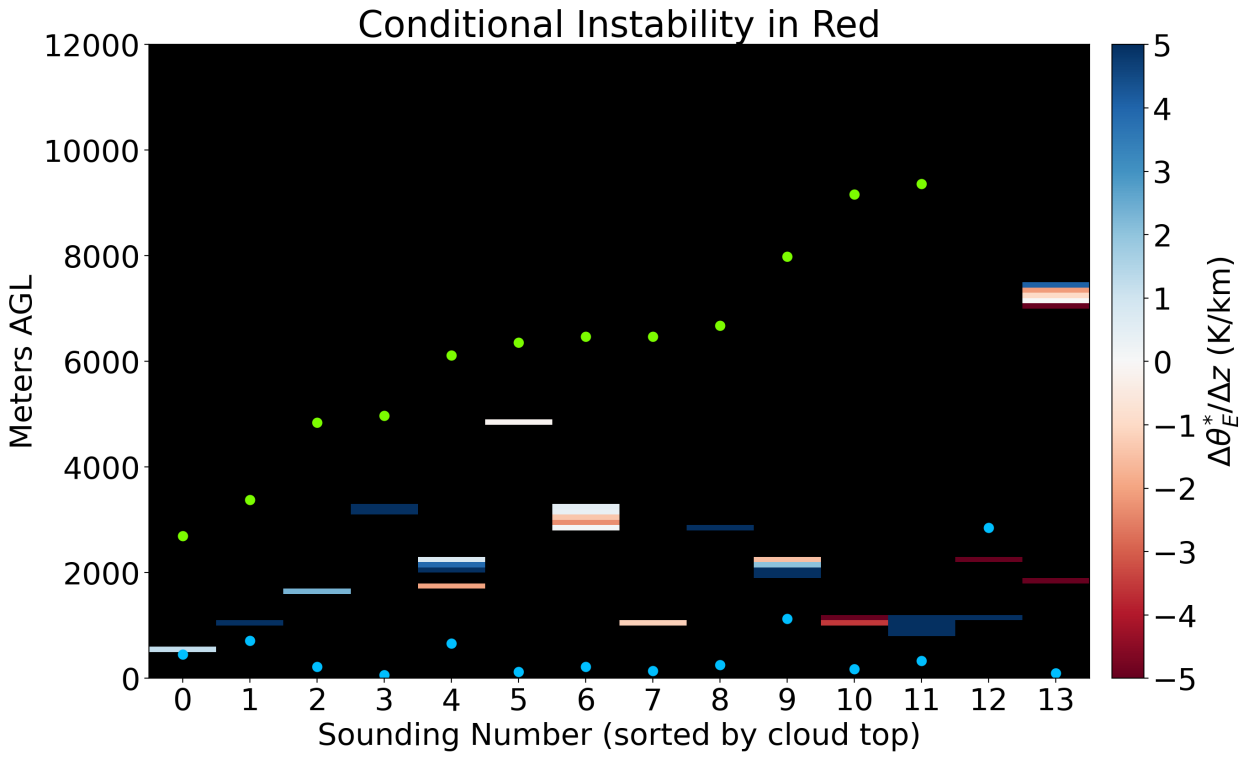

Figure 4.3: Profiles of θ_E^* lapse rates for soundings with surface temperatures < 0 °C and surface precipitation within 500 km of trackable low pressure centers, limited to the subset of subliminating layers. Values less (greater) than 0 K/km are conditionally unstable (stable) and are shaded red (blue). Cloud base (top) is plotted as blue (green) dots.

The final hypothesis for this underlying question addresses the distribution of ice-subsaturated conditions relative to low pressure centers. A preference for layers without ice cloud to occur in the northwest quadrant was anticipated due to dry air from behind the storm intruding into the occlusion.

Testable Hypothesis 1d: Within the storm's vertical extent, more than 40% of observed layers without ice cloud occur in the northwest quadrant relative to the low-pressure center.

To test this hypothesis, all 1,590 soundings within 500 km of trackable lows were used regardless of the surface temperature and precipitation. This was done to yield an improved geographic distribution, though there are still fewer soundings in the SE quadrant than the NW quadrant. For each sounding, the number of 100 m layers within the storm extent without ice cloud are counted. This count is multiplied by 100 m and depth of the dry layers is used for the rest of the calculations. The total depth without ice cloud in each quadrant is normalized by the

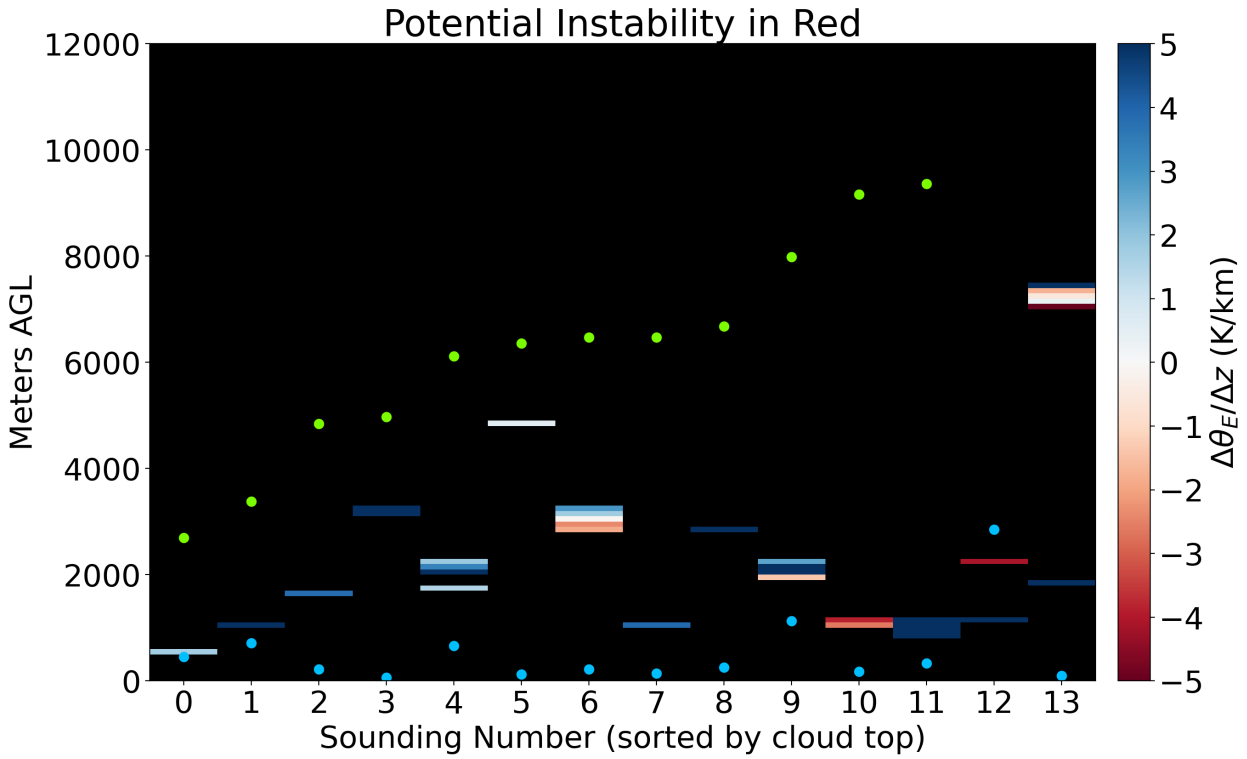

Figure 4.4: Profiles of θ_E lapse rates for soundings with surface temperatures < 0 °C and surface precipitation within 500 km of trackable low pressure centers, limited to the subset of subliminating layers. Values less (greater) than 0 K/km are potentially unstable (stable) and are shaded red (blue). Cloud base (top) is plotted as blue (green) dots.

number of soundings in that quadrant (Table 4.1). In each quadrant, there are soundings with more and less vertical extent of dry layers. The average values are all < 1 km and are similar among the quadrants.

Table 4.1: Characteristics of dry layers (RH_{ice}<85%) within the storm vertical extent for each quadrant relative to the low pressure center.

Quadrant	Avg. Depth of Dry Layers	IQR	Avg. Dry % of storm profile	IQR
NW	880 m	1175 m	13%	22%
NE	800 m	1200 m	12%	18%
SE	910 m	1275 m	15%	30%
SW	810 m	900 m	14%	26%

The mosaic of the percentage of storm extent without ice cloud (where $RH_{ice} < 85\%$) is shown in Figure 4.5. There is no clear preference in geographic locations of the soundings with higher percentages (> 35%) of dry layers within the storm vertical extent. The average percent of storm depth without ice cloud is also shown in Table 4.1. These averages are normalized by the number of soundings in the quadrant. All quadrants are similar; the SE quadrant has the most depth in m and percentage of the storm depth that is without ice cloud. Therefore, *Hypothesis 1d is rejected.*

4.2 Frequency of different types of instability near cloud top

The importance of cloud top instability enhancing ice mass growth is outlined in Section 1.1.3. While the first research question focuses on ice mass loss, the dataset and tools developed to address it are also well suited to investigate cloud top instabilities. Interactions between generating cells and possibly subsaturated layers are also hinted at in Figure 4.1.

Underlying question: What are the frequencies of different types of instability (conditional, potential, or shear) observed at cloud top?

Testable Hypothesis 2: Potential instability is 2x more frequent than either conditional or shear instability within 1 km of cloud top.

As described in Section 1.1.3, potential instability occurs when cold, dry air is above moister air. Since cloud top was defined by a decrease in RH_{ice}, potential instabiltiy was anticipated to be more common than other types of stability near the cloud top.

Referring back to the subset of soundings with surface precipitation and temperature < 0°C within 500 km of trackable lows, the number of stable and unstable layers near cloud top are

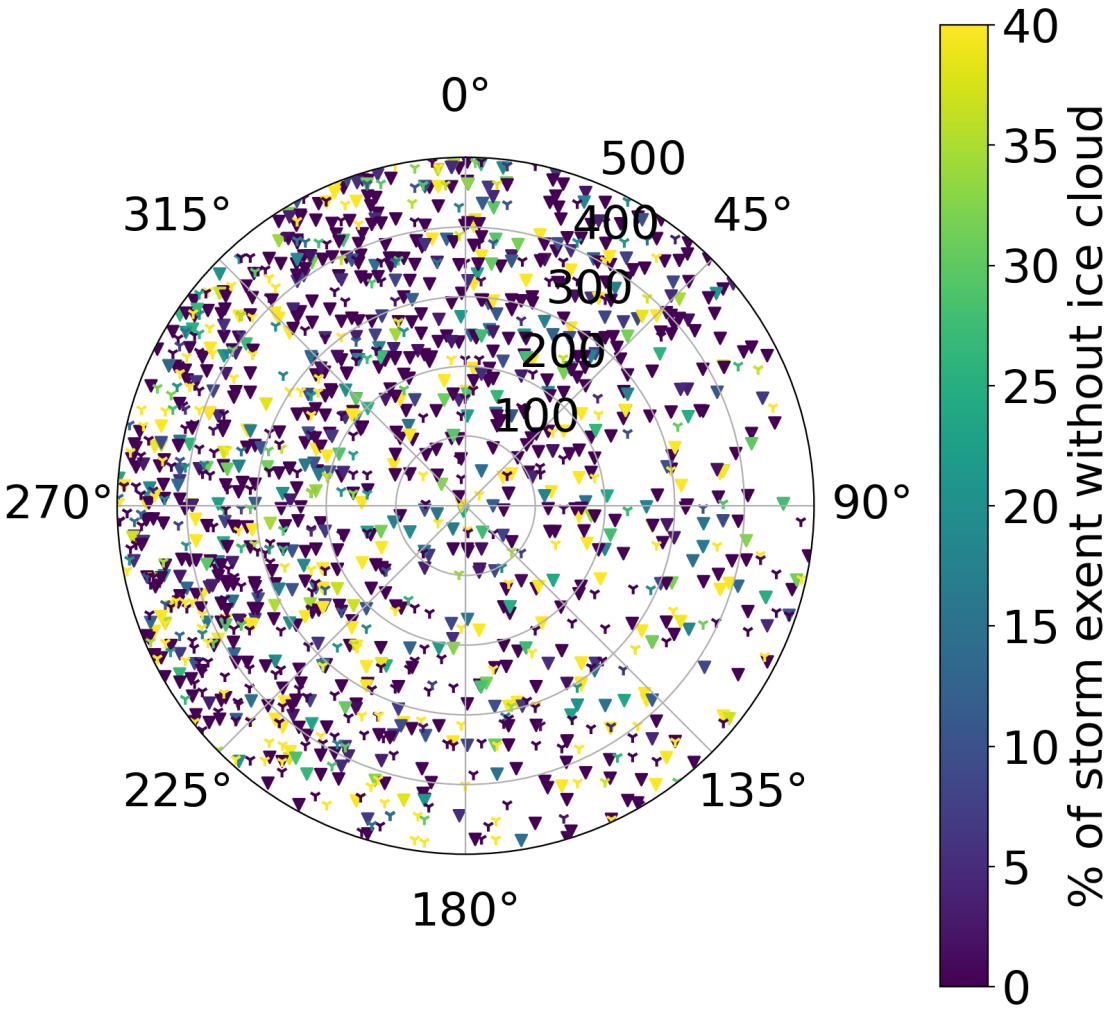

Figure 4.5: Mosiac of the percent of vertical cloud extent with RH_{ice}<85%, for all soundings within 500 km of trackable lows (any surface temperature). Soundings with surface precipitation are marked with a filled triangle; without surface precipitation marked with a "Y"

shown Figures 3.10, 3.12, and 3.15. *This hypothesis is rejected*; within 2 km of cloud top there are 2,046 layers of local conditional instability, 1,713 layers of local potential instability, and 1,748 layers of vertical shear instability. Each type of instability is more prevalent below the cloud top estimate than above it. The frequency of local potentially unstable layers near cloud top is nearly indistinguishable from the frequency of local conditionally unstable layers.

4.3 Summary

The negative results related to sublimation layers rule out certain combinations of conditions from being relevant to quantitative surface precipitation estimation. This dataset does not observe precipitation particles experiencing sublimation as often as the IMPACTS data would suggest. If precipitation-sized ice particles do not typically transit through ice subsaturated environments, then portions of the storm which are producing precipitation have sufficient moisture to maintain ice saturation. Precipitation ice may still encounter ice-subsaturation, but sublimation could reduce reflectivity to less than detectable levels *and* moisten the environment to near saturation in a short time span (order of 10 min). Harris (1977) modeled that the greatest temperature reductions (and thus the most ice mass loss) due to sublimation occurred after precipitation traveled less than 200 m in a subsaturated environment. Clough and Franks (1991) modeled a loss of 95% of ice mass after 700 m of descent. Assuming a snow fall speed of 1 m/s, all evidence of sublimating ice particles could be undetectable after just 12 minutes. The newly moistened environment would be more favorable for the next waves of precipitation. If this time estimate is accurate, detecting such features with a single weather balloon would be extremely rare, as indicated by the dataset.

The negative results related to prevalence of local instabilities suggest that the more steady state, larger scale conditions within winter storms, as revealed by this aggregated analysis of soundings, may be less relevant to precipitation production than transient, smaller scale processes. Examining the sequence of KASPR observations from the Feb 1, 2021 storm shown in Figure 4.1 suggests that overturning motions caused by instabilities are short-lived (∼1 hour), advect away quickly, or both. Precipitation, detected by enhanced reflectivity signatures associated with those motions, takes much longer to descend to the surface. Often the generating cell that produced it is long gone; sometimes new generating cells are present at the cloud top. The odds of detecting such features in soundings launched every 12 hours are very slim.

The dry-over-moist component of potential instability is always present at cloud top (by our definition of cloud top), but the number of potentially unstable layers is no different from other instability types. This suggests that all unstable layers quickly mix out to a neutral state, regardless of how they developed.

CHAPTER

5

CONCLUSIONS AND FUTURE WORK

5.1 Summary of Key Points

This study has amassed data spanning nearly two decades from multiple observation platforms, including 5,403 radiosondes, over 35,000 surface observations, and over 89,000 radar scans. The full dataset was distilled down to focus on 701 trackable low pressure centers during winter storms. This sets it apart from typical case studies which have a very limited number of storms and observations. The pairing of radar reflectivity measurements along the sonde ascent path has not been done in previous sounding climatologies or analyses (Rauber et al. 2001). Except for ERA5 sea level pressure reanalysis used for the low position, all the work done is with observed data. Conclusions are drawn from the best possible measurements of the real world.

Our largest source of uncertainty arises from defining the vertical extent of each storm. While the ASOS ceilometer provides a reasonably robust estimate of cloud base within 60 m, our estimates of cloud top have an estimated typical uncertainty of ~500 m (Fig. 2.11, 2.12). Aspects of the analysis that examine characteristics within 1 km above and below cloud top will be more sensitive to this uncertainty than findings related to the top and bottom halves of vertical extent.

Though the testable hypotheses failed or could not be evaluated because of insufficient sample sizes, the compilation of the sounding dataset provided several insights based on a

large record of winter storms.

1. Weather radar echoes greater than 0 dBZ, indicative of precipitation-sized ice, occurred primarily below 4 km and rarely exceeded 6 km AGL in these storms, even though RH_{ice} conditions > 85% often extended to 8-10 km. These results from a large sample of storms are consistent with NASA IMPACTS and other case studies (McMurdie et al. 2022; Kumjian and Lombardo 2017)).

2. On average, about 11% of storm depth between cloud base and cloud top is subsaturated with respect to ice (< 85% RH_{ice}). Most of these dry layers are in the upper portion of the cloud, above where falling precipitation-size ice is present. Hence, processes that entrain dry air from these "sandwiched" dry layers in between cloud layers will reduce cloud-ice mass more commonly than precipitation-ice mass. Very few layers subsaturated with respect to ice correspond to regions with weather radar echo > 0 dBZ.

3. In contrast to conceptual models that indicate horizontal advection of dry air intrudes preferentially in the NW quadrant of the cyclone, all four quadrants have similar average total vertical depths of dry layers between the cloud top and cloud base (Table 4.1).

4. As expected from conceptual models, the layer above 1 km cloud top is more locally stable for conditional, potential, and shear instabilities than the layer 1 km below cloud top. Observing this signature gives confidence that the cloud top estimate used is reasonably close to the real value for most cases.

5. As expected from conceptual models, the vast majority of vertical storm extent is neutral with respect to conditional and potential stability.

6. The moist Richardson number values indicating possible presence of Kelvin-Helmholtz waves occur about 15% of the time at each level throughout the vertical extent of the cloud (Fig. 3.18).

7. Enhanced wind shear is common within a few 100 m of cloud top which, suggests cloud top entrainment of dry air is nearly always occurring (Figs. 3.20 and 3.21).

8. In the lowest 2 km of the profiles, there is both more frequently occurring wind shear than higher altitudes and more frequently occurring local conditional and potential stable layers compared to higher altitudes. These competing factors imply the boundary layer wind shear instabilities will be damped (Figs. 3.20 and 3.21).

9. The median depth of layers with vertical shear instability within a storm are 500 m for NW and NE quadrants, 200 m for SW quadrant. This equates to about 8% of vertical storm depth for the NW and NE quadrants.

10. In the NE and NW quadrants, cloud tops have median values 1.5 km higher than the SW quadrant (Table 3.1), which consistent with expectations from conceptual models of where large scale ascent is present (Figs. 1.1).

11. There are no obvious gradients in cloud base height relative to distance from the low pressure center (Fig. 3.3). Median cloud base heights are 400, 600, and 800 m for NW, NE and SW quadrants respectively (Table 3.1). Notably, the NW quadrant has a much smaller interquartile range as compared to NE and SW quadrants.

5.1.1 Discussion

In general, instabilities in the atmosphere are ephemeral; those that develop will mix out. Neutral and stable conditions can be persistent, and dominate the observed data. Local stability was targeted in this analysis due to the anticipated local effects from sublimative cooling. Due to infrequency of falling precipitation-sized ice particles in subsaturated layers, the local stability does not seem to have significant impacts on the storm structure. Examination of non-local static stability will address lifting and sinking parcel motions across layers more comprehensively than local stability analysis (Stull 1991). This non-local stability analysis is yet to be done.

Work with our collaborators at Stony Brook University, which utilized high spatial and temporal resolution cloud radar data in winter storm, has indicated that locations with 100 m and < 20 second scale updrafts often coincide with higher turbulence and moist shear instabilities (Oue et al. 2023). Additionally, these storms often contain multiple, very thin layers of turbulent flow sandwiched between more laminar flow (E. Leghart, personal communication).

The sounding-based shear instability results suggest that enhanced wind shear, and Kelvin-Helmholtz instabilities frequently occurring near cloud top are relevant for examining dry air entrainment and warrant further study. A missing piece that cannot be addressed with this data set is the magnitude of dry air entrainment and the amount of subsequent cloud ice mass loss, which occurs at cloud top as well as along the edges of the upper portions of the storm.

5.2 Future Work

Significant errors in duration, liquid water equivalent, and ice mass accumulation are still present in forecasts of wintry precipitation, indicating that numerical models are not capturing key processes. Ice particles were commonly observed in ice-subsaturated conditions by the NASA IMPACTS field campaign, but without more details on the vertical profile of temperature and moisture, the implications of this observation remain incomplete. In addition to sublimation, these ice particles have complicated microphysical histories demonstrated by different growth modes and riming. A future study could pair a sensitive radar with many soundings targeting an individual storm to quantify areas with sublimating ice particles. The KASPR in RHI mode (shown in Figure 4.1) could provide cross sections of reflectivity with fast updates. The RHI scan is necessary to prevent gaps in the vertical dimension and decrease the time between each scan. Strategically selecting radiosonde launch sites to place the sonde flight path in the RHI cross section would provide the necessary temperature and humidity data. Having multiple soundings in flight at once would provide more than one data point in temperature and humidity per scan. This would address problems in this study due to the low sensitivity of the NEXRAD and the low frequency of soundings in any given storm.

The predominant low pressure system in this study was the Hatteras Low. Air masses that influence these cyclones are maritime tropical from the south and east, maritime polar from the north and east, and continental polar from the northwest. The two maritime air masses provide significant amounts of moisture to these storms. If the geographic domain was extended across the United States, different climatologies from Colorado Lows and Alberta Clippers could be evaluated. Air masses affecting these inland storms are continental polar air from Canada and maritime air from the Gulf of Mexico. Storms in the central plains may have greater distinctions relative to the low pressure centers since there is less maritime air available to them.

The biggest practical challenge to expanding the geographic domain in the near term would be accessing the NEXRAD data. Initial attempts to download all the necessary radar data from AWS at once resulted in blocked connections due to the large request ($\sim$ 300 GB). Limiting requests to fetch NEXRAD data for just a few soundings at a time makes the pairing process wait for network traffic before completing. Those wishing to expand the study domain should take note of the computation, network, and data requirements. The matching of soundings with radar data is a computation intensive process. It took 240+ compute hours to pair radar data to the sonde position for the 5,500 soundings in the study domain during winter months between 2005 and 2022. (Multiprocessing techniques make this tractable.)

Using the already processed data on hand, vertical profiles of horizontal moisture advection could be computed. These could be put into a framework relative to trackable lows which

would aid in interpretation of physical processes responsible for varying cloud top heights and depth of dry layers in different quadrants.

The tools developed for this study were developed with future expanded use in mind. Members of the research group are already using SIR plots to inform analysis of individual storms from the NASA IMPACTS field study. SIR plots could be used to verify operational models with a focus on winter storm properties. Soundings from numerical weather models could be incorporated into the relational database, and all the visualizations and calculations could be applied to model-derived soundings as well. Research models with very short timesteps could be investigated to see how profiles of stability and moisture develop during winter storms.

REFERENCES

Alduchov, O. A. and Eskridge, R. E. (1996). Improved Magnus Form Approximation of Saturation Vapor Pressure. *Journal of Applied Meteorology and Climatology*, 35(4):601 – 609.

Allen, L., Tomkins, L., Yuter, S., Miller, M., Peele, T., Hueholt, D., Harley, R., Mclinden, M., Li, L., Yang-Martin, M., Bennett, R., Thornhill, L., and Poelott, M. (2021). Ambient Environments for Ice Mass Growth and Shrinkage in the Context of Winter Storm Structure.

American Meteorological Society (2022). Pseudoadiabatic lapse rate - Glossary of Meteorology.

American Meteorological Society (2023). Psychrometric formula - Glossary of Meteorology.

Bader, M. J., Forbes, G. S., Grant, J. R., Lilley, R. B. E., and Waters, A. J. (1995). *Images in weather forecasting. A practical guide for interpreting satellite and radar imagery*. Cambridge University Press, Cambridge.

Barnett, T. P., Adam, J. C., and Lettenmaier, D. P. (2005). Potential impacts of a warming climate on water availability in snow-dominated regions. *Nature 2005 438:7066*, 438(7066):303–309.

Barton, D. K. (2013). *Radar equations for modern radar*. Boston : Artech House, [2013], Boston.

Bolton, D. (1980). The Computation of Equivalent Potential Temperature. *Monthly Weather Review*, 108(7):1046 – 1053.

Carlson, T. N. (1980). Airflow Through Midlatitude Cyclones and the Comma Cloud Pattern. *Monthly Weather Review*, 108(10):1498 – 1509.

Clough, S. A. and Franks, R. A. (1991). The evaporation of frontal and other stratiform precipitation. *Quarterly Journal of the Royal Meteorological Society*, 117(501):1057–1080.

Clough, S. A., Lean, H. W., Roberts, N. M., and Forbes, R. M. (2000). Dynamical effects of ice sublimation in a frontal wave. *Quarterly Journal of the Royal Meteorological Society*, 126(568):2405–2434.

Crosier, J., Choularton, T. W., Westbrook, C. D., Blyth, A. M., Bower, K. N., Connolly, P. J., Dearden, C., Gallagher, M. W., Cui, Z., and Nicol, J. C. (2014). Microphysical properties of cold frontal rainbands†. *Quarterly Journal of the Royal Meteorological Society*, 140(681):1257–1268.

Evans, A. G., Locatelli, J. D., Stoelinga, M. T., and Hobbs, P. V. (2005). The IMPROVE-1 Storm of 1–2 February 2001. Part II: Cloud Structures and the Growth of Precipitation. *Journal of the Atmospheric Sciences*, 62(10):3456–3473.

Federal Highway Administration (2022). Snow & Ice.

Forbes, R. M. and Hogan, R. J. (2006). Observations of the depth of ice particle evaporation beneath frontal cloud to improve NWP modelling. *Quarterly Journal of the Royal Meteorological Society*, 132(616):865–883.

Fovell, R. G. and Gallagher, A. (2020). Boundary layer and surface verification of the high-resolution rapid refresh, version 3. *Weather and Forecasting*, 35(6):2255–2278.

Ganetis, S. A., Colle, B. A., Yuter, S. E., and Hoban, N. P. (2018). Environmental Conditions Associated with Observed Snowband Structures within Northeast U.S. Winter Storms. *Monthly Weather Review*, 146(11):3675 – 3690.

Harris, F. I. (1977). The Effects of Evaporation at the Base of Ice Precipitation Layers: Theory and Radar Observations. *Journal of Atmospheric Sciences*, 34(4):651 – 672.

Helmus, J. J. and Collis, S. M. (2016). The Python ARM Radar Toolkit (Py-ART), a Library for Working with Weather Radar Data in the Python Programming Language. *Journal of Open Research Software*, 4(1):25.

Hersbach, H., Bell, B., Berrisford, P., Biavati, G., Horányi, A., Muñoz Sabater, J., Nicolas, J., Peubey, C., Radu, R., Rozum, I., Schepers, D., Simmons, A., Soci, C., Dee, D., and Thépaut, J.-N. (2018). ERA5 hourly data on single levels from 1959 to present.

Herzegh, P. H. and Hobbs, P. V. (1980). The Mesoscale and Microscale Structure and Organization of Clouds and Precipitation in Midlatitude Cyclones. II: Warm-Frontal Clouds. *Journal of Atmospheric Sciences*, 37(3):597 – 611.

Hobbs, P. (1978). Organization and structure of clouds and precipitation on the mesoscale and microscale in cyclonic storms. *Reviews of Geophysics*, 16(4):741–755.

Houze, R. A. (1989). Observed structure of mesoscale convective systems and implications for large-scale heating. *Quarterly Journal of the Royal Meteorological Society*, 115(487):425–461.

Houze, R. A. (1993). *Cloud dynamics*. Academic Press.

Houze, R. A. (2014). *Cloud Dynamics*. Academic Press, 2nd edition.

Houze, R. A., Rutledge, S. A., Matejka, T. J., and Hobbs, P. V. (1981). The Mesoscale and Microscale Structure and Organization of Clouds and Precipitation in Midlatitude Cyclones. III: Air Motions and Precipitation Growth in a Warm-Frontal Rainband. *Journal of Atmospheric Sciences*, 38(3):639 – 649.

Keeler, J. M., Jewett, B. F., Rauber, R. M., McFarquhar, G. M., Rasmussen, R. M., Xue, L., Liu, C., and Thompson, G. (2016a). Dynamics of Cloud-Top Generating Cells in Winter Cyclones. Part I: Idealized Simulations in the Context of Field Observations. *Journal of the Atmospheric Sciences*, 73(4):1507–1527.

Keeler, J. M., Jewett, B. F., Rauber, R. M., McFarquhar, G. M., Rasmussen, R. M., Xue, L., Liu, C., and Thompson, G. (2016b). Dynamics of cloud-top generating cells in winter cyclones. Part II: Radiative and instability forcing. *Journal of the Atmospheric Sciences*, 73(4):1529–1553.

Keeler, J. M., Rauber, R. M., Jewett, B. F., Mcfarquhar, G. M., Rasmussen, R. M., Xue, L., Liu, C., and Thompson, G. (2017). Dynamics of cloud-top generating cells in winter cyclones. Part III: Shear and convective organization. *Journal of the Atmospheric Sciences*, 74(9):2879–2897.

Kent, L. M. (2021). *Multi-Year Analysis of Ice Streamers within Coastal Northeast US Winter Storms*. PhD thesis, North Carolina State University.

Kocin, P. J. and Uccellini, L. W. (2004). Summary, Forecast Advances, and a Northeast Snowfall Impact Scale (NESIS). In Kocin, P. J. and Uccellini, L. W., editors, *Northeast Snowstorms: Volume I: Overview / Volume II: The Cases*, pages 233–270. American Meteorological Society, Boston, MA.

Kumjian, M. R. and Lombardo, K. A. (2017). Insights into the Evolving Microphysical and Kinematic Structure of Northeastern U.S. Winter Storms from Dual-Polarization Doppler Radar. *Monthly Weather Review*, 145(3):1033 – 1061.

Kumjian, M. R., Rutledge, S. A., Rasmussen, R. M., Kennedy, P. C., and Dixon, M. (2014). High-Resolution Polarimetric Radar Observations of Snow-Generating Cells. *Journal of Applied Meteorology and Climatology*, 53(6):1636–1658.

Maneewongvatana, S. and Mount, D. (2002). Analysis of approximate nearest neighbor searching with clustered point sets. In Goldwasser, M., Johnson, D., and McGeoch, C., editors, *Data Structures, Near Neighbor Searches, and Methodology: Fifth and Sixth DIMACS Implementation Challenges*, pages 105–123. American Mathematical Society.

Markowski, P. and Richardson, Y. (2010). *Mesoscale meteorology in midlatitudes*. Chichester, West Sussex ; Hoboken, NJ : Wiley-Blackwell, Chichester, West Sussex ; Hoboken, NJ Chichester.

Marshall, J. S. and Palmer, W. M. K. (1948). THE DISTRIBUTION OF RAINDROPS WITH SIZE. *Journal of Atmospheric Sciences*, 5(4):165 – 166.

Matejka, T. J., Houze, R. A., and Hobbs, P. V. (1980). Microphysics and dynamics of clouds associated with mesoscale rainbands in extratropical cyclones. *Quarterly Journal of the Royal Meteorological Society*, 106(447):29–56.

May, R. M., Goebbert, K. H., Thielen, J. E., Leeman, J. R., Camron, M. D., Bruick, Z., Bruning, E. C., Manser, R. P., Arms, S. C., and Marsh, P. T. (2022). MetPy: A Meteorological Python Library for Data Analysis and Visualization. *Bulletin of the American Meteorological Society*, 103(10):E2273 – E2284.

McMurdie, L. A., Heymsfield, G. M., Yorks, J. E., Braun, S. A., Skofronick-Jackson, G., Rauber, R. M., Yuter, S., Colle, B., McFarquhar, G. M., Poellot, M., Novak, D. R., Lang, T. J., Kroodsma, R., McLinden, M., Oue, M., Kollias, P., Kumjian, M. R., Greybush, S. J., Heymsfield, A. J., Finlon, J. A., McDonald, V. L., and Nicholls, S. (2022). Chasing Snowstorms: The Investigation of Microphysics and Precipitation for Atlantic Coast-Threatening Snowstorms (IMPACTS) Campaign. *Bulletin of the American Meteorological Society*, 103(5):E1243–E1269.

National Centers for Environmental Information and Yin, X. (2021). US Radiosonde BUFR Archive.

National Oceanic and Atmospheric Administration, National Aeronautics and Space Administration, and United States Air Force (1976). U.S. Standard Atmosphere, 1976. Technical report, Washington, DC.

Office of the Federal Coordinator for Meteorological Services (2011). Doppler Radar Meteorological Observations Part A.

Oue, M., Colle, B. A., Yuter, S. E., Kollias, P., Yeh, P., and Tomkins, L. M. (2023). Microscale Updrafts Within the U.S. Northeast Coastal Snowstorms Using High-Resolution Cloud Radar Measurements. *Monthly Weather Review*.

Oue, M., Kollias, P., Luke, E. P., and Ryzhkov, A. (2017). A New Ka-Band Scanning Radar Facility: Polarimetric and Doppler Spectra Measurements of Snow Events. In *AGU Fall Meeting, A31G-2270*, New Orleans.

Peele, T., Allen, L., Yuter, S., Iii, R. H., Hueholt, D., Miller, M., Tomkins, L., Yang-Martin, M., Bennett, R., Mclinden, M., Li, L., and Schnaiter, M. (2021). Ice Growth Environments and Snow Geometries Sampled During NASA IMPACTS.

Plummer, D. M., McFarquhar, G. M., Rauber, R. M., Jewett, B. F., and Leon, D. C. (2014). Structure and Statistical Analysis of the Microphysical Properties of Generating Cells in the Comma Head Region of Continental Winter Cyclones. *Journal of the Atmospheric Sciences*, 71(11):4181–4203.

Rauber, R. M., Olthoff, L. S., Ramamurthy, M. K., Miller, D., and Kunkel, K. E. (2001). A Synoptic Weather Pattern and Sounding-Based Climatology of Freezing Precipitation in the United States East of the Rocky Mountains. *Journal of Applied Meteorology*, 40(10):1724 – 1747.

Registry of Open Data on AWS (2022). NEXRAD on AWS.

Roebber, P. J., Bruening, S. L., Schultz, D. M., and Cortinas, J. V. (2003). Improving Snowfall Forecasting by Diagnosing Snow Density. *Weather and Forecasting*, 18(2):264 – 287.

Romps, D. M. (2021). Accurate Expressions for the Dewpoint and Frost Point Derived from the Rankine–Kirchhoff Approximations. *Journal of the Atmospheric Sciences*, 78(7):2113–2116.

Smith, A., Lott, N., and Vose, R. (2011). The integrated surface database: Recent developments and partnerships. *Bulletin of the American Meteorological Society*, 92(6):704–708.

Stull, R. B. (1991). Static Stability—An Update. *Bulletin of the American Meteorological Society*, 72(10):1521 – 1530.

Tomkins, L., Yuter, S., Aponte-Torres, A., and Miller, M. (2022a). Analysis of ER-2 data to elucidate how the trajectories of ice particles are modified by horizontal air motions and wind shear.

Tomkins, L. M., Yuter, S. E., Miller, M. A., and Allen, L. R. (2022b). Image muting of mixed precipitation to improve identification of regions of heavy snow in radar data. *Atmos. Meas. Tech*, 15:5515–5525.

Vaisala (2017). Vaisala Radiosonde RS41-SG Temperature and Humidity Sensors.

Virtanen, P., Gommers, R., Oliphant, T. E., Haberland, M., Reddy, T., Cournapeau, D., Burovski, E., Peterson, P., Weckesser, W., Bright, J., van der Walt, S. J., Brett, M., Wilson, J., Millman, K. J., Mayorov, N., Nelson, A. R. J., Jones, E., Kern, R., Larson, E., Carey, C. J., Polat, I., Feng, Y., Moore, E. W., VanderPlas, J., Laxalde, D., Perktold, J., Cimrman, R., Henriksen, I., Quintero, E. A., Harris, C. R., Archibald, A. M., Ribeiro, A. H., Pedregosa, F., van Mulbregt, P., Vijaykumar, A., Bardelli, A. P., Rothberg, A., Hilboll, A., Kloeckner, A., Scopatz, A., Lee, A., Rokem, A., Woods, C. N., Fulton, C., Masson, C., Häggström, C., Fitzgerald, C., Nicholson, D. A., Hagen, D. R., Pasechnik, D. V., Olivetti, E., Martin, E., Wieser, E., Silva, F., Lenders, F., Wilhelm, F., Young, G., Price, G. A., Ingold, G.-L., Allen, G. E., Lee, G. R., Audren, H., Probst, I., Dietrich, J. P., Silterra, J., Webber, J. T., Slavič, J., Nothman, J., Buchner, J., Kulick, J., Schönberger, J. L., de Miranda Cardoso, J. V., Reimer, J., Harrington, J., Rodríguez, J. L. C., Nunez-Iglesias, J., Kuczynski, J., Tritz, K., Thoma, M., Newville, M., Kümmerer, M., Bolingbroke, M., Tartre, M., Pak, M., Smith, N. J., Nowaczyk, N., Shebanov, N., Pavlyk, O., Brodtkorb, P. A., Lee, P., McGibbon, R. T., Feldbauer, R., Lewis, S., Tygier, S., Sievert, S., Vigna, S., Peterson, S., More, S., Pudlik, T., Oshima, T., Pingel, T. J., Robitaille, T. P., Spura, T., Jones, T. R., Cera, T., Leslie, T., Zito, T., Krauss, T., Upadhyay, U., Halchenko, Y. O., and Vázquez-Baeza, Y. (2020). SciPy 1.0: fundamental algorithms for scientific computing in Python. *Nature Methods*, 17(3):261–272.

Wallace, J. M. and Hobbs, P. V. (2006). *Atmospheric science : an introductory survey*. Amsterdam ; Boston : Elsevier Academic Press, Amsterdam ; Boston, 2nd ed.. edition.

Ward, G. (2023). Forecasting Synoptic Scale Weather Associated With Frontal Systems – Meteorology101.

Wexler, R. and Atlas, D. (1959). PRECIPITATION GENERATING CELLS. *Journal of Atmospheric Sciences*, 16(3):327 – 332.

World Meteorological Organization (2022). WIS Manuals.

APPENDICES

APPENDIX

A

ADDITIONAL FIGURES DEMONSTRATING THE 95% RH_{ice} CLOUND BOUNDARY

A selection of figures from the main chapters are reproduced here using $RH_{ice} \geq 95\%$ to denote the boundary of ice clouds as described in Section 2.5.

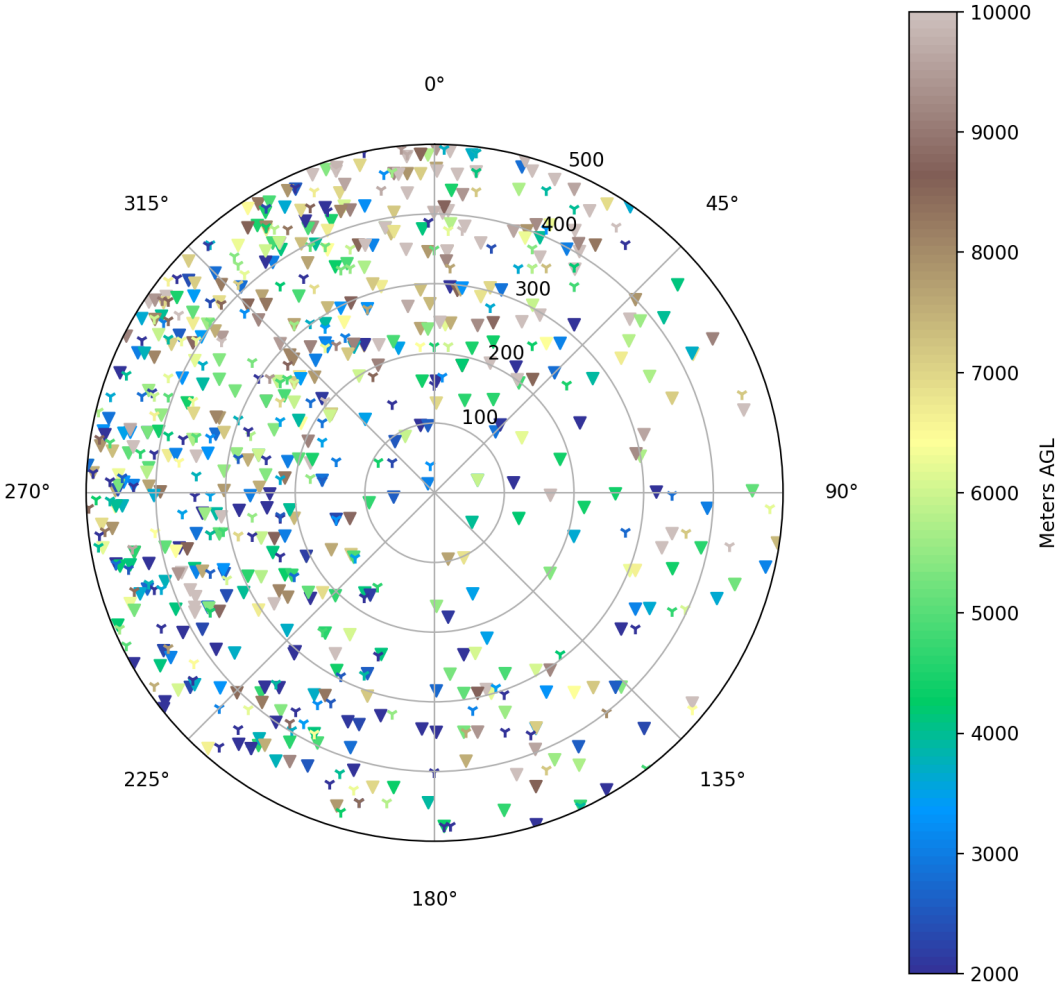

Figure A.1: Mosaic of cloud top altitude (defined by the highest altitude of $RH_{ice} \geq 95\%$) relative to trackable low pressure centers for soundings with surface temperatures < 0 °C. Soundings with surface precipitation are marked with a filled triangle; without surface precipitation marked with a "Y". Color coding is cloud top altitude. Higher cloud tops are most prevalent north and northwest of the low. Paired with Figure 3.2.

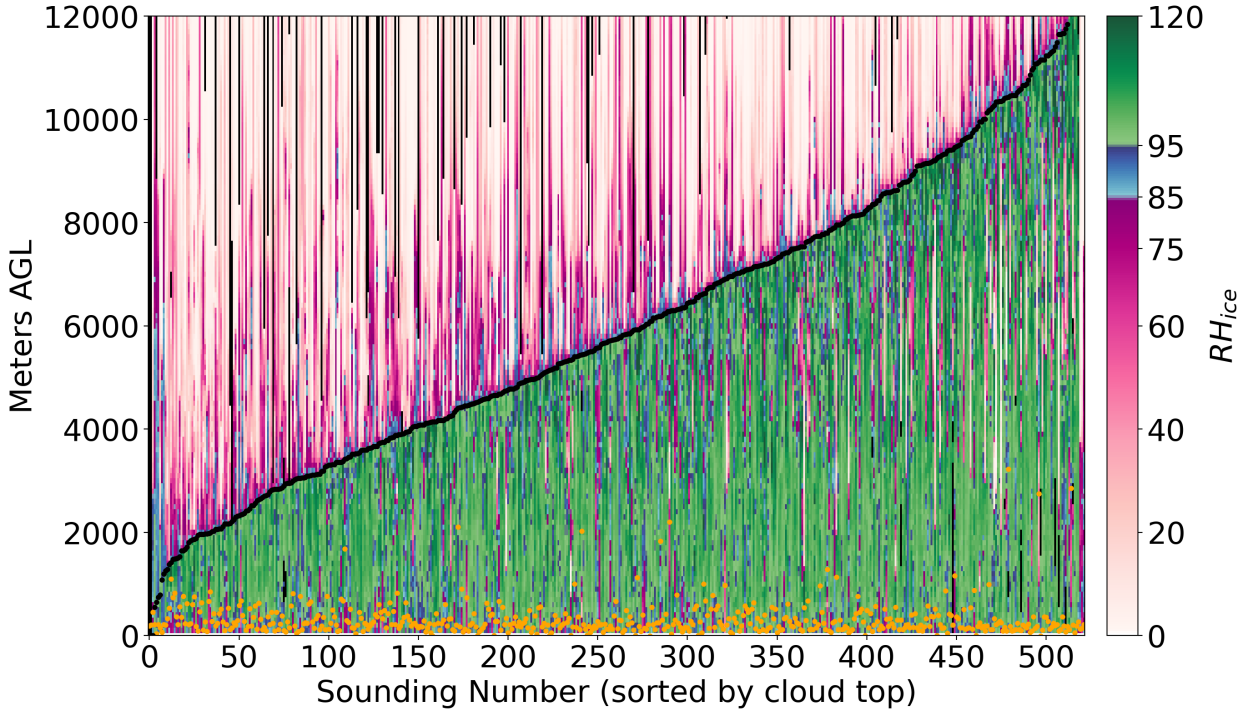

Figure A.2: Profiles of RH_{ice} from soundings with surface temperatures < 0 °C and surface precipitation within 500 km of trackable low pressure centers. Profiles are color coded by RH_{ice} value in each 100 m layer. Each column represents one sounding. Soundings are sorted based on first the estimated cloud top (black, defined by the highest altitude of $RH_{ice} \geq 95\%$) and second on the ASOS ceilometer cloud base (orange). Many profiles have areas of RH_{ice}<95% between the cloud base and top indicating likely zones of sublimation. Most of these non-cloud areas are located in the top-half of the storm's vertical extent, but there are several examples within 1 km of the cloud base as well. Paired with Figure 3.4.

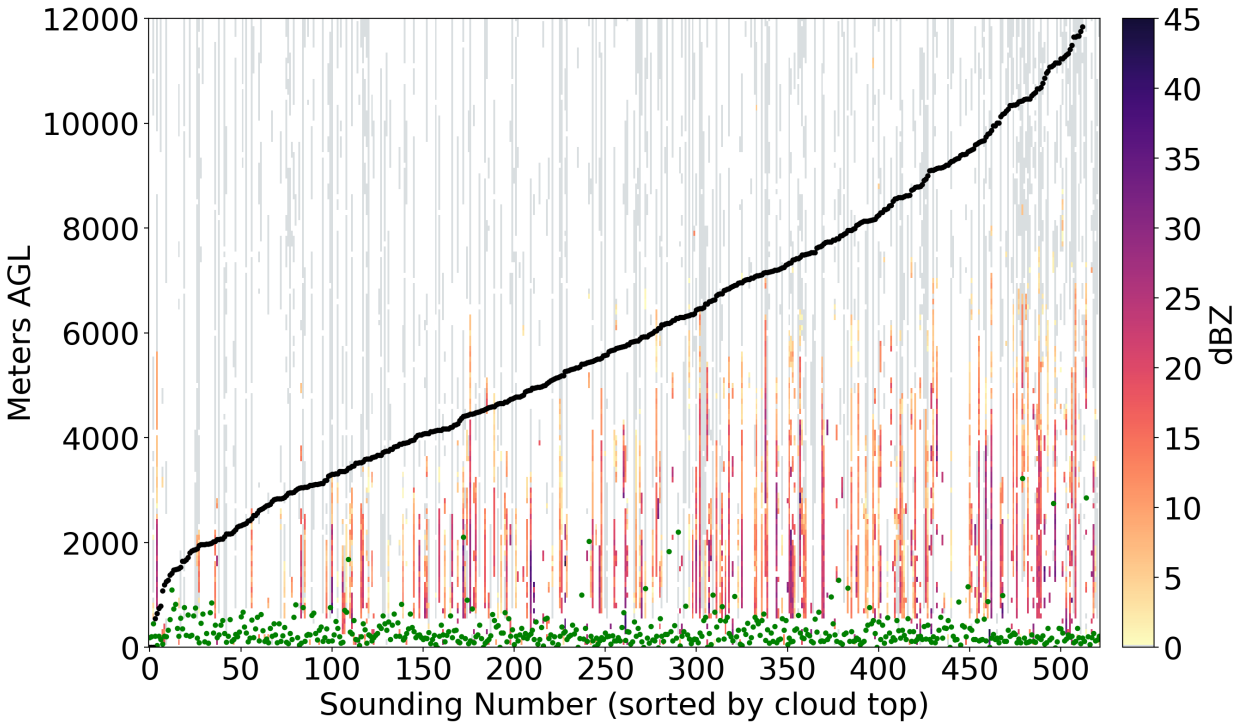

Figure A.3: Profiles of NEXRAD reflectivity matched to sonde positions for soundings with surface temperatures < 0 °C and surface precipitation within 500 km of trackable low pressure centers. Reflectivity values greater than 0 dBZ are color coded, areas with radar coverage but dBZ <0 are gray. Layers when the sonde is outside of the radar beam are white (no data). Cloud base indicated by green dots and cloud top (defined by the highest altitude of $RH_{ice} \geq 95\%$) by black dots. Paired with Figure 3.8.

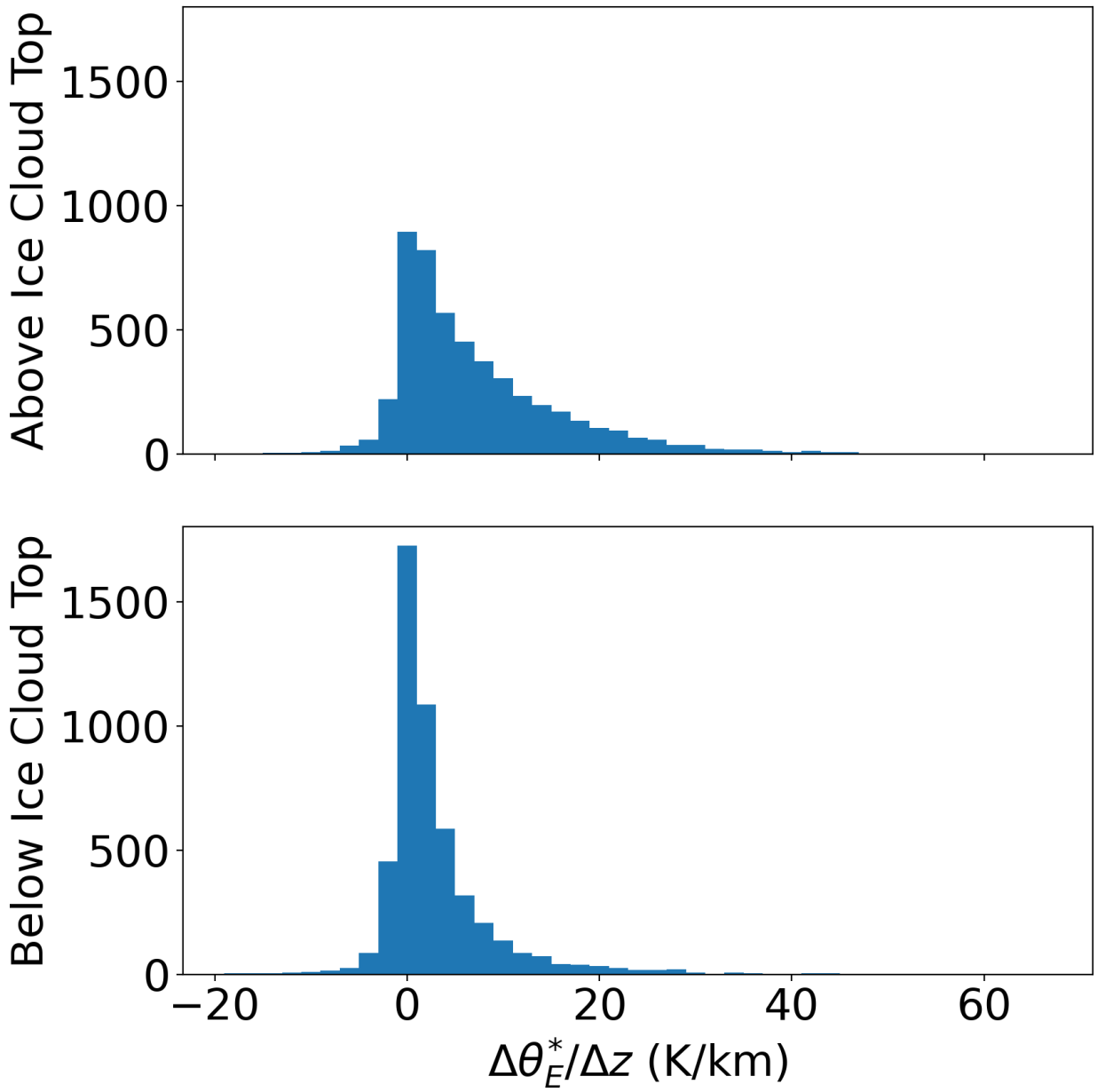

Figure A.4: Histograms of θ_E^* lapse rates 1 km above and 1 km below cloud top (defined by the highest altitude of $RH_{ice} \geq 95\%$) from soundings with surface temperatures < 0 °C and precipitation within 500 km of trackable low pressure centers. Values <0 K/km are conditionally unstable. The longer tail of stable lapse rates above the cloud top indicates increased stability above the storm vertical extent. Paired with Figure 3.10.

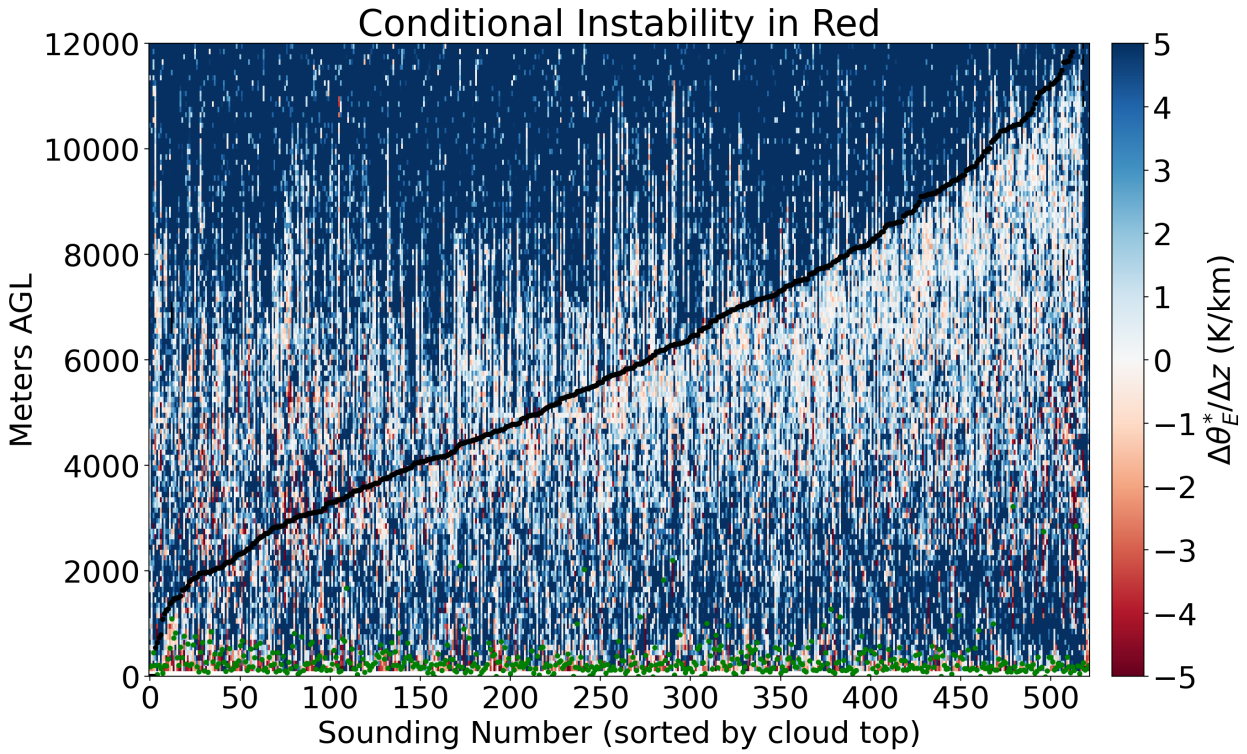

Figure A.5: Profiles of θ_E^* lapse rates for soundings with surface temperatures < 0 °C and surface precipitation within 500 km of trackable low pressure centers. Values less (greater) than 0 K/km are conditionally unstable (stable) and are shaded red (blue). Cloud base indicated by green dots and cloud top (defined by the highest altitude of $RH_{ice} \geq 95\%$) by black dots. Paired with Figure 3.11.

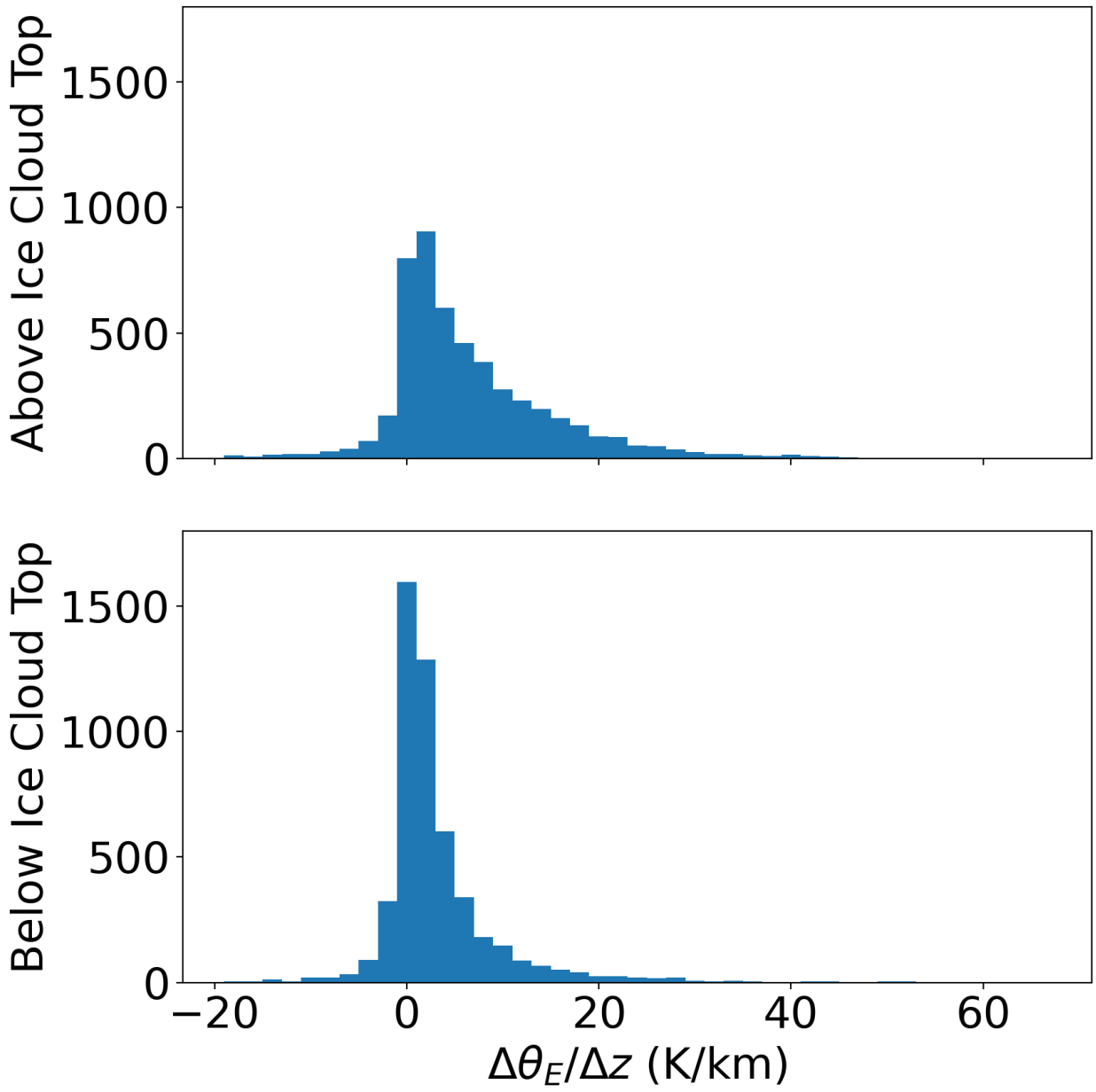

Figure A.6: Histograms of θ_E lapse rates 1 km above and 1 km below cloud top (defined by the highest altitude of $RH_{ice} \geq 95\%$) from soundings with surface temperatures < 0 °C and precipitation within 500 km of trackable low pressure centers. Values <0 K/km are potentially unstable. The longer tail of stable lapse rates above the cloud top indicates increased stability above the storm vertical extent. Paired with Figure 3.12.

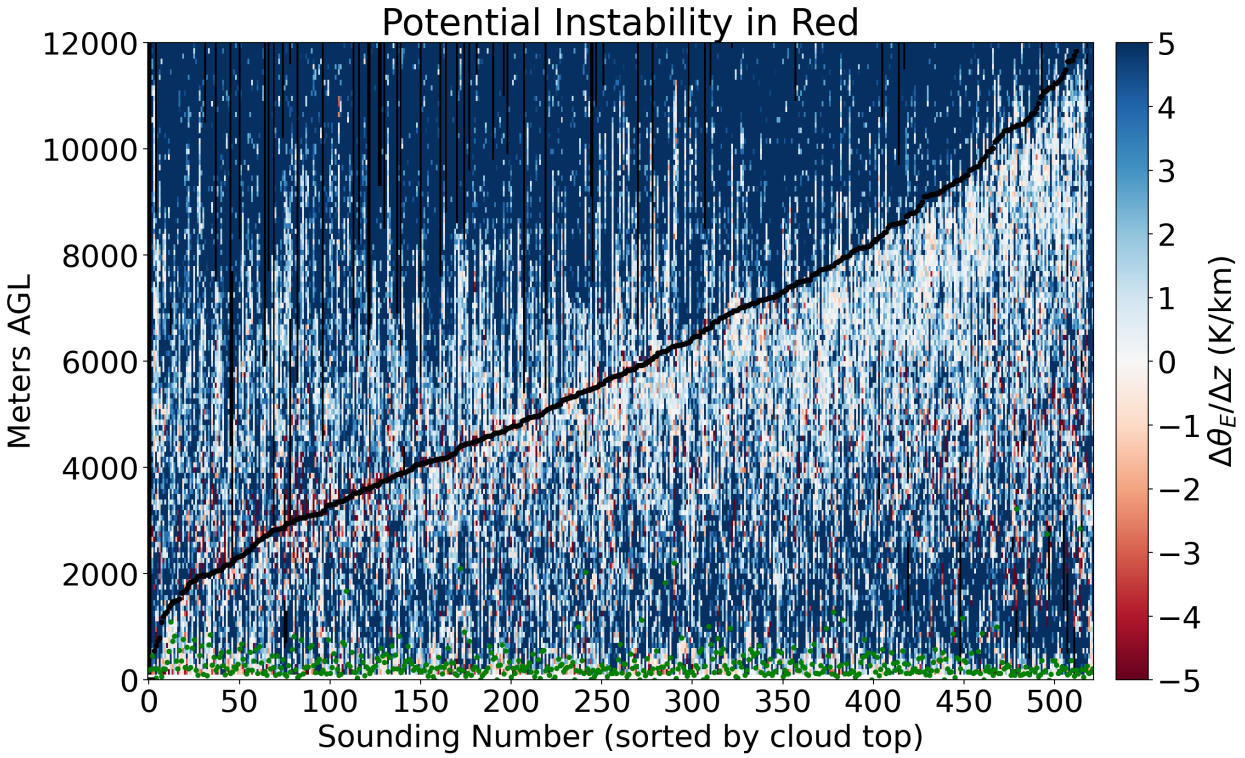

Figure A.7: Profiles of θ_E lapse rates for soundings with surface temperatures < 0 °C and surface precipitation within 500 km of trackable low pressure centers. Values less (greater) than 0 K/km are potentially unstable (stable) and are shaded red (blue). Cloud base indicated by green dots and cloud top (defined by the highest altitude of $RH_{ice} \geq 95\%$) by black dots. Paired with Figure 3.13.

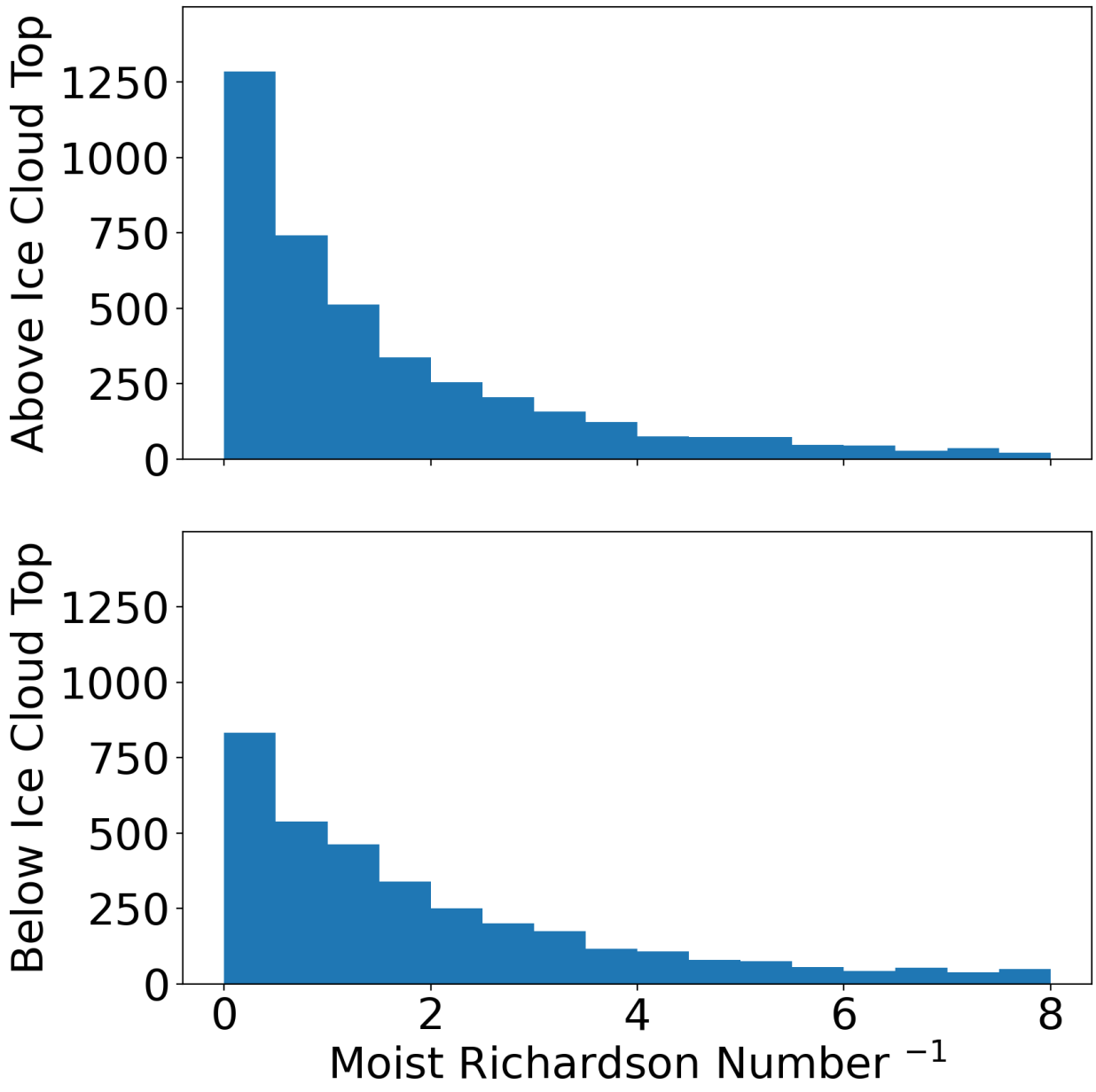

Figure A.8: Histograms of mRi^{-1} 1 km above and 1 km below cloud top ((defined by the highest altitude of $RH_{ice} \geq 95\%$) from soundings with surface temperatures < 0 °C and precipitation within 500 km of trackable low pressure centers. Values greater than 4 have vertical shear instability. Paired with Figure 3.15.

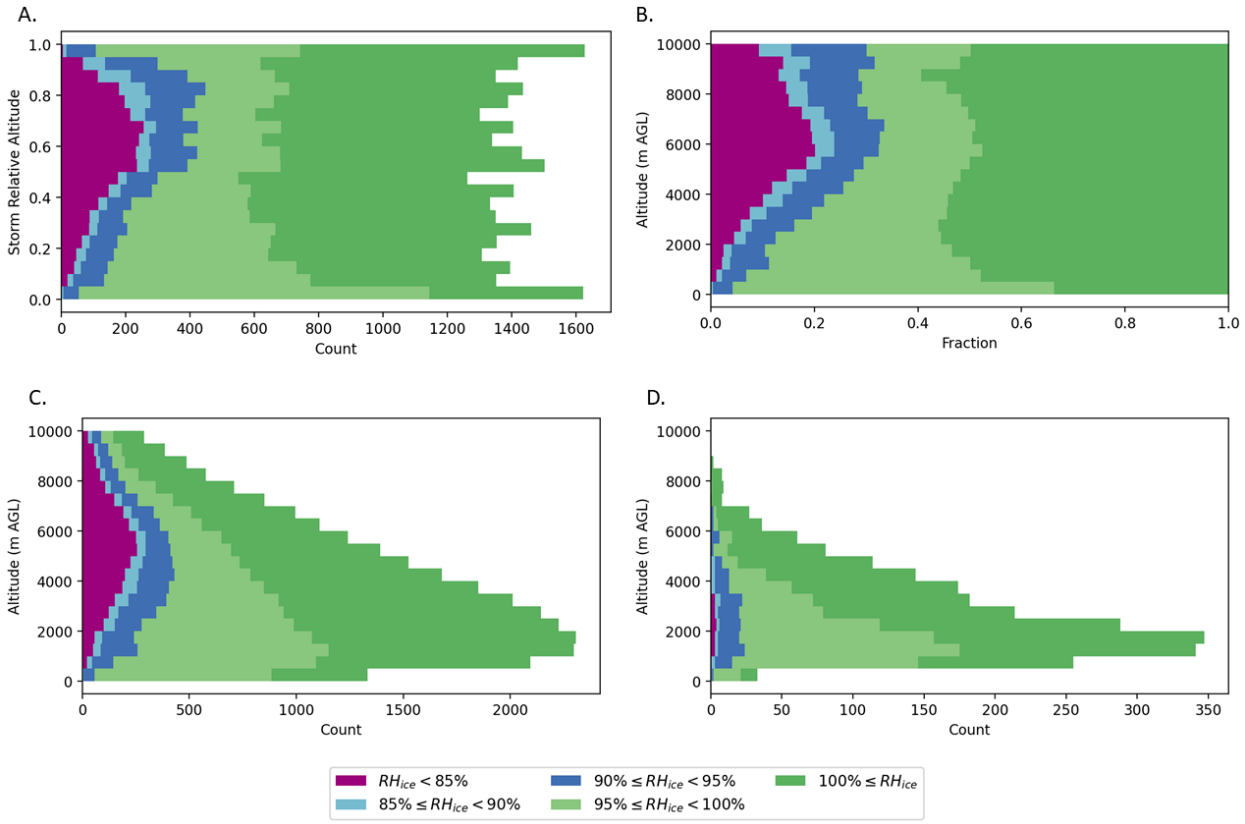

Figure A.9: Stacked histogram of RH_{ice} measurements within the storm vertical extent for soundings with surface temperatures < 0 °C and precipitation within 500 km of trackable low pressure centers. The storm vertical extent is based upon $RH_{ice} \geq 95\%$; this changes what sounding observations are included compared to Figure 4.2. Panel A. is binned by storm relative altitudes. Panel B. is binned by altitude AGL and normalized by the number of observations at each altitude. Panel C. is binned by altitude AGL. Panel D. is the subset of observations within the vertical extent that also have dBZ > 0, binned by altitude AGL. Paired with Figure 4.2

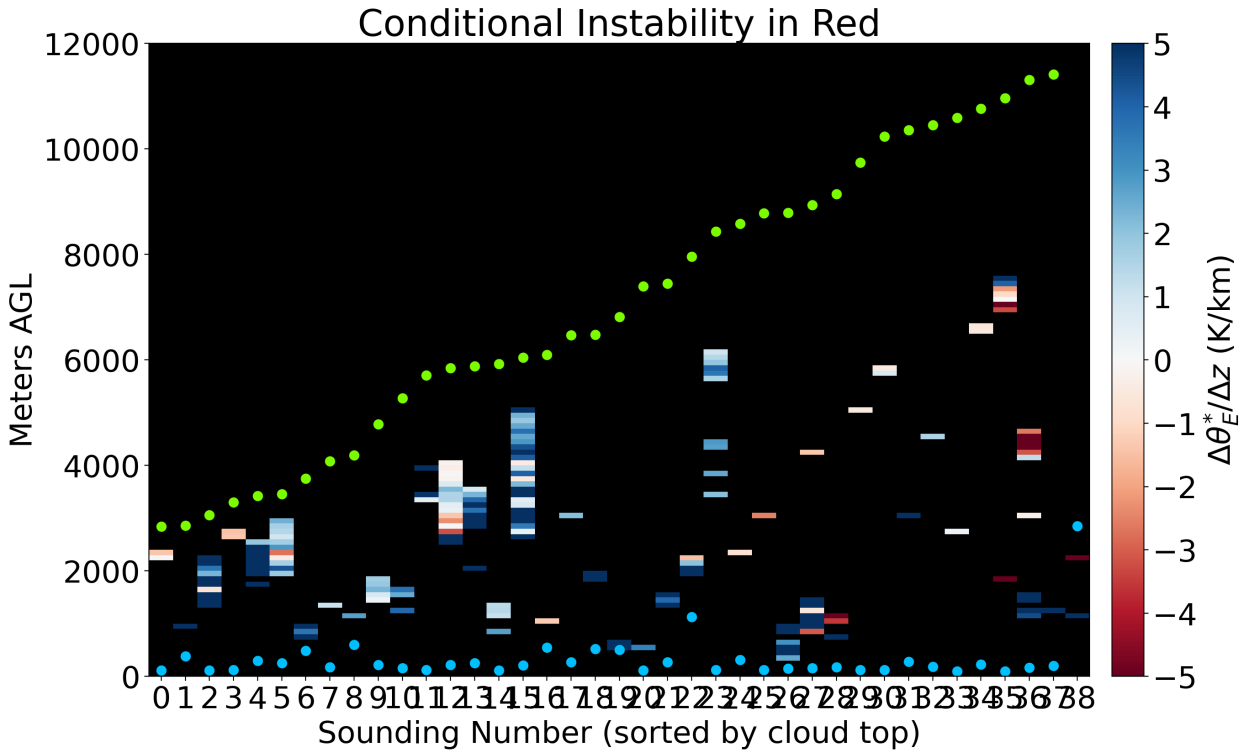

Figure A.10: Profiles of θ_E^* lapse rates for soundings with surface temperatures < 0 °C and surface precipitation within 500 km of trackable low pressure centers, limited to the subset of subliminating layers. Ice cloud is defined here as $RH_{ice} \geq 95\%$. Values less (greater) than 0 K/km are conditionally unstable (stable) and are shaded red (blue). Cloud base (top) is plotted as blue (green) dots. Paired with Figure 4.3

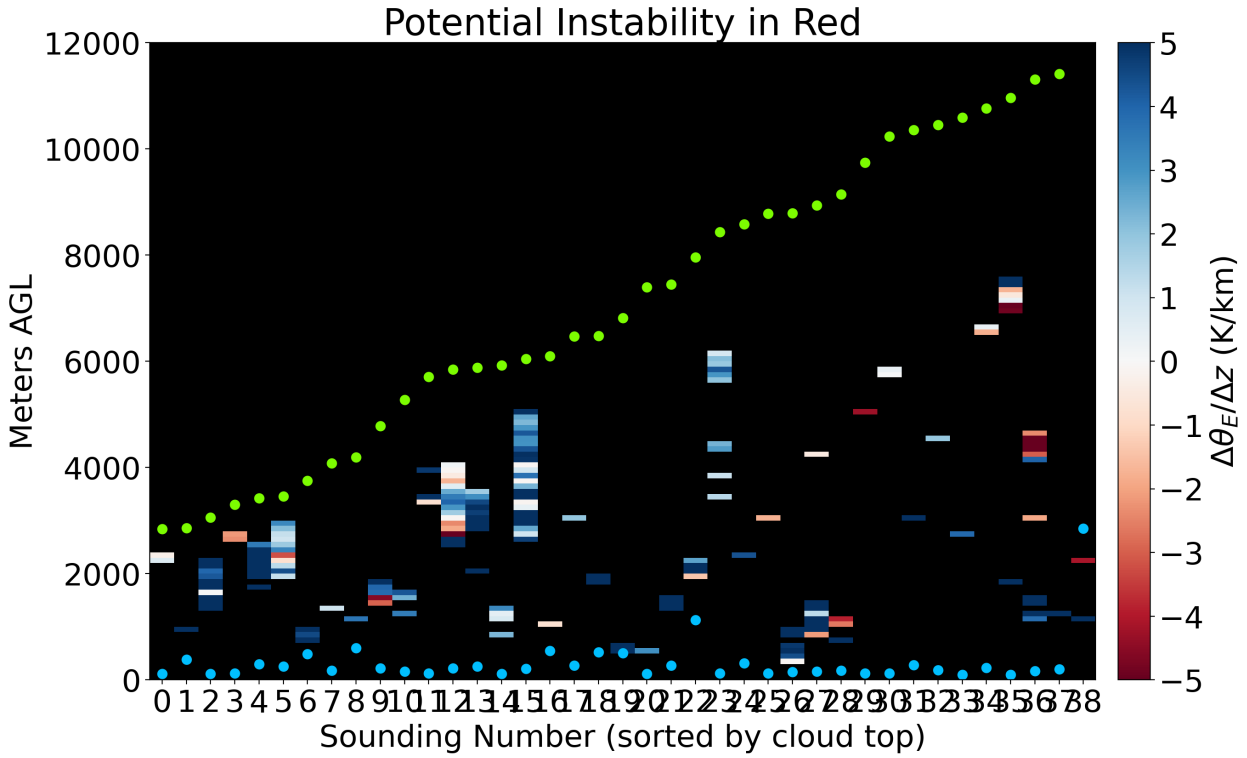

Figure A.11: Profiles of θ_E lapse rates for soundings with surface temperatures < 0 °C and surface precipitation within 500 km of trackable low pressure centers, limited to the subset of subliminating layers. Ice cloud is defined here as $RH_{ice} \geq 95\%$. Values less (greater) than 0 K/km are potentially unstable (stable) and are shaded red (blue). Cloud base (top) is plotted as blue (green) dots. Paired with Figure 4.4

APPENDIX

B

THERMODYNAMIC CALCULATIONS

This section details calculations of meteorological variables are derived from the sounding-measured variables in Table 2.1. When available, the MetPy Python package (May et al. 2022) is used to perform the calculations.

Saturation vapor pressure with respect to water is computed according to Equation 10 from Bolton (1980),

$$e_s(T) = 6.112 \exp\left(\frac{17.67T}{T+243.5}\right)$$

where e_s is in hectopascals and T is the air temperature in degrees Celsius. The dewpoint temperature is used in the same formula to compute the actual vapor pressure.

The saturation vapor pressure with respect to ice is computed according to Equation 23 from Alduchov and Eskridge (1996),

$$e_i(T) = 6.1121 \exp \frac{22.587T}{(273.86+T)}$$

Relative humidity with respect to water and ice are therefore

$$RH_w = \frac{e}{e_s}$$

$$RH_i = \frac{e}{e_i}$$

The psychrometric formula specified by American Meteorological Society (2023) is used to compute the wet-bulb temperature from the temperature, pressure, and actual and equilibrium vapor pressures.

$$e = e_s(T_w) - 6.60 \times 10^{-4}(1 + 0.00115T_w)p(T - T_w)$$

where T and T_w are the dry-bulb and wet-bulb temperatures in degrees Celsius, p, e, and $e_s(T_w)$ are the total air pressure, vapor pressure, and saturation vapor pressure at the wet-bulb temperature, respectively, in hPa. When the temperature is below freezing, the constant 6.60×10^{-4} is replaced with 5.82×10^{-4}.

The frost point is computed according to Romps (2021):

$$T_f = c[W_0(RH_s^{\frac{R_v}{(c_{vs}-c_{pv}}} c \exp c)]^{-1} T$$

$$c \equiv \frac{E_{0v} + E_{0s} - (c_{vv} - c_{vs})T_{trip}}{(c_{pv} - c_{vs})T}$$

where R_v=461 J kg^{-1} K^{-1} is the specific gas constant for water vapor; c_{vv}=1418 J kg^{-1} K^{-1} is the specific heat capacity at constant volume of water vapor; c_{vs}=1816 J kg^{-1} K^{-1} is the specific heat capacity at constant volume of solid water; $c_{pv} = c_{vv} + R_v$ is the specific heat capacity of water vapor at constant pressure; T_{trip}=273.16K is the triple-point temperature; E_{0v}=2.3740 MJ kg^{-1} is the difference in specific internal energy between water vapor and liquid water at the triple point; and E_{0s}=0.3337 MJ kg^{-1} is the difference in specific internal energy between liquid water and solid water at the triple point.

The equivalent potential temperature is computed using the method described by Bolton (1980).

$$\theta_E = \theta_{DL} \exp\left[\left(\frac{3036.}{T_L} - 1.78\right) * r(1 + .448r)\right]$$

where T_L is the temperature at the lifted condensation level

$$T_L = \frac{1}{\frac{1}{T_D - 56} + \frac{ln(T/T_D)}{800}} + 56$$

and θ_{DL} is the potential temperature of dry air at the lifted condensation level

$$\theta_{DL} = T\left(\frac{1000}{p - e}\right)^k \left(\frac{T}{T_L}\right)^{.28r}$$

The same calculation is used for the saturation equivalent potential temperature, but

assumes the process is saturated. This assumption means that T_L is equal to the current temperature and θ_{DL} simplifies to

$$\theta_{DL} = T\left(\frac{1000}{p-e}\right)^k$$

Vertical wind shear instability is assessed by the moist Richardson number (adapted from (Markowski and Richardson 2010)

$$mRi = \frac{N_m^2}{\left(\frac{\partial \bar{u}}{\partial z}\right)^2}$$

and N_m is the moist Brunt-Väisälä frequency Markowski and Richardson (2010).

$$N_m = \left(\frac{g}{\bar{\theta}_E}\frac{\Gamma_m}{\Gamma_d}\frac{\partial \bar{\theta}_E}{\partial z}\right)^{\frac{1}{2}}$$

The moist adibatic lapse rate, Γ_m, is an approximation of the pseudoadiabatic lapse rate, Γ_{ps}(American Meteorological Society 2022).

$$\Gamma_{ps} = g\frac{(1+r_v)(1+\frac{L_v r_v}{RT})}{c_{pd}+r_v c_{pv}+\frac{L_v^2 r_v(\epsilon+r_v)}{RT^2}}$$

where g is gravitational acceleration, r_v is the mixing ratio of water vapor, c_{pd} and c_{pv} are the specific heats at constant pressure of dry air and water vapor, L_v is the latent heat of vaporization, R is the dry air gas constant, $\epsilon \approx 0.62$ is the ratio of the gas constants of dry air and water vapor, and T is temperature.

Γ_d is the dry adiabatic lapse rate; $\Gamma_d = \frac{g}{c_{pd}}$

APPENDIX

C

ADDITIONAL FIGURES FOR SOUNDINGS WITHOUT SURFACE PRECIPITATION

For completeness, relevant figures for the subset of soundings without surface precipitation are presented in this section. The findings from these figures do not change any of the main results.

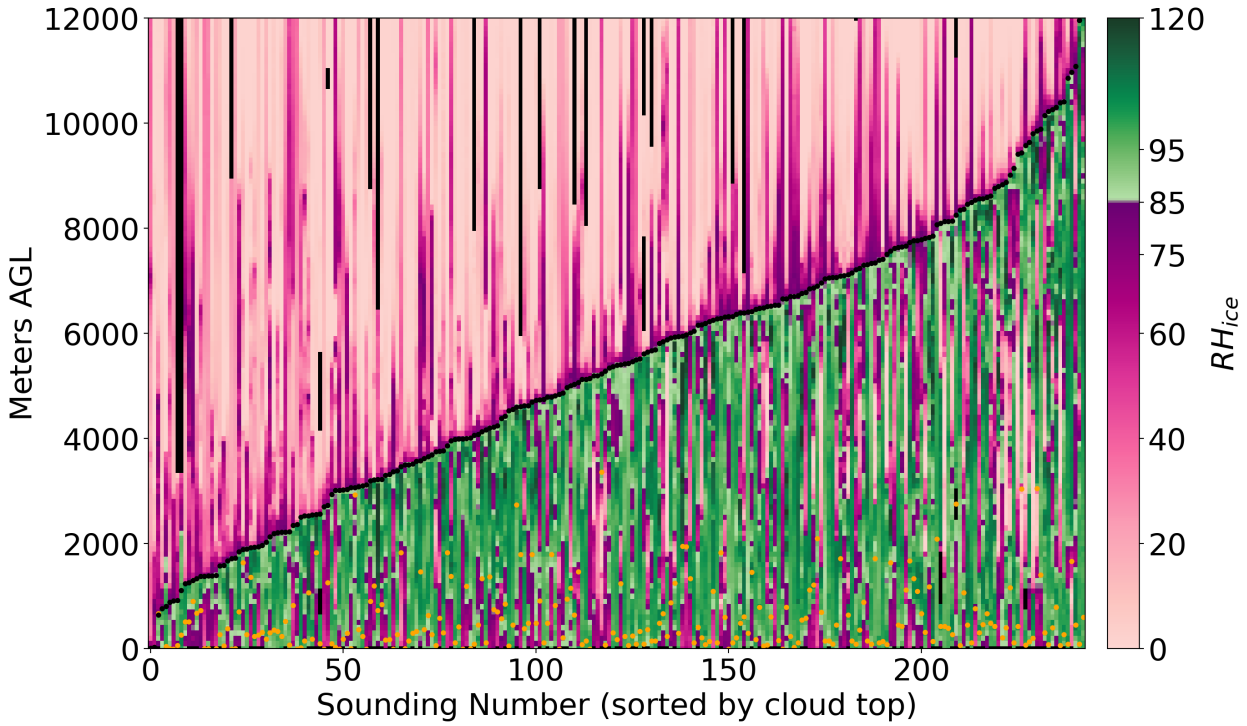

Figure C.1: Profiles of RH_{ice} from soundings with surface temperatures < 0 °C and *without* surface precipitation within 500 km of trackable low pressure centers. Profiles are color coded by RH_{ice} value in each 100 m layer. Each column represents one sounding. Soundings are sorted based on first the estimated cloud top (black, median value is 6.5 km) and second on the ASOS ceilometer cloud base (orange). Paired with similar figure for subset of soundings with surface precipitation in Fig. 3.4.

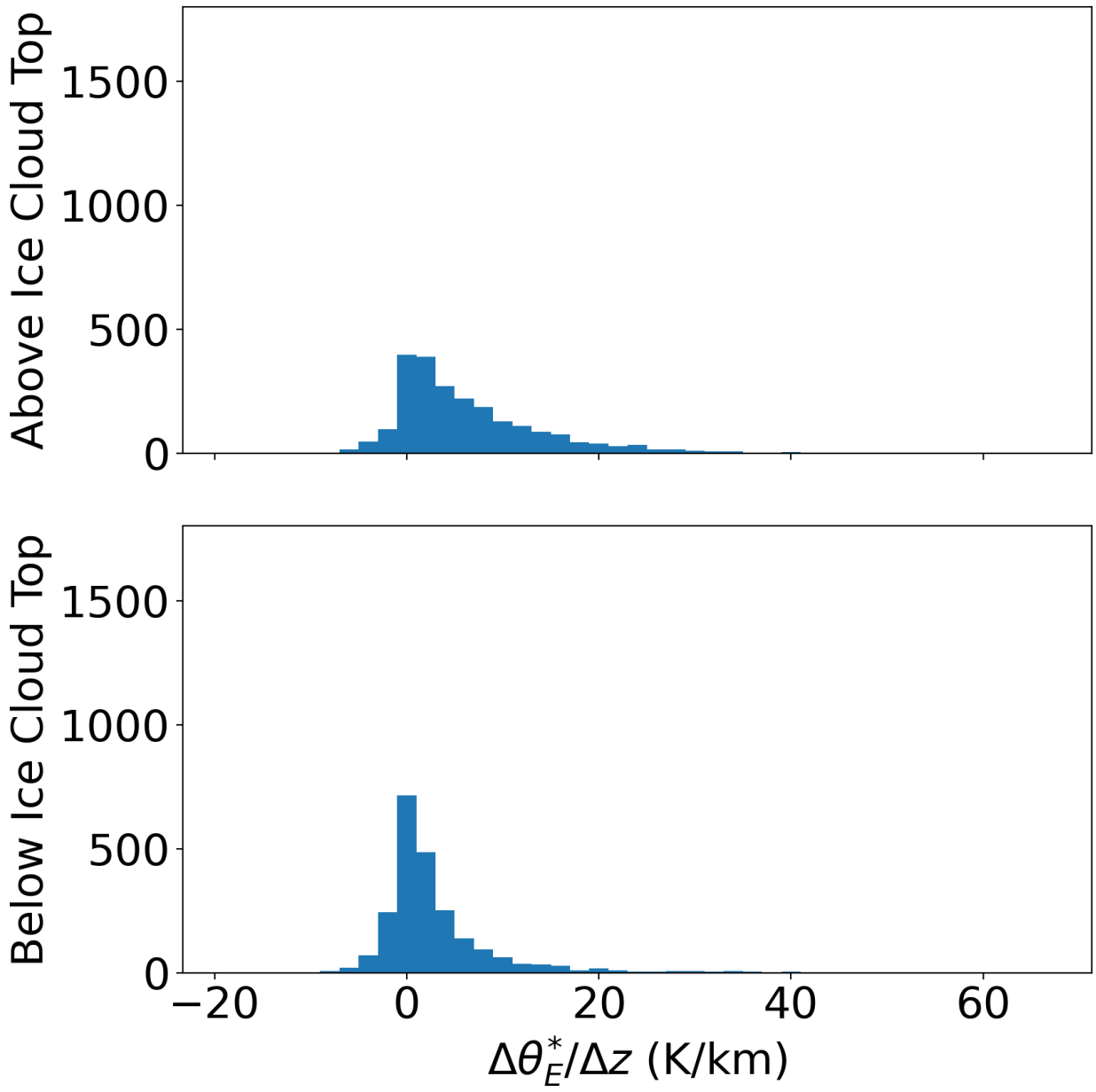

Figure C.2: Histograms of θ_E^* lapse rates 1 km above and 1 km below cloud top from soundings with surface temperatures < 0 °C and *without* precipitation within 500 km of trackable low pressure centers. Values <0 K/km are conditionally unstable. The longer tail of stable lapse rates above the cloud top indicates increased stability above the storm vertical extent. Paired with similar figure for subset of soundings with surface precipitation in Fig. 3.10.

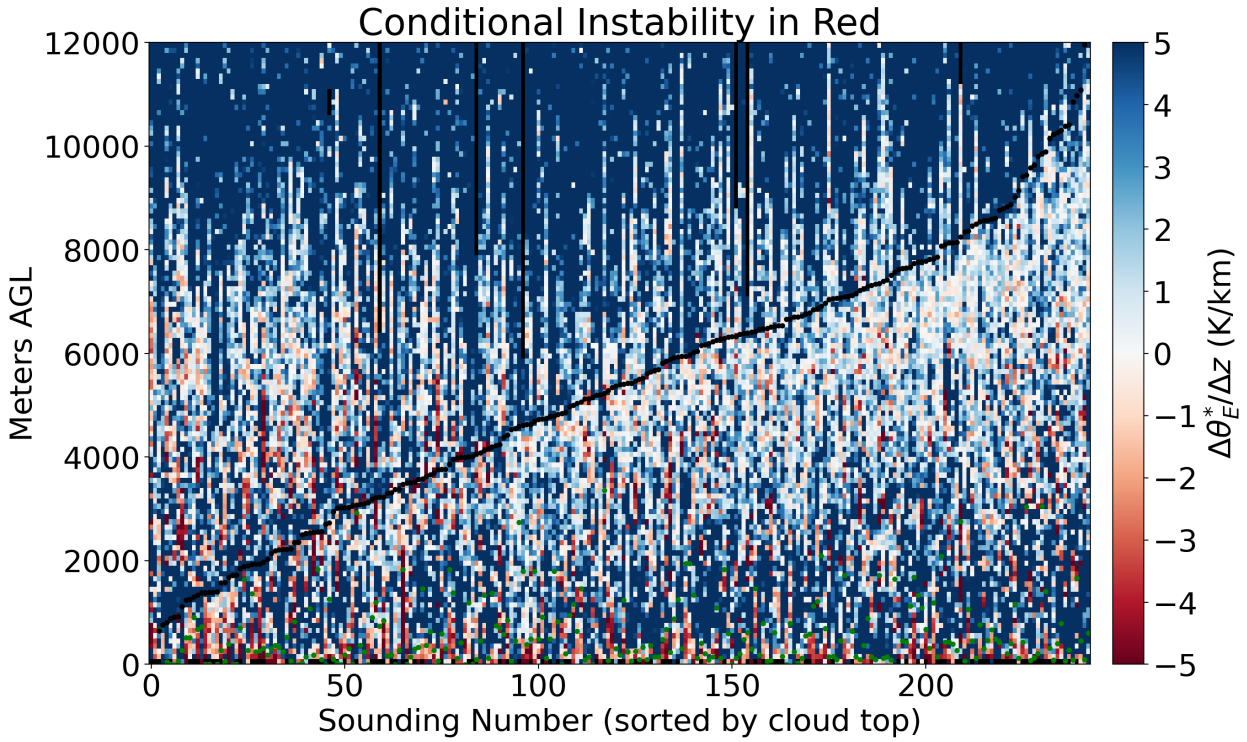

Figure C.3: Profiles of θ_E^* lapse rates for soundings with surface temperatures < 0 °C and *without* surface precipitation within 500 km of trackable low pressure centers. Values less (greater) than 0 K/km are conditionally unstable (stable) and are shaded red (blue). Cloud base indicated by green dots and cloud top by black dots. Paired with similar figure for subset of soundings with surface precipitation in Fig. 3.11.

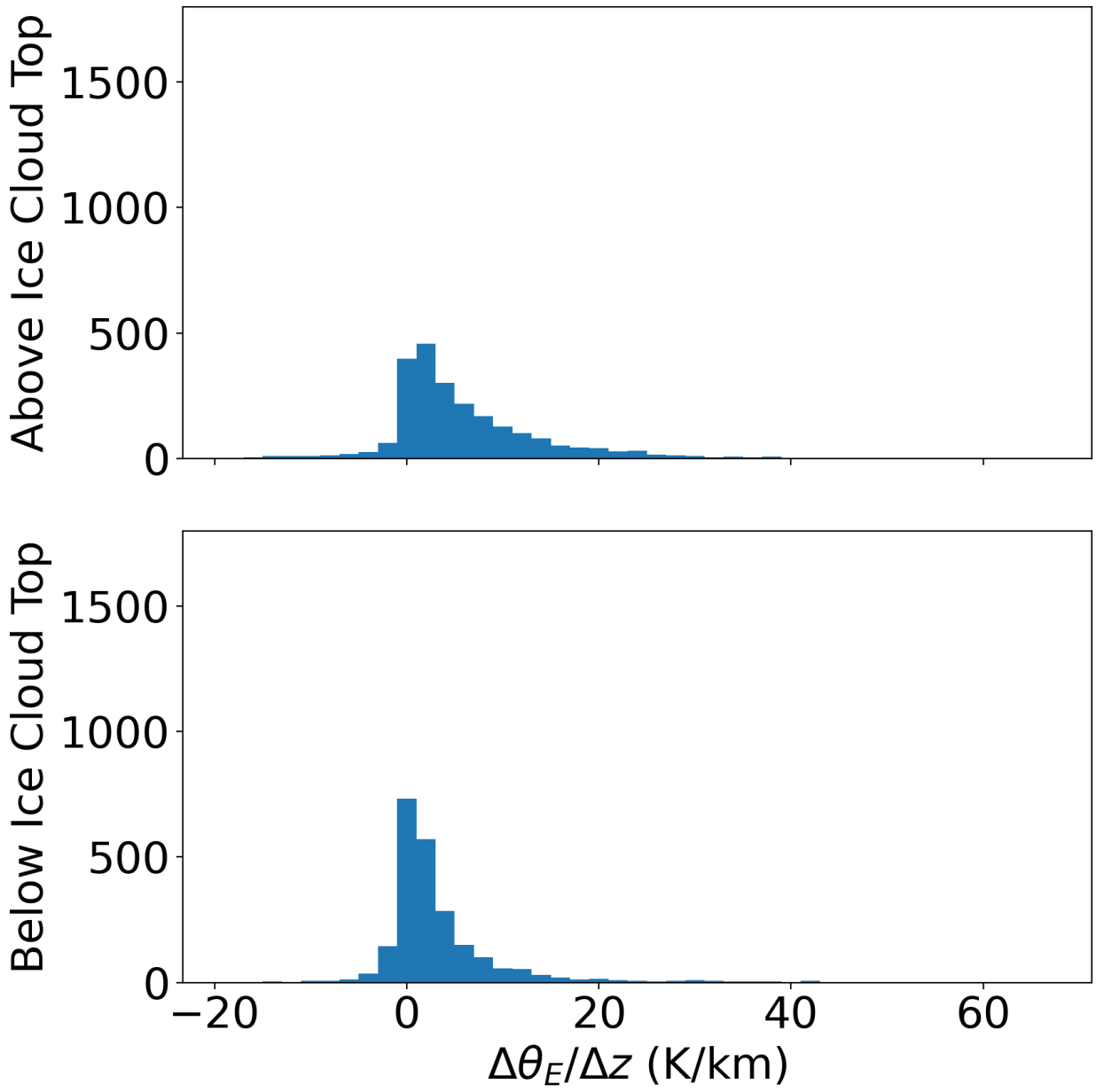

Figure C.4: Histograms of θ_E lapse rates 1 km above and 1 km below cloud top from soundings with surface temperatures < 0 °C and *without* precipitation within 500 km of trackable low pressure centers. Values <0 K/km are potentially unstable. The longer tail of stable lapse rates above the cloud top indicates increased stability above the storm vertical extent. Paired with similar figure for subset of soundings with surface precipitation in Fig. 3.12.

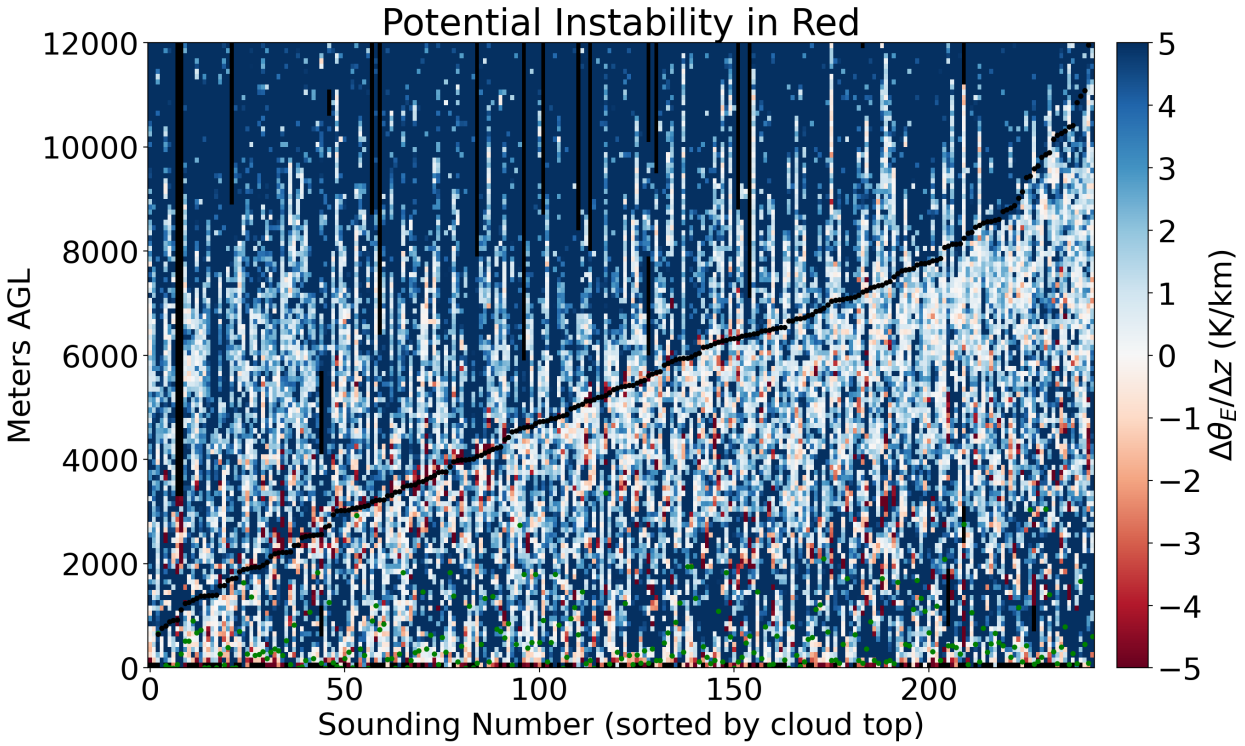

Figure C.5: Profiles of θ_E lapse rates for soundings with surface temperatures < 0 ° C and *without* surface precipitation within 500 km of trackable low pressure centers. Values less (greater) than 0 K/km are potentially unstable (stable) and are shaded red (blue). Cloud base indicated by green dots and cloud top by black dots. Paired with similar figure for subset of soundings with surface precipitation in Fig. 3.13.

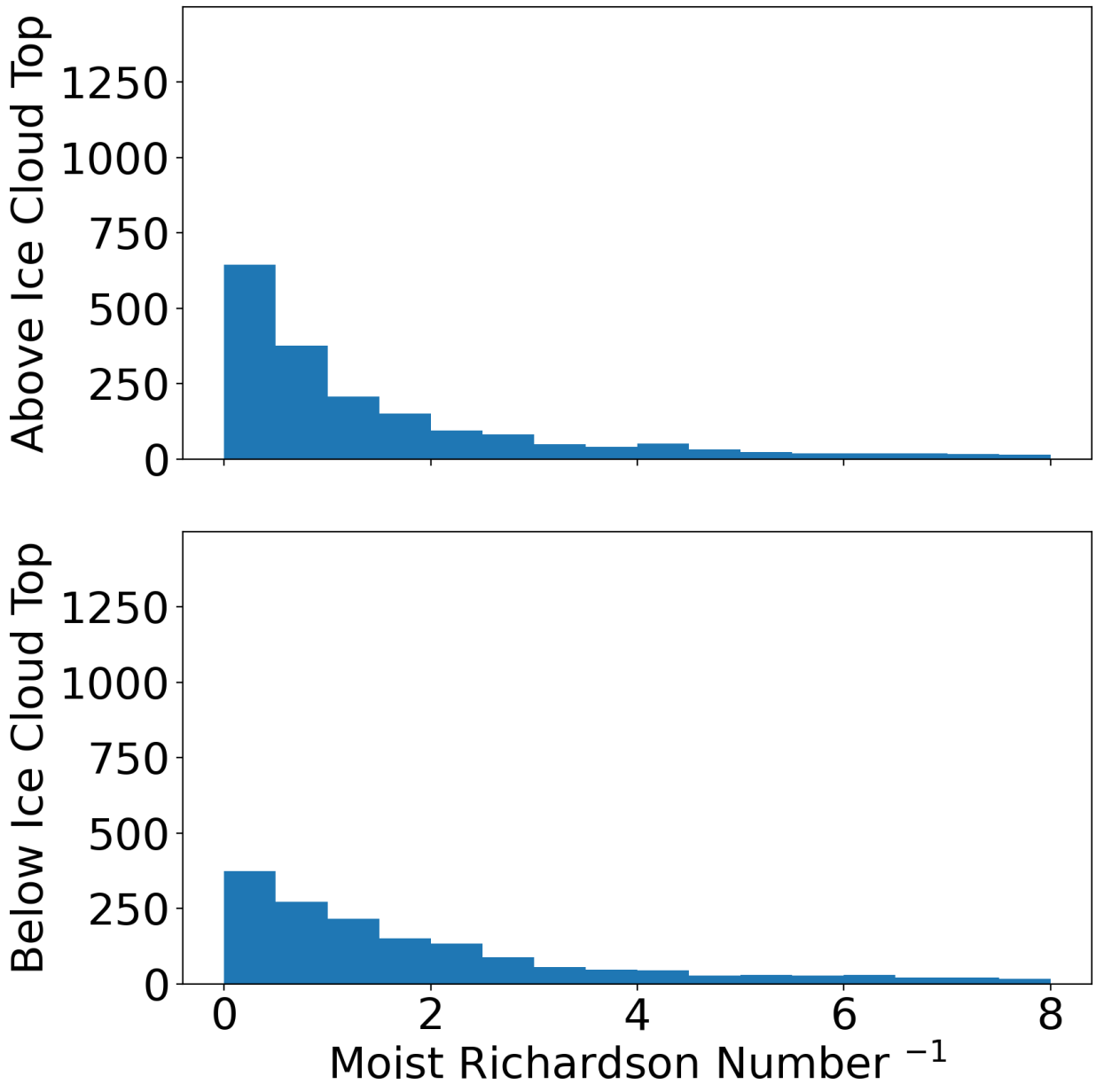

Figure C.6: Histograms of mRi^{-1} 1 km above and 1 km below cloud top from soundings with surface temperatures < 0 °C and *without* precipitation within 500 km of trackable low pressure centers. Values greater than 4 have vertical shear instability. Paired with similar figure for subset of soundings with surface precipitation in Fig. 3.15.

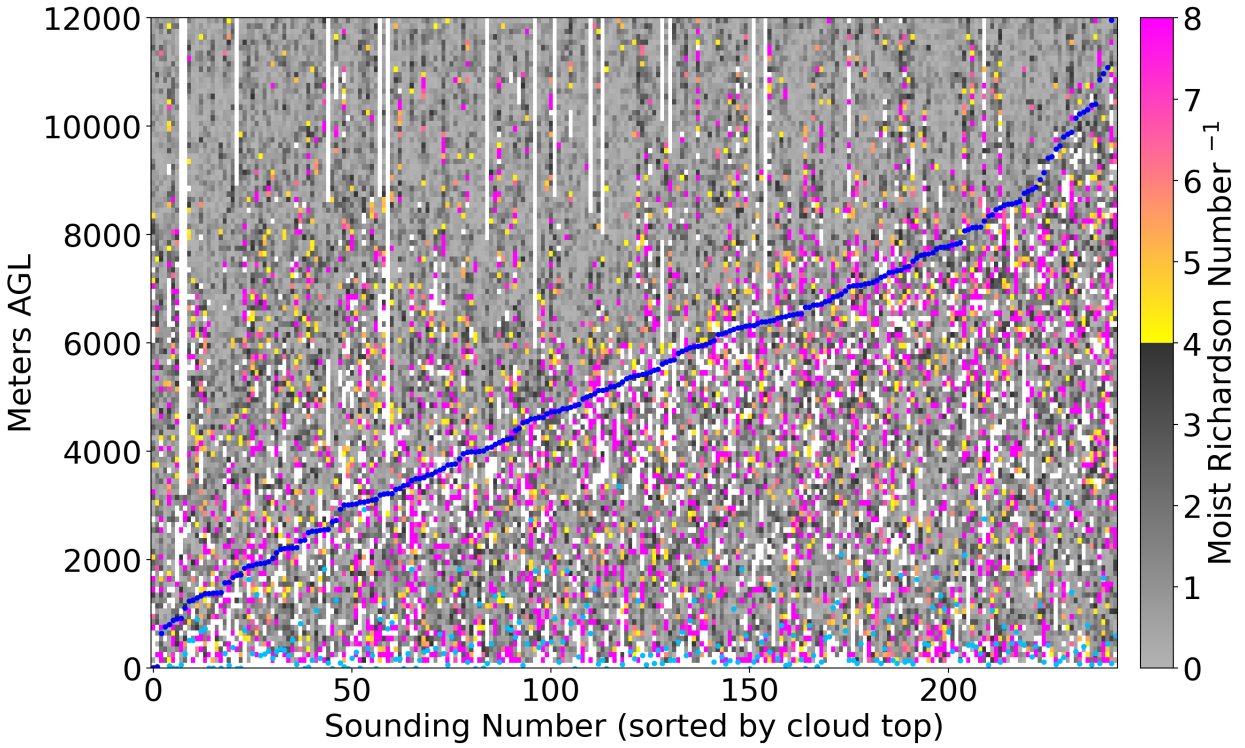

Figure C.7: Profiles of mRi^{-1} for soundings with surface temperatures < 0 °C and *without* surface precipitation within 500 km of trackable low pressure centers. Values greater than 4 have vertical shear instability and are color coded. Stable values are shown in gray. Cloud base indicated by light blue dots and cloud top by dark blue dots. Paired with similar figure for subset of soundings with surface precipitation in Fig. 3.17.

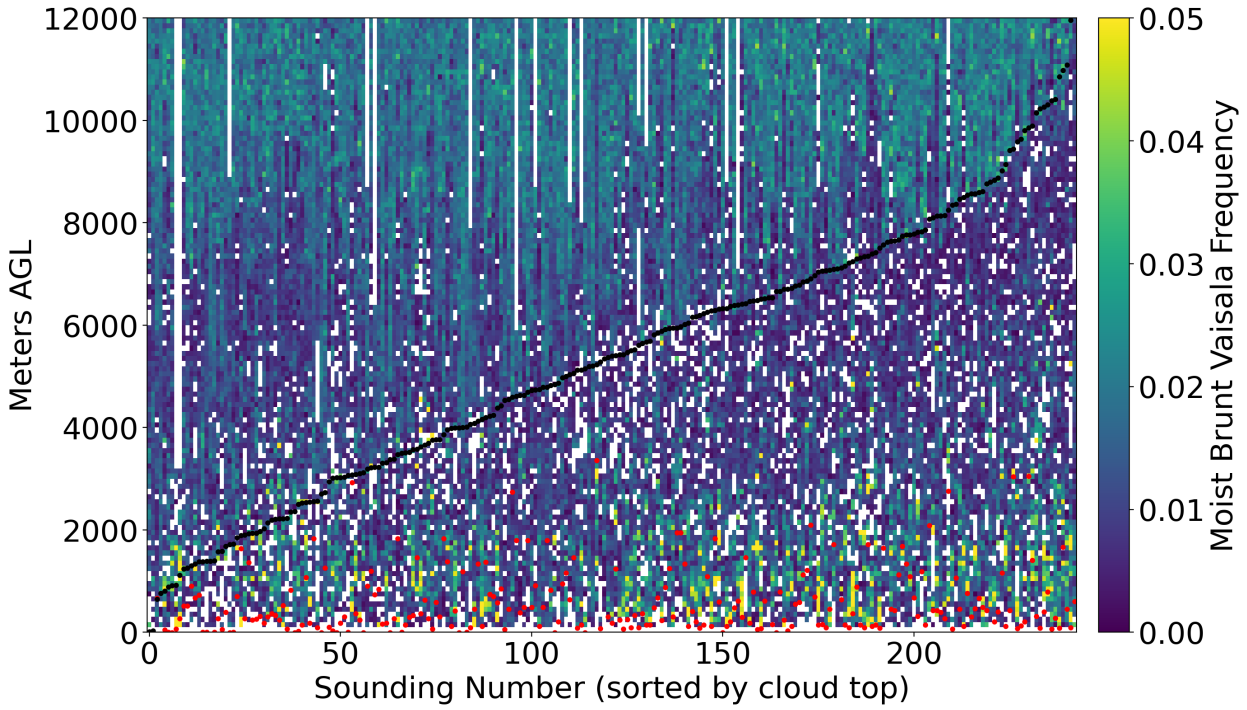

Figure C.8: Profiles of the moist Brunt-Väisälä frequency for soundings with surface temperatures < 0 °C and *without* surface precipitation within 500 km of trackable low pressure centers. Larger values are more stable. Cloud base indicated by red dots and cloud top indicated by black dots. Paired with similar figure for subset of soundings with surface precipitation in Fig. 3.19.

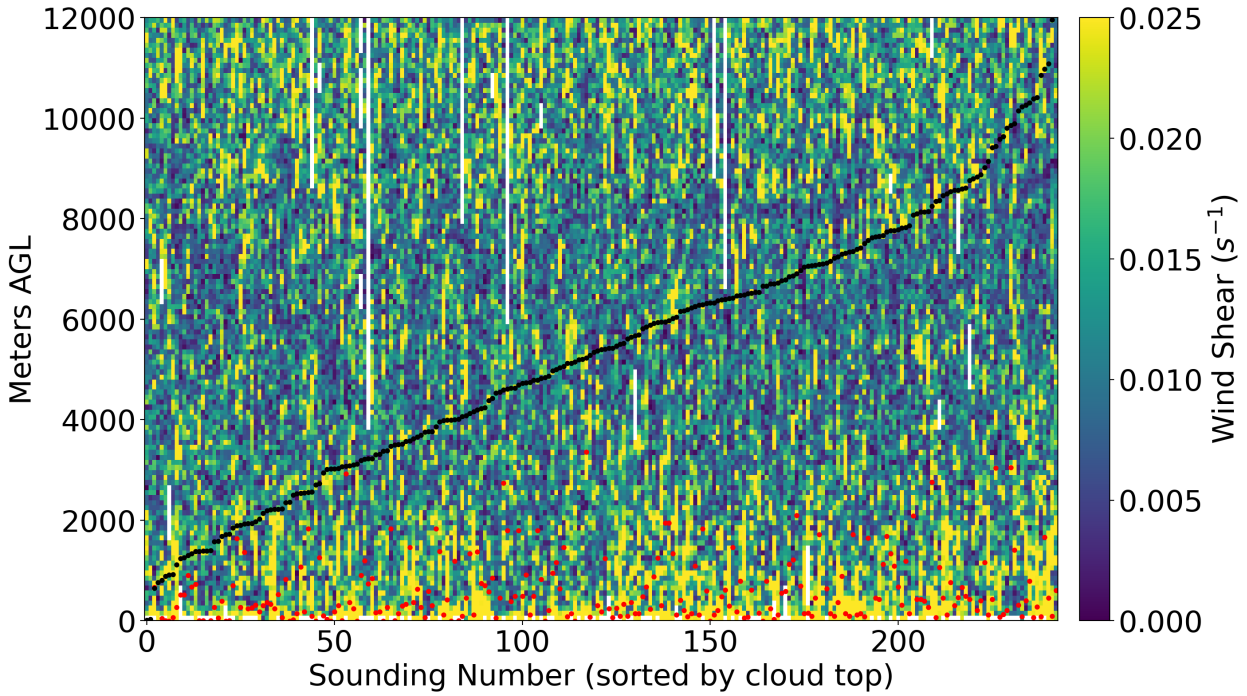

Figure C.9: Profiles of $\frac{\partial \bar{u}}{\partial z}$ for soundings with surface temperatures < 0 °C and *without* surface precipitation within 500 km of trackable low pressure centers. Cloud base indicated by red dots and cloud top by black dots. Paired with similar figure for subset of soundings with surface precipitation in Fig. 3.20.